Lehrstuhl für THERMODYNAMIK

MASTER'S THESIS

Thermoacoustic Characterization of a Single Burner Gas Turbine Combustor

Author:
Muhammad Yasir

Matriculation No.:
03684319

Supervisors:
Prof. Dr.-Ing. Thomas Sattelmayer
Jan Kaufmann, M.Sc.

January 26, 2020

DOI:
10.14459/2022md1656179

Chair of Thermodynamics
Prof. Dr.-Ing. Thomas Sattelmayer
www.td.mw.tum.de

Declaration

I hereby declare that this thesis is my own work prepared without the help of a third party. No literature and resources other than those listed have been used.

Erklärung

Hiermit versichere ich, die vorliegende Arbeit selbstständig verfasst zu haben. Ich habe keine anderen Quellen und Hilfsmittel als die angegebenen verwendet.

Ort, Datum	Muhammad Yasir

Abstract

Modern gas turbines employ lean premixed combustion to reduce NO_x emissions. However, flames in such combustion are prone to thermoacoustic instabilities resulting from a two-way coupling between the combustor acoustic modes and unsteady heat release. The dynamic response of flames to acoustic perturbations is quantified in terms of velocity-coupled Flame Transfer Functions (FTFs). This study was performed to measure the FTFs of a perfectly premixed natural gas flame in a gas turbine combustor subject to 1D longitudinal thermoacoustics. Measurements were done for thermal power in the range of 40-55 kW and air ratio in the range of 1.4-1.7, covering 80-640 Hz frequency spectrum. The otherwise stable swirl flame was forced to acoustic excitation through the upstream and downstream sirens. The acoustic behaviour of the burner and flame were characterised in terms of the transfer matrices determined from acoustic pressure measurements at multiple axial locations using microphones. FTFs were then evaluated using the transfer matrix of the flame. Alternatively, the heat release fluctuation was directly measured using a photomultiplier installed with an OH* chemiluminescence filter. By matching the results from the two methods, estimates for the combustor and flame temperatures were obtained. These estimates showed a similar trend as predicted by an analytical model from previous research. Procedures adopted showed good reproducibility of FTF results. Moreover, the results were found to be not influenced by the measurement locations for acoustic pressure. The variation in FTFs with thermal power and air ratio were explained using flame geometry variation evaluated by means of OH* chemiluminescence imaging. The FTF amplitude generally increased with the thermal power and air ratio, except for a decrease at high frequency with increasing air ratio. The phase plots suggested a constant convective time delay between the velocity perturbations and flame heat release fluctuation, which increased with increasing air ratio. A Proper Orthogonal Decomposition (POD) based reduced-order model of FTFs was also developed. The model offered a decomposition of the FTF sensitivity to operating parameters. Some of the resulting POD modes correlated well with the physical sensitivity mechanisms, aiding in the understanding of FTF variation with operating conditions. Moreover, the model results were used to estimate the FTF at a non-measured desired operating point simply through the interpolation of POD coefficients. The modelling results were validated against the experimental measurements and good agreement was achieved.

Contents

List of Figures

List of Tables

Nomenclature

Roman Letters

A	$[m^2]$	Area
a	[−]	POD coefficient
c	[m/s]	Speed of sound
d	[m]	Diameter
f	[Hz]	Acoustic temporal frequency
f	[m/s]	Riemann invariant travelling downstream
g	[m/s]	Riemann invariant travelling upstream
H	[J/kg]	Specific reaction enthalpy
h	$[m^2 \cdot kg/s]$	Planck's constant
I	[−]	OH* chemiluminescence intensity
i	[−]	Imaginary number $\sqrt{-1}$
k	[1/m]	Wave number
L	[m]	Length
m	[No.]	No. of measurements
n	[No.]	No. of data points
P	[W]	Power
p	[Pa]	Pressure
R	[J/kg·K]	Gas constant
r	[m]	Radial coordinate
s	[m/s]	Flame burning velocity
S_N	[−]	Swirl number
T	[K]	Temperature
t	[s]	Time
t_0	[s]	Time period of oscillation cycle
u	[m/s]	Velocity
V	$[m^3]$	Volume
w	[w]	POD distribution space

X	[m]	Lift-off distance
x	[m]	Axial coordinate
Z	[−]	Acoustic impedance
$\dot{Q}$	[W]	Heat release rate

Greek Letters

β	[−]	Specific impedance ratio
ϵ	[−]	Eigenvalue for POD
γ	[−]	Specific heat ratio
λ	[−]	Excess air ratio
ν	[Hz]	Electromagnetic frequency
Ω	[1/s]	Vorticity
ω	[rad/s]	Angular frequency
Φ	[m]	Diameter
ϕ	[rad]	Phase angle
ψ	[−]	POD dynamic space
ρ	$[\mathrm{kg/m^3}]$	Density
τ	[s]	Time delay
θ	[−]	POD mode for FTF amplitude
θ	[rad]	POD mode for FTF phase

Matrices

$\mathbf{\Omega}$	Linear transformation matrix
$\mathbf{\Theta}$	POD modes matrix
$\mathbf{A}$	POD coefficients matrix
$\mathbf{C}$	Covariance matrix
$\mathbf{H}$	Matrix of f, g oscillating terms
$\mathbf{p}$	Matrix of acoustic pressures
$\mathbf{V}$	Matrix of data ensemble

Dimensionless Numbers

He	Helmholtz number
Ma	Mach number

Subscripts

θ	Azimuthal coordinate
A	Quantity per unit area, Upstream siren location
a	Burner upstream
ac	Acoustic
ad	Adiabatic
B	Downstream siren location
b	Burner exit
C	Cold
c	Flame upstream
$comb$	Combustor
cr	Critical
d	Downstream location
ds	Downstream duct
en	Ensemble
Exp	Experimental
F	Flame
f	Fuel
H	Hot
h	Flame downstream
j	Arbitrary POD mode
max	Maximum
min	Minimum
r	Ratio
ref	Reference
st	Stoichiometric
th	Thermal
u	Upstream location
us	Upnstream duct
V	Quantity per unit volume

Superscripts

$+$	In the flow direciton
$-$	Against the flow direction
A	Upstream excitation
B	Downstream excitation

fg	fg notation of transfer matrix
pu	pu notation of transfer matrix

Operators

$\dot{(..)}$	Temporal rate
$(..)'$	Perturbation
$\bar{(..)}$	Mean
$\hat{(..)}$	Amplitude of oscillating variable
$(..)^\intercal$	Matrix transpose
$(..)^\dagger$	Matrix pseudo inverse
$\|..\|$	Magnitude of complex quantity
$\angle(..)$	Phase angle
$\mathcal{O}(..)$	Equal and higher orders of
$Re(..)$	Real part of complex number

Abbreviations and Acronyms

Amp.	Amplitude
Coeff.	Coefficients
Temp.	Temperature
AAD	Average Absolute Deviation
AEV	Advanced En-Vironmental
BC	Boundary Condition
CCD	Charge Coupled Device
CL	Chemiluminescence
CW	Cooling Water
BFTM	Burner+Flame Transfer Matrix
BTM	Burner Transfer Matrix
DAQ	Data Acquisitioner
FFT	Fast Fourier Transform
FPS	Frames-Per-Second
FTF	Flame Transfer Function
FTM	Flame Transfer Matrix
FWHM	Full Width Half Maximum
ICLEAC	Instability Control of Low Emission Aero-engine Combustor
IRZ	Outer Recirculation Zone

LOS	Line-Of-Sight
MAD	Median Absolute Deviation
MMM	Multi-Microphone Method
MRI	Mode Relevance Index
MSI	Mode Sensitivty Index
NI	National Instruments Inc.
OH	OH* chemiluminescence
OP	Operating Point
ORZ	Outer Recirculation Zone
PIV	Particle Image Velocimetry
POD	Proper Orthogonal Decomposition
RH	Rankine-Hugoniot
RMSE	Root Mean Square Error
ROM	Reduced Order Model
SSE	Sum of Squares Error
TM	Transfer Matrix
UHC	Unburned Hydrocarbons
UV	Ultraviolet
VB	Vortex Breakdown
VI	Virtual Instrumentation

1 Introduction

1.1 Gas Turbines and Emissions Reduction

Despite of a growing trend in energy and transport markets of shifting from fossil-fuels to renewable sources, the former will continue playing an important role in the near future. This can be observed in Figure 1.1 which shows the history and projection of installed power generation capacity for different energy sources. It is anticipated that 74% of electricity would come from conventional systems even in 2040 [1]. Although the contribution of coal and oil is declining, an increase for gas is evident.

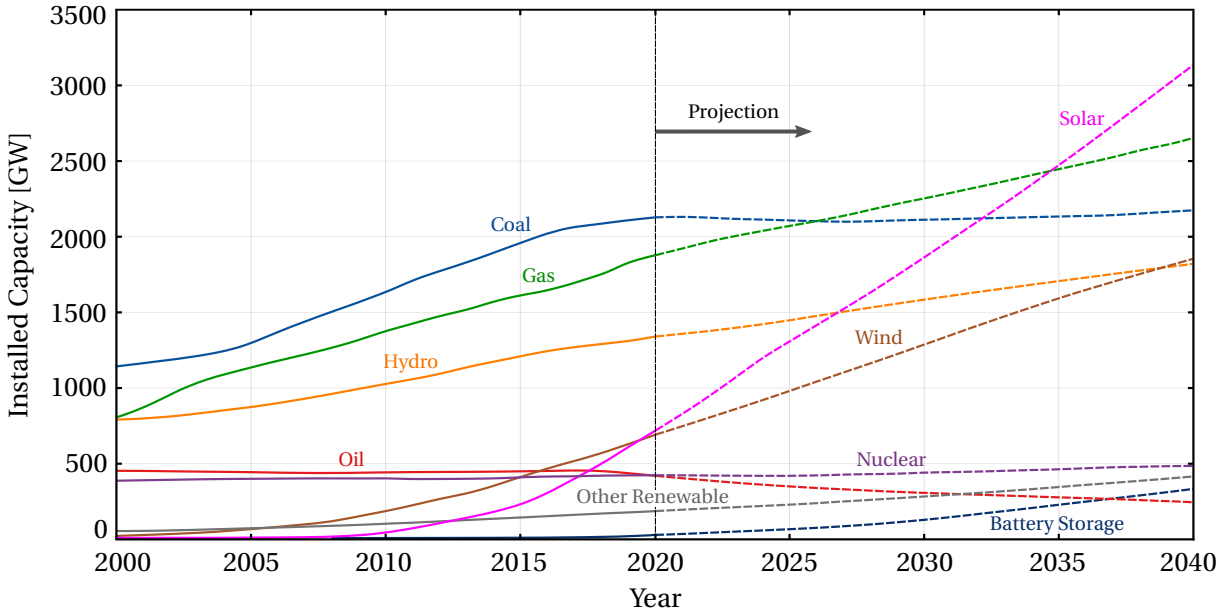

Figure 1.1: *Installed power generation capacity by source in Stated Policies Scenario [2]*

Compared with other conventional systems, gas turbines aid in integrating intermittent supply from renewables [3]. This is because of their flexible operation and reliability [1]. Hence, gas turbines would remain relevant in the power sector.

However, the environmental cognizance demands reformation of conventional gas turbines to reduce pollutant emissions. Design and efficiency improvements have produced a signific-

ant reduction in some of these pollutants, like soot. Other emissions which remain of concern are Carbon Monoxide (CO), Unburned Hydrocarbons (UHCs), and oxides of Nitrogen (NO_x) [4]. The trends for these emissions and the flame temperature T_F with respect to Air/Fuel ratio are shown in Figure 1.2(a). CO and UHCs are controlled by operating just leaner than stoichiometric mixture [4]. That is providing slightly more air than the theoretically required amount for complete combustion. However at this condition, thermal NO_x which has an exponential dependence upon flame temperature, is very high. It leads to smog, acid rain, and unwanted ozone [5, 6].

(a) Emissions and flame temperature

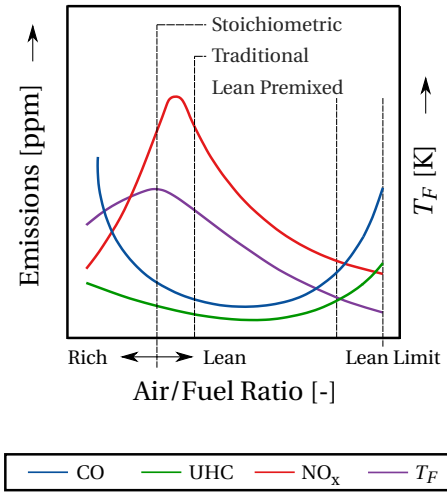

(b) Reduction in NO_x over the years

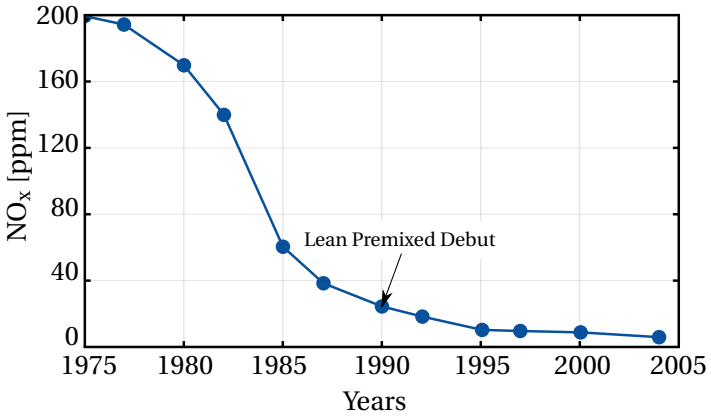

Figure 1.2: *Typical emissions, flame temperature in gas turbines (adopted from [6, 7]), and NO_x reduction over the years [6]*

Using different methods, a significant reduction in NO_x levels has been achieved over the years as shown in Figure 1.2(b). Among others, *Lean Premixed* combustion has become a standard technology in modern gas turbines since 1990s [7, 8]. The lean mixture ensures reduction in global peak temperature while premixing of fuel and air well in advance of burning provide a uniform temperature distribution avoiding local hotspots. This combustion mode leads to a significant reduction in NO_x but increases energy density of the flame. Moreover, the combustion occurs near lean (blowout) limit. Subsequently, the system becomes more susceptible to adverse *thermoacoustic instabilities* [9–11], which are discussed in the next section.

1.2 Thermoacoustic Instabilities

In a combustion system, thermoacoustic instabilities refer to large-amplitude oscillations in operational variables such as the combustor pressure. They result due to a two-way coupling between the unsteady heat release at the flame and acoustic waves formed inside the

combustor [12]. There are two main reasons for these instabilities as discussed in subsequent paragraphs.

The first reason is that combustors are closed cavities [13] and therefore have specific *natural* acoustic modes. These modes can be excited by providing sufficient energy and resonant acoustic waves can form in the combustor at corresponding *natural frequencies*. Depending upon the direction of oscillations with respect to combustor geometry, different modes are possible [12, 14] as shown in Figure 1.3. The colour field shows distribution of acoustic pressure p' on the combustor walls at a given time instant. *Longitudinal* modes occur when the direction of oscillation is aligned with axial direction of the combustor which is usually the flow direction. They are often 1D and occur at frequencies in the range of 50-1000 Hz. *Azimuthal* modes have similar frequencies but gas particles oscillate circumferentially. Transverse modes refer to oscillations along an axis perpendicular to the axial direction, such as the *Transverse-Azimuthal* mode shown in Figure 1.3. A special case of transverse oscillation is the *Transverse-Radial* mode when the gas particles follow the radial direction. The transverse modes occur above 1000 Hz when wavelength is comparable or less than transverse dimensions of the combustor. Mixed modes may also result from any combination of these modes [13].

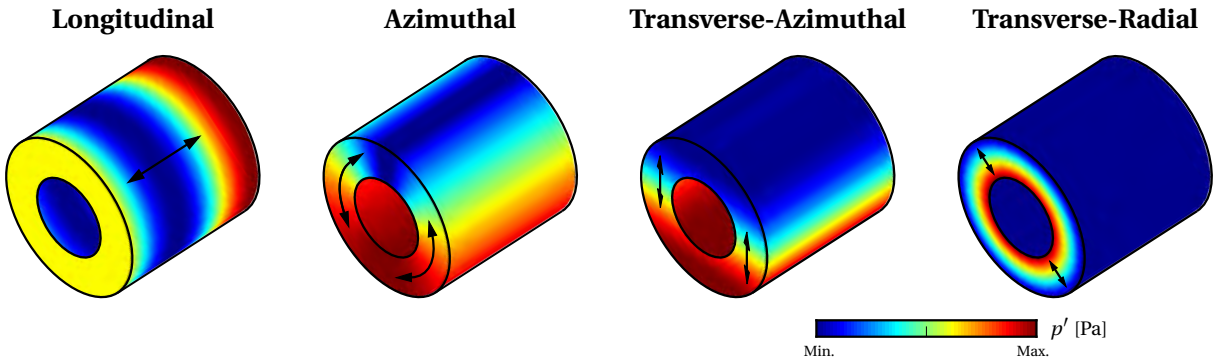

Figure 1.3: *Types of acoustic modes in a combustor*

The second main possible reason for thermoacoustic instabilities is that the heat released at flame has far more energy than that required to actuate any of these acoustic modes [13]. A small fluctuation in heat release, for instance due to turbulent noise, may produce sufficient perturbation in combustor pressure for formation of acoustic waves. These waves can pulsate the flow conditions in the air and fuel supply to the combustor, leading to heat release oscillations. An exemplary evolution of a Kerosene flame during a thermoacoustic cycle is shown in Figure 1.4 to demonstrate the sensitivity of flame to acoustic perturbations. It shows temporal sequence of OH* chemiluminescence images used for flame visualisation at different instances during the cycle period t_0.

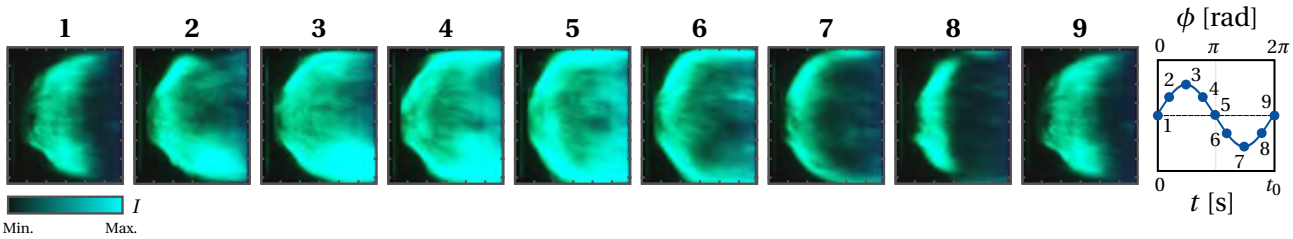

Figure 1.4: *Exemplary evolution of a Kerosene flame during a thermoacoustic instability cycle (adopted from [15])*

It is clear that the flame responds significantly to acoustic perturbation, hence leading to high oscillations in heat release. This unsteady heat release may reinforce the acoustic mode forming a feedback loop as shown in Figure 1.5.

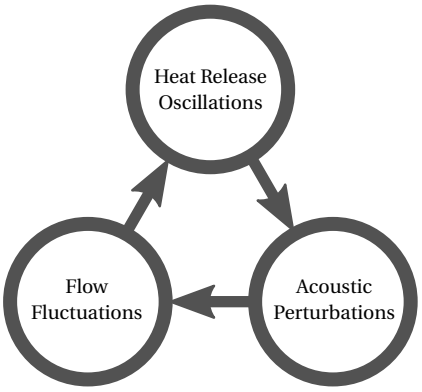

Figure 1.5: *Basic feedback loop responsible for thermoacoustic instabilities [12]*

Under right conditions, oscillating heat release and combustor pressure may amplify one another up to saturation, producing high final amplitudes. This may cause noise, operational issues, and even structural damage [16]. However, current state of the art is that thermoacoustic stability behaviour cannot be reliably predicted during early design phase [17]. Therefore, research and systematic testing is required to better understand these instabilities and develop active control methods for their mitigation [14].

Longitudinal thermoacoustics for natural gas swirl combustion has been widely studied. Several authors have experimentally measured the flame response to acoustic perturbations using different techniques. One approach is to measure the acoustic perturbation in the flow and fluctuation in the flame heat release. For instance, Freitag used OH* chemiluminescence for quantifying the flame heat release and hot-wire anemometry for flow fluctuation [18]. This arrangement has also been used by other researchers, such as [19, 20]. The other common approach is to use microphones for measuring pressure perturbation. The acoustic behaviour of burner and flame is then quantified only using these measurements as was done by Stadlmair [21]. Alemela *et al.* used a hybrid method in which heat release was quantified using OH* chemiluminescence and flow perturbation was indirectly determined using microphone measurements [22]. A network modelling method is usually employed for a simpler

acoustic analysis of instability problems. Schuermans used this procedure for studying thermoacoustics of a premixed flame and successfully validated the results against experimental measurements [23]. Bade used a combination of different approaches to study the influence of burner geometry and operating conditions on flame dynamics [24–26]. OH* chemiluminescence flame images representative of the heat release distribution were also used for this purpose.

On the other hand, little research is reported for thermoacoustics in Kerosene flames. Eckstein *et al.* reported fluctuations in atomisation to be responsible for low frequency instabilities in aero-engines [27]. It has been observed that an acoustic field significantly alters the spray characteristics such as droplet size, distribution, and trajectories [28, 29]. Further research is necessary for characterisation of spray response, instability behaviour, and validation of numerical models [28, 30].

To this end, procedures were to be established for experimentally determining the flame's dynamic response to acoustic perturbations in a single burner test rig. The simpler case of premixed natural gas combustion was opted as a starting point with the aim of later extending these methods to Kerosene flame.

1.3 Empirical Modelling using Proper Orthogonal Decomposition (POD)

Given the time required and complexity of measuring flame response under different operating conditions, it is always desirable to develop a model based on few measurements. This can then be used to predict the stability characteristics for any desired operating condition, for instance thermal power and air ratio [31].

Scaling rules have been used for this purpose in which the flame response is correlated to operating conditions through an intermediate parameter (such as flame length, see [22, 32].) These methods, however, require physical considerations and identification of additional parameter(s). A simpler modelling technique solely based on the empirical data is sought.

Proper Orthogonal Decomposition (POD) offers such an alternative. This mathematical tool has been used to develop Reduced Order Models (ROMs), such as, for predicting temperature fields in heat transfer problems under desired conditions [33–36]. Moreover, many applications are reported for estimation of flow-field around aerofoils at desired Mach numbers and angles of attack. [37–39]. POD ROMs have also been used to increase temporal or spatial resolution of Particle Image Velocimetry (PIV) data [40–43].

Further to estimations, POD can also be used to decompose a given field into modes, each representing a specific feature. This has been used for studying dynamical systems. For instance, coherent structures in turbulent flows have been identified through POD of PIV images [44, 45]. Recently, it is used to decompose flame images into spatial modes associated

with excited flames [46–48].

Little work is reported for application of POD to quantities representing the flame response, such as flame transfer functions. Zahn demonstrated the use of POD for estimating the phase of transfer functions at desired thermal power and air ratio [49]. Further validation for estimating the complete flame response was required. Moreover, possibility of decomposing the transfer function into physically relevant modes needed to be explored.

1.4 Thesis Objectives and Outline

This study aimed to measure and model flame dynamics for a perfectly premixed natural gas flame. Specifically, it entailed the following objectives:

1. Measure flame dynamics in terms of transfer function and evaluate its variation with operating conditions.
2. Assess and possibly improve the quality of results.
3. Model variation in flame dynamics with operating conditions for prediction at desired operating points and decomposition into individual contributions.

Quality of the results was assessed in terms of reproducibility and sensitivity to measurement location. The method for estimating temperatures required for evaluation of transfer functions was improved. Variation in flame dynamics with the operating conditions was described in terms of physical sensitivity mechanisms. Further to reconstruction at desired operating point, the modelling was aimed at decomposing the net flame response into contributions from different sensitivity mechanisms.

The thesis is structured as follows: Chapter 2 provides the definitions of relevant terms, underlying assumptions, and mathematical formulations. Description of the experimental hardware and techniques employed for measurements are given in Chapter 3. Chapter 4 explains the methodology used for the evaluation of measured data. Major results and a discussion on quality assessment as well as variation of flame dynamics with the operating conditions are furnished in Chapter 5. The results of empirical modelling along with an interpretation of modal decomposition can be found in Chapter 6. Finally, a summary of important conclusions and future recommendations are given in Chapter 7.

2 Theoretical Basis

The subject of thermoacoustics overlaps between acoustics and combustion science. For a basic understanding, equations describing the wave propagation in ducts and notion of network modelling is outlined first. In Section 2.2, concepts and mathematical treatment for longitudinal thermoacoustics are presented. Theory of Proper Orthogonal Decomposition (POD) is given in Section 2.3.

2.1 Linear 1D Acoustics in Ducts

Guided waves bounded by walls can form or be forced in ducts having a mean flow. They produce acoustic perturbations in the flow variables. If the perturbations are considerably smaller than their time-averaged values, higher order terms of perturbed variables are ignored and the analysis is said to be *linear* [50]. Moreover, when viscous effects at the walls are negligible, *plane waves* uniform throughout the cross-section are formed [51]. Thus the problem becomes one-dimensional and measurement, such as of pressure perturbation, only at the wall is sufficient [52].

2.1.1 Governing Equations

In order to establish basic working equations describing the wave propagation, consider a duct segment with constant cross-section as shown in Figure 2.1. Air is supplied far upstream such that the flow is fully developed with a steady velocity $\bar{u}$ in the considered segment. An excitation source, such as a speaker, produces plane acoustic waves in the flowing medium, giving rise to pressure and velocity perturbations p' and u' over their respective means $\bar{p}$ and $\bar{u}$. Note that u' represents a vector field as shown under the coloured distribution.

The pressure and velocity can then be written as[1]:

$$p(x,t) = \bar{p} + p'(x,t) \tag{2.1}$$

$$u(x,t) = \bar{u} + u'(x,t) \tag{2.2}$$

[1] When the flow is turbulent, fluctuations due to turbulence and acoustics coexist. However, turbulence usually results in a broadband incoherent noise [13]. We assumed it to be much smaller than acoustic amplitudes and therefore did not consider.

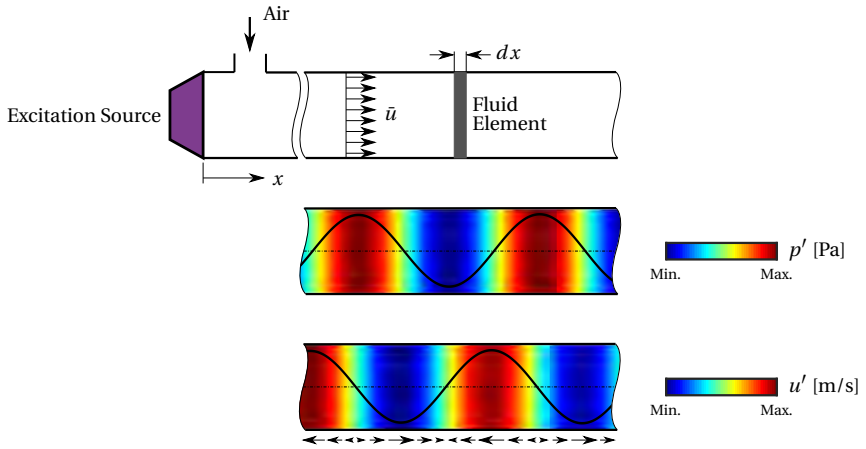

Figure 2.1: *Plane waves in a duct with mean flow of air*

From conservation of mass, momentum, and energy for a differential fluid parcel of thickness dx (see Figure 2.1), the *convective wave equation* can be obtained [16, 53, 54]:

$$\left(\frac{\partial}{\partial t}+\bar{u}\frac{\partial}{\partial x}\right)^2 p' - c^2\frac{\partial^2 p'}{\partial x^2} = 0 \tag{2.3}$$

Where c is the speed of sound[2]. This equation assumes ideal gas behaviour, isentropic compression and rarefaction with small amplitudes, a spatially constant $\bar{u}$, rigid duct walls, no source for mass, momentum, and energy.

The wave equation can be solved analytically using d'Alembert's method for p' and u' as [53, 54, 56]:

$$\frac{p'(x,t)}{\rho c} = f(x-(c+\bar{u})t) + g(x+(c-\bar{u})t) \tag{2.4}$$

$$u'(x,t) = f(x-(c+\bar{u})t) - g(x+(c-\bar{u})t) \tag{2.5}$$

Where, f and g are arbitrary functions called *Riemann Invariants*. They can be thought as upstream (f) and downstream (g) travelling waves of the same frequency and depend upon the initial and boundary conditions [52–54]. Thus, p' is the scalar superposition of these two waves and u' is their vector sum [55].

Assuming the f and g functions to have harmonic time dependence, they can be written in complex notation as:

$$f(x,t) = Re(\hat{f}_r e^{i(t-x/(c+\bar{u})+\phi_f)}) \tag{2.6}$$

$$g(x,t) = Re(\hat{g}_r e^{i(t+x/(c-\bar{u})+\phi_g)}) \tag{2.7}$$

Where subscript r denotes the real amplitude, and ϕ represents phase angle. The real (Re) operator is usually not written. It is convenient to use complex amplitudes instead of real

[2] For an ideal gas, $c = \sqrt{\gamma RT}$ [55]. Where γ is the specific heat ratio and R is the gas constant.

amplitudes and phase angles [16]:

$$\hat{f} = \hat{f}_r e^{i\phi_f} \tag{2.8}$$

$$\hat{g} = \hat{g}_r e^{i\phi_g} \tag{2.9}$$

The Equations 2.6 and 2.7 can then be written as:

$$f(x,t) = \hat{f} e^{i(t-x/(c+\bar{u}))} = \hat{f} \cdot e^{-ik^+x} \tag{2.10}$$

$$g(x,t) = \hat{g} e^{i(t+x/(c-\bar{u}))} = \hat{g} \cdot e^{+ik^-x} \tag{2.11}$$

Where k^+ represents the *wave number*[3] in the direction of flow and k^- denotes the wave number opposite to the flow direction:

$$k^{\pm} = \frac{\omega}{c \pm u} \tag{2.12}$$

Since f and g are assumed to be harmonic, p' and u' will also be harmonic functions of space and time. Using Equations 2.6 and 2.7 in Equations 2.4 and 2.5, p' and u' can be expressed in terms of $\hat{f}$ and $\hat{g}$ at a fixed frequency ω as:

$$\frac{p'(x,t)}{\rho c} = \hat{f} \cdot e^{(i\omega t - ik^+x)} + \hat{g} \cdot e^{(i\omega t + ik^-x)} \tag{2.13}$$

$$u'(x,t) = \hat{f} \cdot e^{(i\omega t - ik^+x)} - \hat{g} \cdot e^{(i\omega t + ik^-x)} \tag{2.14}$$

Equations 2.13 and 2.14 are the fundamental equations describing the 1D propagation of acoustic waves in ducts [53, 54]. In these equations, p' is normalised by ρc to make the two equations consistent in units. These equations can also be written in frequency domain as:

$$\frac{p'(x,\omega)}{\rho c} = \hat{f} \cdot e^{-ik^+x} + \hat{g} \cdot e^{+ik^-x} \tag{2.15}$$

$$u'(x,\omega) = \hat{f} \cdot e^{-ik^+x} - \hat{g} \cdot e^{+ik^-x} \tag{2.16}$$

Since p' and u' are functions of $\hat{f}$ and $\hat{g}$, different types of waves can form in the duct depending upon the amplitudes of Riemann invariants [50, 55]. For a given frequency ω, exemplary snapshots of possible harmonic waves in a duct at time t are shown in Figure 2.2.

Pure travelling waves result in the absence of downstream (Figure 2.2(a)) or upstream (Figure 2.2(b)) Riemann invariants. In that case $u' = \mp p'/(\rho c)$, where "$-$" is valid when $\hat{f} = 0$ and "$+$" applies for $\hat{g} = 0$ [50, 54]. When the two Riemann invariants have equal amplitudes, a *pure standing wave* is formed as depicted in Figure 2.2(c). It is characterised by *nodes* and *antinodes*. A mixed *standing+travelling wave* is produced in the more general case of unequal amplitudes of Riemann invariants as shown in Figure 2.2(d).

[3] In contrast to the temporal frequency (number of cycles in a unit time), the wave number represents spatial frequency (number of cycles in a unit distance) of a wave [57].

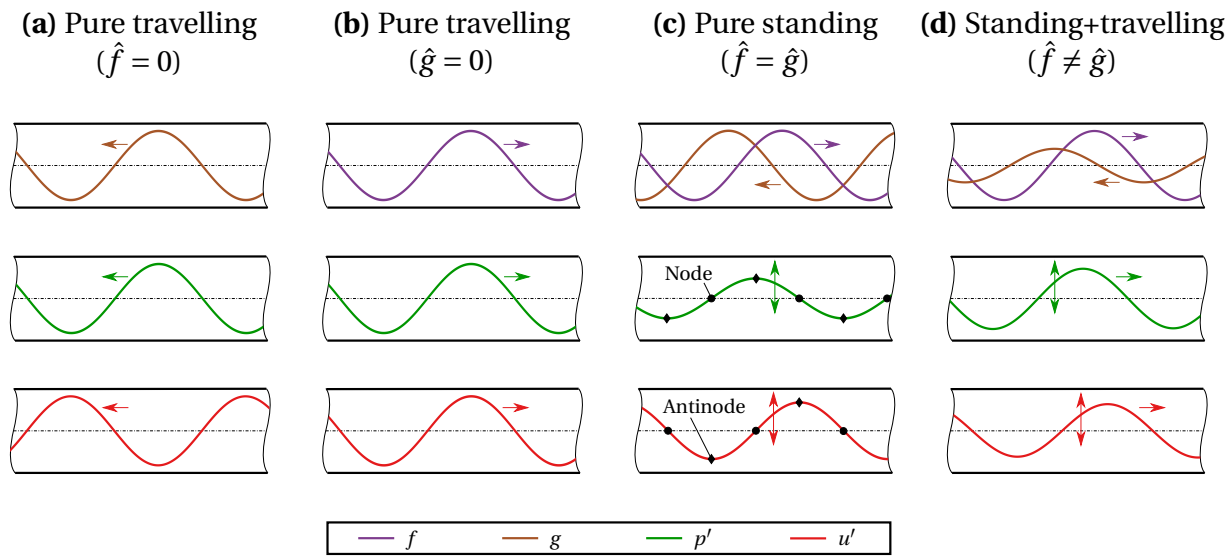

Figure 2.2: *Types of p', u' waves depending upon amplitudes of Riemann invariants ($\hat{f}$, $\hat{g}$)*

2.1.2 Network Modelling and Transfer Matrices

When different acoustic components are connected in series, the acoustic field altered by one component becomes inlet condition for the other. Therefore, it is convenient to consider the problem as a *network* of connected acoustic elements [52, 53]. A specimen for the physical problem and its network is shown in Figure 2.3(a).

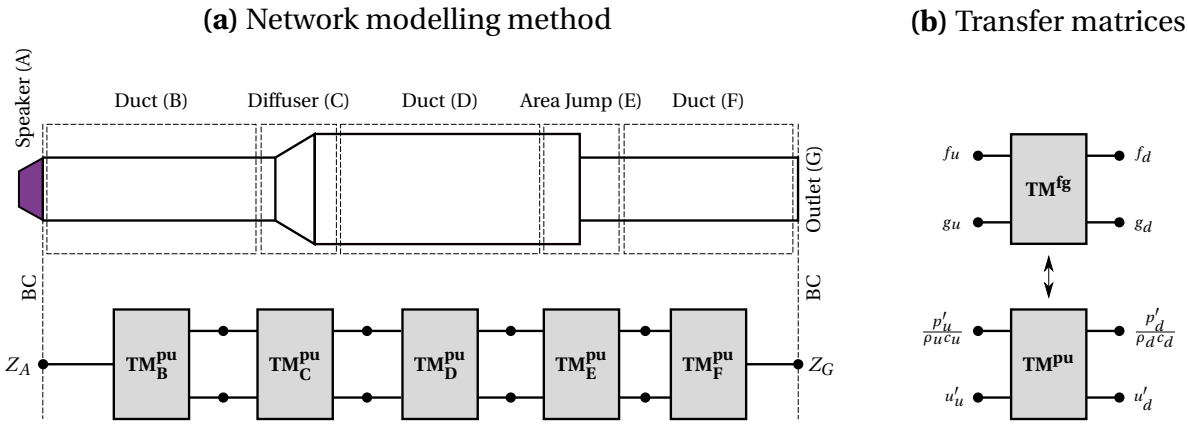

Figure 2.3: *Concept of network modelling and transfer matrices*

Each element is characterised by its *Transfer Matrix (TM)* which relates the acoustic state upstream (u) to that at downstream (d). The generic transfer matrix can be written in pu notation as:

$$\begin{pmatrix} \frac{p'}{\rho c} \\ u' \end{pmatrix}_d = \underbrace{\begin{pmatrix} \mathrm{TM}_{11}^{pu} & \mathrm{TM}_{12}^{pu} \\ \mathrm{TM}_{21}^{pu} & \mathrm{TM}_{22}^{pu} \end{pmatrix}}_{\mathbf{TM^{pu}}} \cdot \begin{pmatrix} \frac{p'}{\rho c} \\ u' \end{pmatrix}_u \tag{2.17}$$

Equivalently, the transfer matrix can also be represented in fg notation as:

$$\begin{pmatrix} f \\ g \end{pmatrix}_d = \underbrace{\begin{pmatrix} \mathrm{TM}_{11}^{fg} & \mathrm{TM}_{12}^{fg} \\ \mathrm{TM}_{21}^{fg} & \mathrm{TM}_{22}^{fg} \end{pmatrix}}_{\mathbf{TM^{fg}}} \cdot \begin{pmatrix} f \\ g \end{pmatrix}_u \tag{2.18}$$

Thus, each acoustic element is represented as an acoustic two-port with two inputs and two outputs as shown in Figure 2.3(b). Through a linear coordinate transformation matrix:

$$\mathbf{\Omega} = \begin{pmatrix} 1 & 1 \\ 1 & -1 \end{pmatrix} \tag{2.19}$$

one form can be converted into another as:

$$\mathbf{TM^{pu}} = \mathbf{\Omega} \cdot \mathbf{TM^{fg}} \cdot \mathbf{\Omega}^{-1} \tag{2.20}$$

$$\mathbf{TM^{fg}} = \mathbf{\Omega}^{-1} \cdot \mathbf{TM^{pu}} \cdot \mathbf{\Omega} \tag{2.21}$$

As shown in Figure 2.3(a), a *Boundary Condition (BC)* is characterised by *specific acoustic impedance Z*. It quantifies the extent by which motion imposed by a pressure disturbance is impeded [50, 54]. It is the ratio of pressure to velocity perturbations, normalised by ρc to make it a dimensionless quantity:

$$Z = \frac{p'/\rho c}{u'} \tag{2.22}$$

For instance, a rigid wall ($u' = 0$) has $Z = \infty$ and an open end ($p' = 0$) has $Z = 0$. A non-reflecting boundary having no impact on acoustic fields is characterised by $Z = 1$.

It is possible to determine the transfer matrix of an acoustic element from measurement of acoustic pressures as discussed next.

2.1.3 Multi-Microphone Method (MMM) for Determination of Transfer Matrices

The transfer matrix of an acoustic element can be determined experimentally by imposing a known acoustic excitation state upstream of the element and measuring its response downstream or vice versa. The TM has four unknowns (see Equation 2.17 or 2.18) whereas an acoustic state is defined by the two state variables (p', u' or f, g) corresponding to the two equations in the matrix. Therefore, two linearly independent states are required to determine the four unknowns. This can be achieved by using the *Two-Source Location Technique* [58, 59] in which acoustic excitation is imposed first at upstream and then at downstream with the same frequency. The Riemann invariants f and g are mathematical quantities and cannot be measured directly. Although p' and u' both can be directly measured, the measurement

of p' is more convenient than u' [18, 31]. Therefore, a method solely based on the measurement of p' known as *Multi-Microphone Method* [60, 61] is commonly used for determination of transfer matrices using two excitation sources.

The arrangement for this method is shown in Figure 2.4. The acoustic element is connected to upstream and downstream ducts, each equipped with a source of acoustic excitation such as a siren and multiple microphones. In this study, three microphones were used on each side. Excitation is provided first from far upstream (A) and then from downstream (B). Figure 2.4 shows exemplary upstream excitation, for downstream see Figure 4.2(c). p' is measured using microphones at multiple locations (x_j) in the upstream (subscript us) and downstream (subscript us) ducts for each forcing[4]. Analytical solution of the convective wave equation (Equation 2.15) allows determination of the Riemann invariants f, g and reconstruction of the complete acoustic wave in the ducts. Knowing the Riemann invariants just upstream (x_u) and downstream (x_d) of the acoustic element for the two forcing states serves direct determination of the transfer matrix.

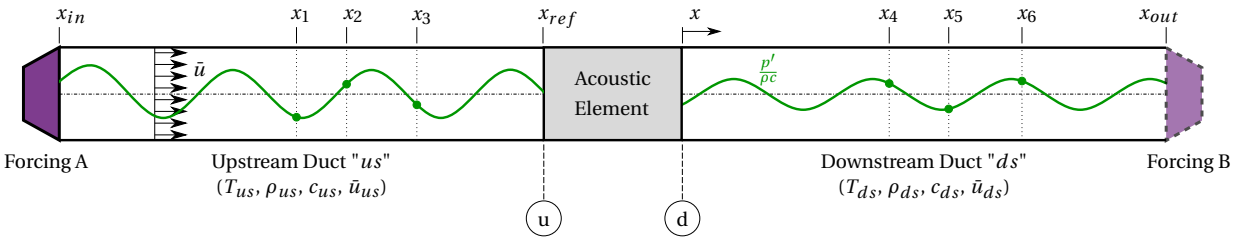

Figure 2.4: *Determination of transfer matrix using Multi-Microphone Method*

In order to elaborate the procedure, consider microphone measurements in the upstream duct for forcing A. Equation 2.15 can be written for the three locations as:

$$\frac{{p'}_1^A(\omega)}{\rho_{us} c_{us}} = \hat{f}_{us}^A(\omega) \cdot e^{-ik^+(x_1 - x_{ref})} + \hat{g}_{us}^A(\omega) \cdot e^{+ik^-(x_1 - x_{ref})} \tag{2.23}$$

$$\frac{{p'}_2^A(\omega)}{\rho_{us} c_{us}} = \hat{f}_{us}^A(\omega) \cdot e^{-ik^+(x_2 - x_{ref})} + \hat{g}_{us}^A(\omega) \cdot e^{+ik^-(x_2 - x_{ref})} \tag{2.24}$$

$$\frac{{p'}_3^A(\omega)}{\rho_{us} c_{us}} = \hat{f}_{us}^A(\omega) \cdot e^{-ik^+(x_3 - x_{ref})} + \hat{g}_{us}^A(\omega) \cdot e^{+ik^-(x_3 - x_{ref})} \tag{2.25}$$

Here ${p'}_j^A(\omega)$ represents the FFT of j-th pressure measurement at frequency ω as mentioned in Section 3.3.1. ρ_{us} and c_{us} are respectively the density and speed of sound valid throughout the upstream duct at mean temperature T_{us}[5]. Coordinates of microphone locations in the upstream duct are subtracted from $x_{ref} = x_u$ in order to reconstruct the upstream wave with origin at x_u. The wave reconstructed at downstream side has origin at $x_d = 0$. Equations 2.23-

[4] Subscripts u, d belong to stations just upstream and downstream of the acoustic element. Subscripts us, ds refer to the whole lengths of the upstream and downstream ducts.

[5] See Section 4.3.1 for details on the temperature profile and assumptions.

2.25 can be written in matrix form as:

$$\frac{1}{\rho_{us}c_{us}}\underbrace{\begin{pmatrix} p_1'^A(\omega) \\ p_2'^A(\omega) \\ p_3'^A(\omega) \end{pmatrix}}_{\mathbf{p'^A_{us}}} = \underbrace{\begin{pmatrix} e^{-ik^+(x_1-x_{ref})} & e^{+ik^-(x_1-x_{ref})} \\ e^{-ik^+(x_2-x_{ref})} & e^{+ik^-(x_2-x_{ref})} \\ e^{-ik^+(x_3-x_{ref})} & e^{+ik^-(x_3-x_{ref})} \end{pmatrix}}_{\mathbf{H_{us}}} \cdot \begin{pmatrix} \hat{f}^A_{us}(\omega) \\ \hat{g}^A_{us}(\omega) \end{pmatrix} \tag{2.26}$$

This set of equations can now be solved for $\hat{f}^A_{us}, \hat{g}^A_{us}$. However, the system is overdetermined, it has two unknowns with three equations. Therefore, a least square method is used to solve the system by minimising the *Sum of Squares Error (SSE)* between the measured data $p_j'^A(\omega)$ (left side of Equation 2.26) and its model given by the right side of Equation 2.26. It can be shown that this method translates to the following result for Riemann invariants [62]:

$$\begin{pmatrix} \hat{f}^A_{us}(\omega) \\ \hat{g}^A_{us}(\omega) \end{pmatrix} = \frac{1}{\rho_{us}c_{us}} (\mathbf{H_{us}})^\dagger \cdot \mathbf{p'^A_{us}} \tag{2.27}$$

Where † denotes the pseudo inverse of a matrix and is defined as:

$$\mathbf{H}^\dagger = \left(\mathbf{H}^\intercal \cdot \mathbf{H}\right)^{-1} \cdot \mathbf{H}^\intercal \tag{2.28}$$

Here $\intercal$ represents the matrix transpose.

The formulation in Equations 2.23-2.27 can be repeated for forcing B, the $\mathbf{H_{us}}$ matrix remains the same. The four resulting Riemann invariants can be written in the matrix form as:

$$\begin{pmatrix} \hat{f}^A_{us}(\omega) & \hat{f}^B_{us}(\omega) \\ \hat{g}^A_{us}(\omega) & \hat{g}^B_{us}(\omega) \end{pmatrix} = \frac{1}{\rho_{us}c_{us}} (\mathbf{H_{us}})^\dagger \cdot \underbrace{\begin{pmatrix} p_1'^A(\omega) & p_1'^B(\omega) \\ p_2'^A(\omega) & p_2'^B(\omega) \\ p_3'^A(\omega) & p_3'^B(\omega) \end{pmatrix}}_{\mathbf{p'_{us}}} \tag{2.29}$$

Similarly, the amplitude of Riemann invariants in the downstream duct can be evaluated for each forcing using downstream coordinates and conditions:

$$\begin{pmatrix} \hat{f}^A_{ds}(\omega) & \hat{f}^B_{ds}(\omega) \\ \hat{g}^A_{ds}(\omega) & \hat{g}^B_{ds}(\omega) \end{pmatrix} = \frac{1}{\rho_{ds}c_{ds}} (\mathbf{H_{ds}})^\dagger \cdot \underbrace{\begin{pmatrix} p_4'^A(\omega) & p_4'^B(\omega) \\ p_5'^A(\omega) & p_5'^B(\omega) \\ p_6'^A(\omega) & p_6'^B(\omega) \end{pmatrix}}_{\mathbf{p'_{ds}}} \tag{2.30}$$

It is worth noting that the Riemann invariants f, g at station "u" are equal to their respective complex amplitudes in the upstream duct us:

$$f^A_u(x_{ref},\omega) = \hat{f}^A_{us}(\omega) \cdot e^{-ik^+(x_{ref}-x_{ref})} = \hat{f}^A_{us}(\omega) \tag{2.31}$$

$$g^A_u(x_{ref},\omega) = \hat{g}^A_{us}(\omega) \cdot e^{-ik^+(x_{ref}-x_{ref})} = \hat{g}^A_{us}(\omega) \tag{2.32}$$

Same is true for station d and amplitudes in the downstream duct, for both the forcing conditions. Therefore, Equations 2.29 and 2.30 represent the acoustic state just upstream and downstream of the acoustic element. The two are related to by the transfer matrix Equation 2.18 for each forcing and can be written in a single matrix equation as:

$$\begin{pmatrix} f_d^A(\omega) & f_d^B(\omega) \\ g_d^A(\omega) & g_d^B(\omega) \end{pmatrix} = \begin{pmatrix} \mathrm{TM}_{11}^{fg} & \mathrm{TM}_{12}^{fg} \\ \mathrm{TM}_{21}^{fg} & \mathrm{TM}_{22}^{fg} \end{pmatrix} \cdot \begin{pmatrix} f_u^A(\omega) & f_u^B(\omega) \\ g_u^A(\omega) & g_u^B(\omega) \end{pmatrix} \tag{2.33}$$

Solving it for the transfer matrix yields:

$$\begin{pmatrix} \mathrm{TM}_{11}^{fg}(\omega) & \mathrm{TM}_{12}^{fg}(\omega) \\ \mathrm{TM}_{21}^{fg}(\omega) & \mathrm{TM}_{22}^{fg}(\omega) \end{pmatrix} = \begin{pmatrix} f_d^A(\omega) & f_d^B(\omega) \\ g_d^A(\omega) & g_d^B(\omega) \end{pmatrix} \cdot \begin{pmatrix} f_u^A(\omega) & f_u^B(\omega) \\ g_u^A(\omega) & g_u^B(\omega) \end{pmatrix}^{-1} \tag{2.34}$$

This procedure can be repeated for all the frequencies to obtain a frequency dependent transfer matrix in fg notation. The linear transformation in Equation 2.20 can then be used to obtain the transfer matrices in pu notation.

Mathematically, only two equations in the matrix 2.26 are required to solve for the two unknowns on each side of the acoustic element and there exist a *Two Microphone Method* [63, 64]. However, increasing the number of microphones helps in reducing the background noise and offers better wave reconstruction [31].

2.2 Longitudinal Thermoacoustics in Premixed Combustion

2.2.1 Conditions for Self-Sustained Oscillations

The thermoacoustic feedback loop mentioned in Figure 1.5 is actively established when two conditions are met. The first condition is a constructive interaction between unsteady heat release rate per unit volume $\dot{Q}'_V$ and local acoustic pressure p' over a cycle period t_0. For a combustor of volume V, $\dot{Q}'_V$ and p' interact constructively if the following inequality is true [54, 65]:

$$\int_V \left(\oint_{t_0} p' \dot{Q}'_V \, dt \right) dV > 0 \tag{2.35}$$

The above equation is known as *Rayleigh Criterion* [65, 66] and is illustrated for a given combustor location in Figure 2.5. Unsteady heat release can energise the acoustic field and make the system potentially unstable when this criterion is valid. It translates to a phase difference of less than 0.5π rad between p' and $\dot{Q}'_V$ as shown in Figure 2.5(b). When the criterion is invalid, the system remains stable.

The second condition is adequate supply of energy from the heat source to the acoustic field for overcoming the acoustic losses in the system [16, 65]. Sustained self-excited oscillations will result only if both the conditions are met.

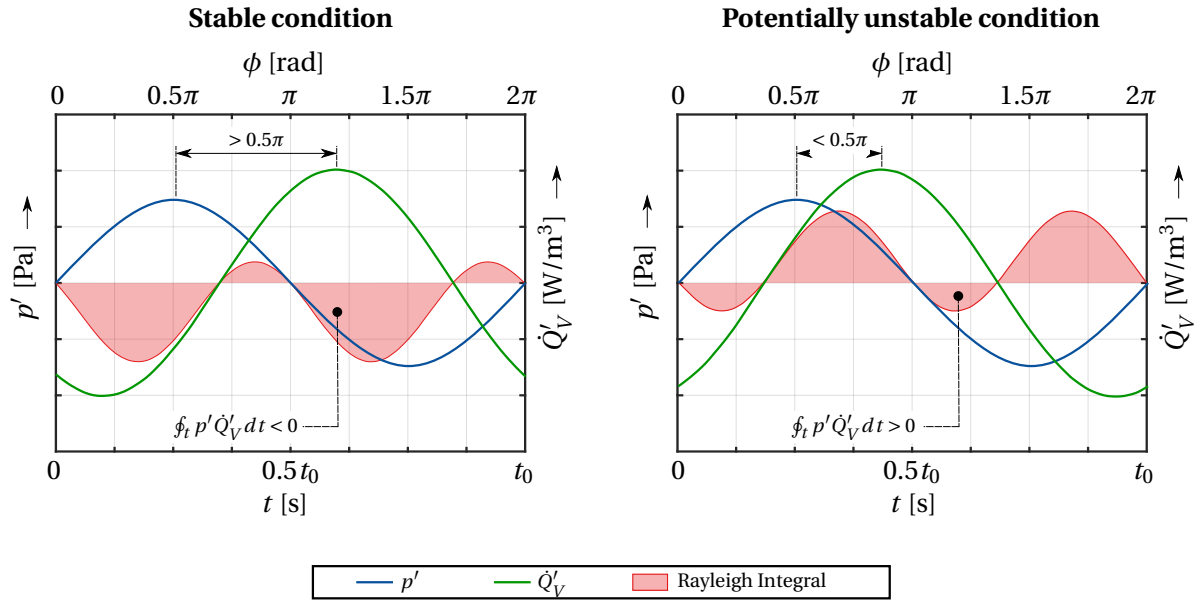

Figure 2.5: *Rayleigh criterion at a given location for stable and potentially unstable combustion*

2.2.2 Flame Response Mechanisms

Referring to Figure 1.5, multiple physical mechanisms may cause the flame to respond for a given flow field fluctuation. These response mechanisms strongly depend upon the nature of flow field and type of flame involved. For the current study, mechanisms for swirl-stabilised flames are relevant.

As shown in Figure 2.6(a), sudden expansion of a swirling flow in the wider combustor produces an *Outer Recirculation Zone (ORZ)* [67]. When the swirl number S_N[6] is above a critical value, an *Inner Recirculation Zone* is also formed due to *Vortex Breakdown (VB)* [70, 71]. Thus, the core flow is sandwiched between inner and outer recirculation zones as shown by the streamlines in upper half of Figure 2.6(a). Vortex Breakdown occurs because a diverging flow has axially decreasing azimuthal velocities (from conservation of angular momentum) which give rise to a negative azimuthal vorticity Ω_θ [72]. In turn, the azimuthal vorticity produces a negative axial velocity u_{Ω_θ} (not shown) leading to further divergence of flow, stagnation, and subsequently abrupt breakdown of the main vortex.

In premixed combustion, the flame can be considered as a front propagating against the incoming flow with an effective flame burning velocity s_F [77, 78] as depicted in the lower half of Figure 2.6(a). The variation in mean flow and flame velocities in the axial direction is indicated in Figure 2.6(b)[7]. The time-averaged flow velocity $\bar{u}$ decreases due to diverging and stagnating flow. Whereas, the flame velocity increases due to increasing turbulence in the axial direction

[6] Swirl number is a dimensionless measure of rotation in the flow. It is the ratio of axial flux of angular momentum to axial flux of axial momentum [68, 69].

[7] Figure 2.6(b) gives a sense of variation in the flow and flame velocities in axial direction. It does not strictly correspond to the flow field of Figure 2.6(a).

(a) Swirl flame features

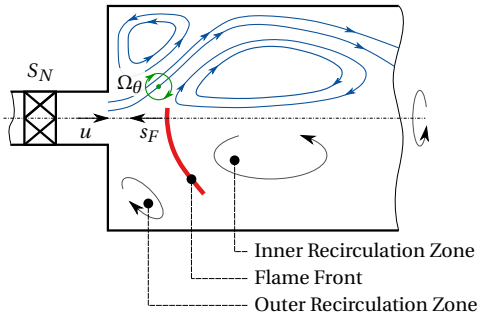

(b) Axial variation of velocities

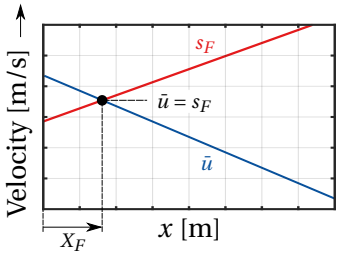

Figure 2.6: *Swirl flame features (based on [70, 73–75]), axial variation of flow and burning velocities [76]*

[77, 78]. The flame is stabilised at an axial location $x = X_F$ where the two velocities are equal [75, 76, 79]. This distance from the burner exit is known as *flame lift-off distance*. The stabilisation usually occurs near the inner recirculation zone characterised by high turbulence and low flow velocities [70, 80].

The instantaneous rate of heat release $\dot{Q}$ for a premixed flame can be expressed as [18, 20, 55, 81]:

$$\dot{Q}(t) = \int_{A_F} \rho s_F \frac{\left(\dot{m}_f/\dot{m}_a\right)_{st}}{\lambda} H_f \, dA \tag{2.36}$$

Where ρ, $\left(\dot{m}_f/\dot{m}_a\right)_{st}$, and H_f denote respectively the density, stoichiometric Fuel/Air ratio, and reaction enthalpy of fuel. The integral is evaluated over the flame area A_F.

In Equation 2.36, λ represents the ratio of actual Air/Fuel ratio to the stoichiometric Air/Fuel ratio[82, 83]:

$$\lambda = \frac{\left(\dot{m}_a/\dot{m}_f\right)}{\left(\dot{m}_a/\dot{m}_f\right)_{st}} \tag{2.37}$$

It is the reciprocal of equivalence ratio and is termed as *air ratio* in this text.

A perturbation in any of the variables on right hand side of Equation 2.36 will lead to heat release fluctuation. This may, for example, result from a perturbation in pressure, velocity, and air ratio [55]. For a homogenous mixture of fuel and air, as in perfectly premixed combus-

tion, λ remains fixed [84]. Moreover, the pressure perturbation is not important at low Mach numbers when oscillation amplitudes are low [20, 85]. Therefore, we consider only velocity-coupled mechanisms.

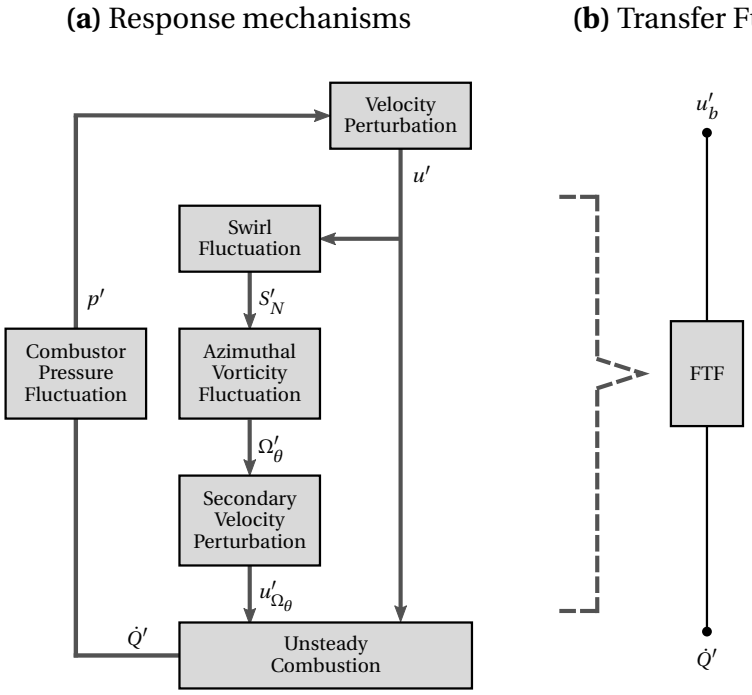

Figure 2.7: *Flowchart of flame response mechanisms (adopted from [69, 86]) and the concept of Flame Transfer Function*

A flowchart of potentially possible paths leading to heat release fluctuation is depicted in Figure 2.7. The combustor pressure fluctuation p' disturbs the flow field upstream of the flame resulting in a velocity perturbation. This disturbance may distort the flame, altering heat release rate [13, 55]. Furthermore, large-scale vortical structures may naturally exist or be acoustically excited in the shear layers between the core jet flow and recirculation zones [16, 87]. They convect with the mean flow and modulate the supply of fuel-air mixture to the flame causing heat release fluctuations. Additionally, perturbations in tangential velocity give rise to swirl number fluctuations S'_N [17, 88]. This produces a perturbation in azimuthal vorticity Ω'_θ which leads to a fluctuation in the secondary axial velocity u'_{Ω_θ} [73]. This additional disturbance is convected with the mean flow and may affect the flame heat release through similar processes described before. The net effect on flame heat release is a combination of all the active mechanisms.

The concept of Flame Transfer Function discussed next, allows encapsulating all these details into a black-box [16] as shown in Figure 2.7(b).

2.2.3 Flame Transfer Function (FTF)

The dynamic response of a flame to acoustic perturbations is quantified through a *Flame Transfer Function (FTF)*. When the unsteady heat release is assumed to result only from a velocity perturbation, it can be defined as the frequency-domain ratio of relative heat release rate fluctuation to relative velocity perturbation [55, 69]:

$$\mathrm{FTF}(\omega) = \frac{\dot{Q}'(\omega)/\bar{\dot{Q}}}{u'_b(\omega)/\bar{u}_b} \tag{2.38}$$

Where $\dot{Q}'$ is spatially integrated unsteady heat release and u'_b is the velocity perturbation at burner exit b, both are complex amplitudes (see p. 9). Therefore, the FTF is a complex quantity whose amplitude is a dimensionless ratio of relative amplitudes of $\dot{Q}'$ and u'_b, and whose phase is the phase difference between the two variables:

$$|\mathrm{FTF}(\omega)| = \frac{|\dot{Q}'(\omega)|/\bar{\dot{Q}}}{|u'_b(\omega)|/\bar{u}_b} \tag{2.39}$$

$$\angle\mathrm{FTF}(\omega) = \angle\dot{Q}'(\omega) - \angle u'_b(\omega) \tag{2.40}$$

Note that this definition is valid for perfectly premixed flames in which the flame response is supposed to be linear, that is FTF is independent of u'_b amplitude [12, 69].

In the limiting case of infinitesimally low frequency ($\omega \longrightarrow 0$), the amplitude of FTF approaches unity and its phase tends to zero. This means that the heat release fluctuates in the same amount as that of the velocity fluctuation without any delay. This is called *quasi-steady state* response of the flame [85]. Whereas, if the frequency is very high ($\omega \longrightarrow \infty$), the FTF approaches to zero with no meaningful phase. Thus, the flame becomes insensitive to velocity perturbations at very high frequencies in longitudinal modes due to high axial dispersion of the flame response [18, 89].

The FTF can be related to the TM of the flame using the theoretical relations discussed next.

2.2.4 Rankine-Hugoniot Relations for Flame Transfer Matrix (FTM)

The acoustic behaviour of the flame can be characterised through analytical relations between acoustic state (p', u') upstream and downstream of the flame [65]. In longitudinal thermoacoustics, the flame can usually be considered *acoustically compact*. A compact acoustic element has length L which is significantly smaller than the acoustic wavelength L_{ac}. Thus, the Helmholtz number is very low: $He = 2\pi L/L_{ac} << 1$ [54]. Due to compact assumption, flame thickness is irrelevant for an acoustic solution [13, 16]. This is graphically presented in Figure 2.8 which shows a compact flame having length L_F and acoustic wavelength L_{ac}.

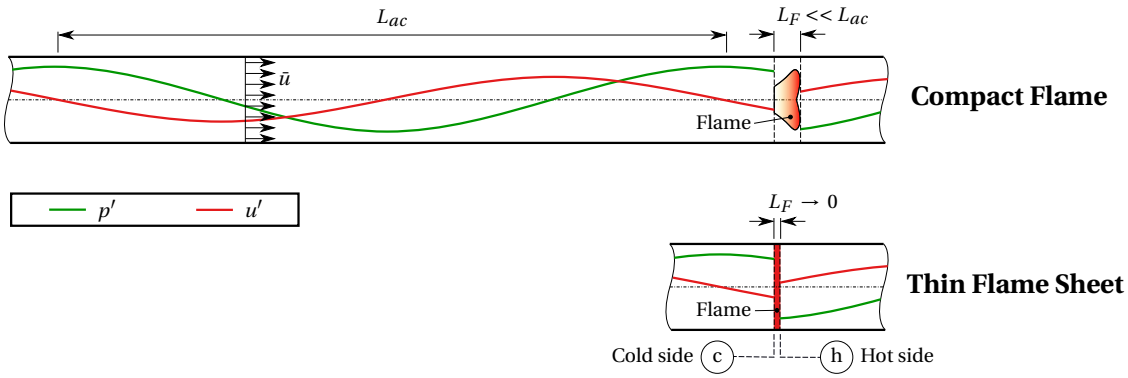

Figure 2.8: *Illustration of a compact flame and thin flame sheet*

In such a condition, the flame can be assumed to be a thin sheet of discontinuity in the reacting flow as shown in lower half of Figure 2.8 [90]. The *Rankine-Hugoniot* relations obtained from integral mass, momentum, and conservation energy equations relate the flow variables across such discontinuity and are given by [90]:

$$\frac{u_h}{u_c} = 1 + \frac{\gamma - 1}{\gamma} \frac{\dot{Q}_A}{p_c u_c} + \mathcal{O}(Ma^2) \tag{2.41}$$

$$\frac{p_h}{p_c} = 1 - (\gamma - 1) \frac{\dot{Q}_A}{p_c u_c} Ma_c^2 + \mathcal{O}(Ma^4) \tag{2.42}$$

$$\frac{T_h}{T_c} = 1 + \frac{\gamma - 1}{\gamma} \frac{\dot{Q}_A}{p_c u_c} + \mathcal{O}(Ma^2) \tag{2.43}$$

Where $\dot{Q}_A = \dot{Q}/A_F$ is the heat release rate per unit area, A_F is the effective area of the flame sheet, T is the temperature, γ is the specific heat ratio, and Ma is for Mach number. The subscripts c and h denote the upstream cold and downstream hot side respectively. Higher order Ma terms represented by $\mathcal{O}$ can be neglected [91].

The above relations are valid for total quantities of the flow variables. Decomposing them into their mean and fluctuating components (see Equations 2.1-2.2) and linearising by retaining only first order terms give the relations for acoustic states:

$$\frac{p'_h}{\bar{\rho}_h c_h} = \beta \frac{p'_c}{\bar{\rho}_c c_c} - \beta T_r Ma_c \left(1 + \frac{\dot{Q}'_A / \bar{\dot{Q}}_A}{u'_c / \bar{u}_c}\right) u'_c \tag{2.44}$$

$$u'_h = -T_r \gamma Ma_c u'_c \frac{p'_c}{\bar{\rho}_c c_c} + \left(1 + \frac{\dot{Q}'_A / \bar{\dot{Q}}_A}{u'_c / \bar{u}_c}\right) u'_c \tag{2.45}$$

Where β and T_r are ratio of specific impedances and relative temperature rise respectively:

$$\beta = \frac{\bar{\rho}_c c_c}{\bar{\rho}_h c_h} \tag{2.46}$$

$$T_r = \frac{T_h}{T_c} - 1 \tag{2.47}$$

Using the corollary $\dot{Q}'_A/\bar{\dot{Q}}_A = \dot{Q}'/\bar{\dot{Q}}$ in the definition of FTF (Equation 2.38), the cold and hot side acoustic states can be related through the *Flame Transfer Matrix (FTM)* as:

$$\begin{pmatrix} \frac{p'}{\rho c} \\ u' \end{pmatrix}_h = \underbrace{\begin{pmatrix} \beta & -\beta T_r Ma(1+\mathrm{FTF}) \\ -T_r \gamma Ma & 1+T_r \mathrm{FTF} \end{pmatrix}}_{\mathbf{FTM^{pu}}} \begin{pmatrix} \frac{p'}{\rho c} \\ u' \end{pmatrix}_c \tag{2.48}$$

Since gas turbines generally involve low Mach numbers [65], Equation 2.48 can be simplified as:

$$\begin{pmatrix} \frac{p'}{\rho c} \\ u' \end{pmatrix}_h = \underbrace{\begin{pmatrix} \beta & 0 \\ 0 & 1+T_r \mathrm{FTF} \end{pmatrix}}_{\mathbf{FTM^{pu}}} \begin{pmatrix} \frac{p'}{\rho c} \\ u' \end{pmatrix}_c \tag{2.49}$$

2.3 Proper Orthogonal Decomposition

Proper Orthogonal Decomposition (POD) is a statistical tool to deal with data samples in which each observation is a distribution instead of a single value [92–94]. It decomposes a given dependent variable, such as a physical field $v(\psi, w)$ distributed in space w and the distribution changing in space ψ, into a linear combination of deterministic basis functions [94]:

$$v(\psi, w) = \sum_{j=1}^{\infty} a_j(\psi)\theta_j(w) \tag{2.50}$$

Thus, POD expands a given function into a linear series of basis functions $\theta(w)$ weighted by their respective coefficients $a_j(\psi)$. The basis functions are in the distribution space (such as 2D coordinate space) whereas the coefficients signify the change in distribution with ψ (for instance time.)

Mathematics of POD will be briefly described here for a discrete ensemble of data **V**. The data matrix for m measurements each corresponding to a distribution over n elements can be written in terms of POD modes and coefficients as:

$$\underbrace{\begin{pmatrix} v(\psi_1, w_1) & \dots & v(\psi_1, w_n) \\ \dots & \dots & \dots \\ v(\psi_m, w_1) & \dots & v(\psi_m, w_n) \end{pmatrix}}_{\mathbf{V}\,(m\times n)} = \underbrace{\begin{pmatrix} a_{11}(\psi_1) & \dots & a_{1n}(\psi_1) \\ \dots & \dots & \dots \\ a_{m1}(\psi_m) & \dots & a_{mn}(\psi_m) \end{pmatrix}}_{\mathbf{A}\,(m\times n)} \cdot \underbrace{\begin{pmatrix} \theta_{11}(w_1) & \dots & \theta_{1n}(w_1) \\ \dots & \dots & \dots \\ \theta_{n1}(w_n) & \dots & \theta_{nn}(w_n) \end{pmatrix}^{\mathsf{T}}}_{\mathbf{\Theta}\,(n\times n)} \tag{2.51}$$

Where each row of **V** contains data for one distribution. Thus, distribution changes row-wise. Each column of matrix $\mathbf{\Theta}$ is a vector representing a basis function and each column of **A** gives its corresponding coefficients. POD subjects Equation 2.50 to two conditions; *orthonormality* and *optimality* [95, 96]. The first condition demands that the basis functions are *orthogonal*.

If the basis functions are considered as vectors in n-D space, they should be normal to each other with a vector magnitude of unity:

$$\theta_i \cdot \theta_j{}^{\mathsf{T}} = \begin{cases} 1 & \text{when } \theta_i = \theta_j, \\ 0 & \text{otherwise} \end{cases} \tag{2.52}$$

With this condition, the coefficients matrix $\mathbf{A}$ can be obtained by projecting the data $\mathbf{V}$ on the basis functions [44]:

$$\mathbf{A} = \mathbf{V} \cdot \mathbf{\Theta} \tag{2.53}$$

The second condition requires that the series expansion in Equation 2.50 is *optimal*. This means that the first k terms of this series approximates the data better or as good as any other linear combination with k terms, thus the name *proper*.

The above two conditions translate into an eigenvalue problem and the unknown basis functions can be found as [44, 97]:

$$\mathbf{C} \cdot \mathbf{\Theta} = \boldsymbol{\epsilon} \cdot \mathbf{\Theta} \tag{2.54}$$

Where $\boldsymbol{\epsilon}$ is a diagonal matrix containing $min(m,n)$ non-zero eigenvalues ϵ_j and $\mathbf{\Theta}$ is a matrix of n eigenvectors θ_j arranged in columns. The eigenvectors corresponding to zero eigenvalues have no significance and are discarded. The matrix $\mathbf{C}$ represents the covariance matrix of the data ensemble:

$$\mathbf{C} = \frac{1}{m-1} \mathbf{V}^{\mathsf{T}} \cdot \mathbf{V} \tag{2.55}$$

Its diagonal terms represent the variance and off-diagonal terms represent the covariance in data with respect to ψ. Hence, basis functions are eigenvectors of the covariance matrix of the data ensemble. They signify the correlation in the data and capture distinct features present, hence also named as *modes*. The eigenvalues correspond to the data variance and its value reflects the extent of information/change captured by a mode. A higher value means the mode has a higher relevance in representing the original data. Based on these values, the Mode Relevance Index (MRI) for mode θ_j can be calculated as [98]:

$$\text{MRI}_j = \frac{\epsilon_j}{\sum_{j=1}^{n} \epsilon_j} \tag{2.56}$$

MRI helps in sorting the modes from highest relevance to the lowest. For a correlated data, the first few modes (for instance k) contain most of variance in data and are sufficient to represent the entire data ensemble. Hence, the dimensionality of the problem is reduced in that only k modes are required instead of n, therefore the name *Reduced Order Model* [44]. Usually modes representing 90% of the total data variance are retained [99].

Once the POD modes are selected, reconstruction at any desired point in space ψ requires interpolating the coefficient values at that point. Such as using first k modes, the field $v(\psi, w)$

at a desired point $\psi = \psi_z$ can be obtained as:

$$\underbrace{\begin{pmatrix} \tilde{v}(\psi_z, w_1) & \dots & \tilde{v}(\psi_z, w_n) \end{pmatrix}}_{\tilde{\mathbf{V}}\,(1\times n)} = \underbrace{\begin{pmatrix} \tilde{a}_{z1}(\psi_z) & \dots & \tilde{a}_{zk}(\psi_z) \end{pmatrix}}_{\tilde{\mathbf{A}}\,(1\times k)} \cdot \underbrace{\begin{pmatrix} \theta_{11}(w_1) & \dots & \theta_{1k}(w_1) \\ \dots & \dots & \dots \\ \theta_{n1}(w_n) & \dots & \theta_{nk}(w_n) \end{pmatrix}^{\mathsf{T}}}_{\boldsymbol{\Theta}\,(n\times k)} \tag{2.57}$$

Where "~" denotes the desired quantity. The coefficient values $\tilde{a}_{zj}$ are interpolated using the known coefficients a_{ij} from Equation 2.53.

The above method known as the *direct method* of POD is used in this study. Further details on the underlying mathematics of the procedure can be found in [100].

3 Experimental and Measurement Setup

This chapter outlines the hardware used for performing experiments and methods employed for making measurements. The single burner test rig is described in the first section. Section 3.2 discusses features of the swirl burner used in this study. Subsequently, measurement equipment and methods are elaborated in Section 3.3. The chapter closes with a description of the operating cases investigated given in Section 3.4.

3.1 Combustion Test Rig

All experiments were performed on the Instability Control of Low Emission Aero-engine Combustor (ICLEAC) single burner test rig available at the Chair of Thermodynamics, TU Munich. It was designed for studying longitudinal thermoacoustics at atmospheric pressure with a maximum thermal power of 65 kW [89]. The test rig allows performing acoustical and optical measurements for natural gas as well as Kerosene flames under conditions similar to typical gas turbine combustors, except for atmospheric pressure. The setup of the test rig is schematically shown in Figure 3.1.

The rig is an axial arrangement of plenum (11), combustor (12), and exhaust silencer with a swirl burner (10) mounted at the combustor inlet. Combustion air is drawn from a compressed air supply header. It is filtered and regulated to maintain a pressure of approximately 10 bar. After passing through a mass flow controller[1] (01) with a built-in flow meter (02), it is supplied to a 32 kW electric preheater[2] (03). The fuel used was city natural gas with a methane content of approximately 98% by volume. Similar to the air, natural gas is also regulated before being fed to the combustor through a separate flow controller[3]. It is introduced in the air stream near the outlet of the preheater to allow thorough mixing of fuel and air in the plenum, ensuring perfectly premixed conditions. Via a 3-way valve, half of the heated mixture is then supplied directly to the plenum and other half through an upstream siren (04) which modulates the flow rate. The pipes connecting preheater and plenum provide enough buffer volume for acoustically isolating the plenum from upstream infrastructure [101].

[1] Type Bronkhorst F206BI-FBD-99V, maximum air flow rate 150 g/s
[2] Type Leister 40000, maximum temperature 773 K
[3] Type Bronkhorst F-202AC-AAB-44V, maximum flow rate 190 ln/min (CH_4)

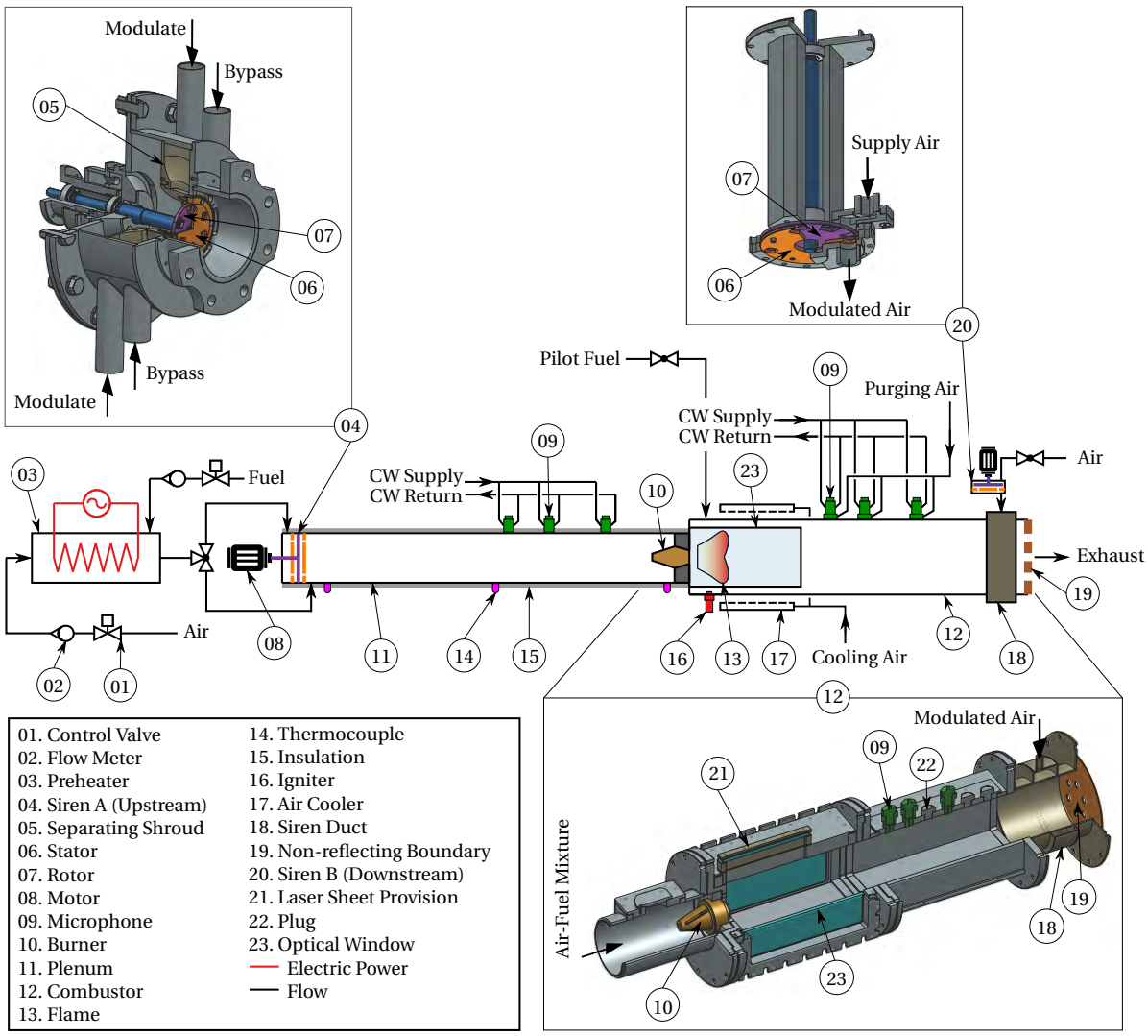

Figure 3.1: *Schematic of the ICLEAC single burner test rig*

The plenum (11) is a cylindrical pipe with a diameter of 124 mm and length of 1365 mm. This geometry allows only longitudinal modes to be formed in the desired frequency range mentioned in Section 3.4. It has fundamental natural frequency of around 175 Hz for a mean plenum temperature of 573 K used in this study [31, 86]. External insulation (15) is provided for achieving the desired plenum temperature. Three K-type thermocouples (14) are installed for monitoring the plenum temperatures. The combustor (12) has a rectangular section of 150×150 mm^2 and a length of 730 mm. It's first segment incorporates quartz glass[4] optical windows (23) on two sides with dimensions 150x300 mm^2. Ignition is achieved through a spark plug (16) flushed at the bottom wall and a pilot gas supply. Impingement air cooling is provided on the combustor walls and the optical windows. Ports for installation of microphones are furnished in the second segment having lower temperature gradients. Near the combustor exit, the downstream siren (20) is installed normal to the central axis. The modu-

[4]Type Sico Silux, thickness 8 mm

lated air from this siren is injected into the combustor via an annular cavity (18) as shown in the 3D cut-away view of the combustor. A non-reflecting boundary is used at the combustor exit for accurate measurements under external excitation [31]. A perforated plate (19) with six 20 mm diameter holes approximately serves the non-reflecting boundary condition over the frequency range of interest [21, 86].

The upstream (04) and downstream (20) sirens used for acoustic excitation consist of a combination of stator (06) and rotor (07) discs each having multiple orifices. The rotors are driven by speed-controlled electric motors not shown in the figure and the excitation frequency is determined by the speed of rotation. Since air can only pass when the orifices in the two discs align, a sinusoidal modulation of flow is achieved based on the orifice shape. Further details can be found in [31, 101].

Six piezoelectric microphones[5] (09) are provided for dynamic pressure measurement, three in the plenum and three in the combustor. Since the microphones are rated to a maximum temperature of 120°C, Cooling Water (CW) is used to prevent all the microphones from overheating. For this purpose, they are mounted with a CW adapter[6]. Additionally, the microphones installed in the combustor are provided with air purging to evade deposition of any condensate or soot forming in the combustor.

The test rig control is realised through a LabVIEW *Virtual Instrumentation (VI)* panel. It allows monitoring and setting of the desired flow-rates and preheating temperature. Another VI panel is used for control of the excitation sirens. Further details are available in [101].

3.2 Swirl Burner

The burner (10) used in this study is a 2.3:1 scaled-down version of the A^{2}EV burner developed by Sangl and Mayer [80, 102]. Its design was derived from the Alstom Advanced EnVironmental (AEV) burner (German patent no. DE19545310B4) and was optimised with respect to fuel flexibility, flame flashback safety, and NO_x reduction [102]. The burner 3D view along with its cross-section, major dimensions, and flow field are shown in Figure 3.2.

The burner consists of a divergent cone with a central hole and four tangential slots. Swirl is generated as the fluid enters through the tangential slots. The ratio of tangential and axial flow areas defines the swirl strength. The convergent mixing tube maintains the swirl strength which would otherwise increase in the downstream direction [102]. Figure 3.2(b) shows a specimen of the flow field produced by this burner. It qualitatively shows magnitude of mean axial velocity $\bar{u}_x$ normalised by mean burner exit velocity $\bar{u}_b$. As mentioned in Section 2.2.2, the features of high swirl flow can be identified. The inner and outer shear layers are formed due to large transverse velocity gradients in the region where core jet flow meets the recirculation zones.

[5] Type Piezotronics PCB-106B
[6] Type Piezotronics 064B06

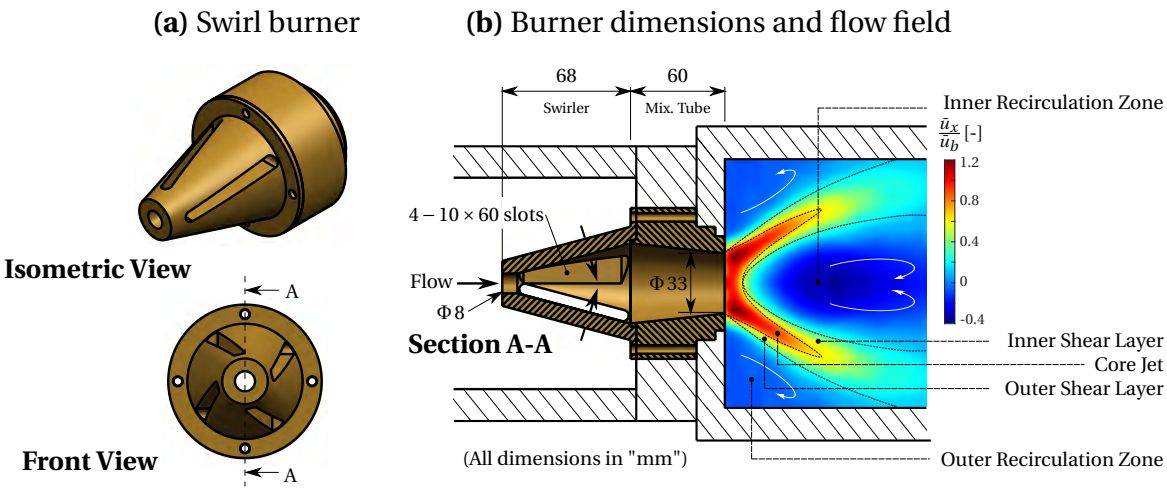

Figure 3.2: *Swirl burner geometry and flow field (PIV of exemplary flow field adopted from [102])*

3.3 Measurement Instruments and Techniques

For the current study, three measurement techniques were employed:

1. Measurement of pressure perturbation under excited condition by means of microphones.
2. OH* chemiluminescence detection for quantifying unsteady heat release rate under excitation using photomultiplier.
3. OH* chemiluminescence imaging for evaluating flame geometry under stationary (non-excited) condition using a high speed camera.

The instruments used for data acquisition and scheme employed for the measurement processes are depicted in Figure 3.3.

Details of the measuring technique, hardware, and data acquisition are explained in the following subsections.

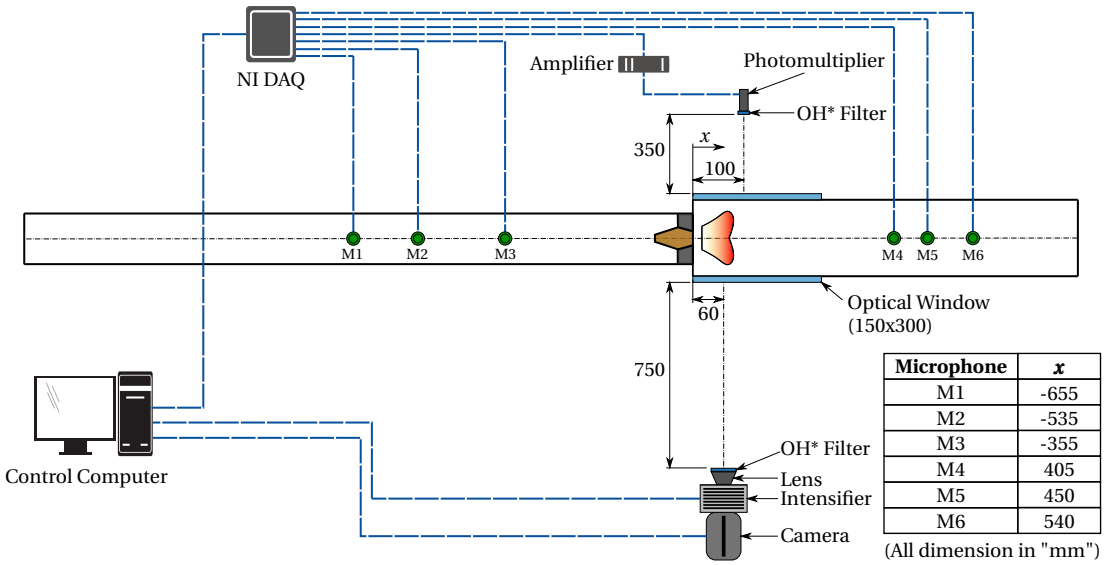

Figure 3.3: *Scheme for acoustical, optical measurements, and acquisition of data*

3.3.1 Acoustic Pressure Measurement using Microphones

Acoustic pressure was measured using the microphones (see footnote on p. 25) at an acquisition rate of 10 kHz. The microphones were positioned relative to the burner exit along the x direction as shown in Figure 3.3. The analogue signals from the microphones (M1 to M6) are gathered through a National Instruments Inc. (NI) Data Acquisitioner (DAQ) device NI-6229 and are fed to the measurement computer.

The microphones measure acoustic pressure $p'(t)$ in plenum and combustor with respect to time. An already established routine was used for acquiring the data via LabVIEW [31] as illustrated in Figure 3.4. This flowchart outlines specimen for microphone M2 with an exemplary upstream excitation (forcing A) at 380 Hz.

The excitation frequency was varied stepwise over the desired frequency range 80-640 Hz. For each frequency step, ten measurements were performed to record time series (1a) for a duration of 1 s for better averaging of acoustic pressure. The data for first measurement differ significantly from other measurements and therefore was not considered. Due to a sinusoidal excitation, the pressure recorded is almost sinusoidal as shown for the time range of 0.6-0.65 s (1b). Fast Fourier Transform (FFT) of this signal is performed in order to obtain the amplitude (2a) and phase (2b) of the harmonic components. The amplitude and phase were extracted from the FFT spectrum only at the excitation frequency [23, 103].

Thus, the complex acoustic pressure for measurement j at the excitation frequency ω_A is obtained as:

$$p'_j(\omega_A) = |p'_j(\omega_A)| \cdot e^{(\angle p'_j(\omega_A))} \tag{3.1}$$

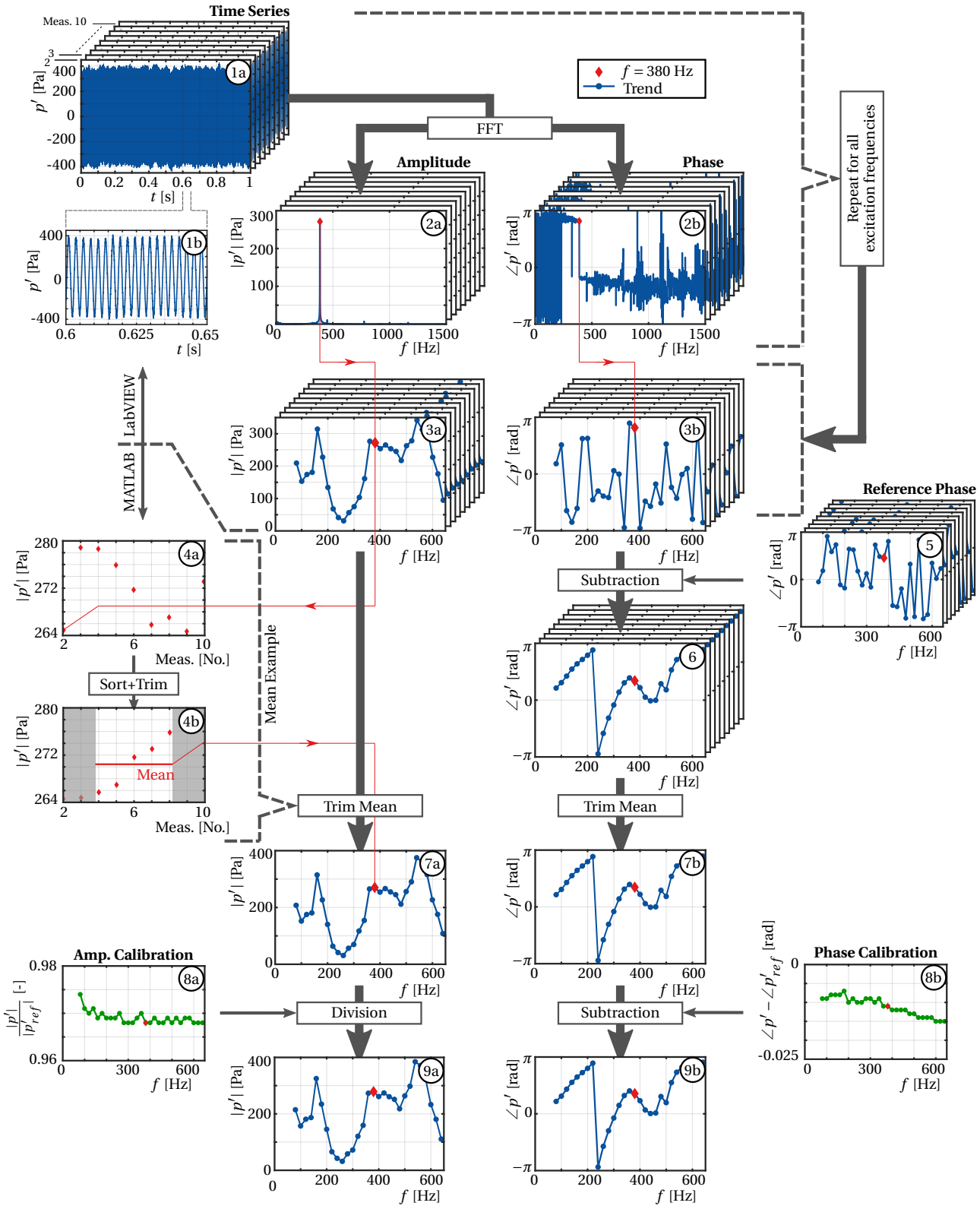

Figure 3.4: *Flowchart for acquisition of acoustic pressure data (specimen for microphone M2 with excitation frequency of 380 Hz)*

This process is repeated for all the desired frequencies to obtain the trend of acoustic pressure amplitude (3a) and phase (3b) with respect to excitation frequencies as shown in the figure. These steps are mathematically performed in the LabVIEW VI and resulting data is stored in text files. A MATLAB script was developed for further preprocessing. The phase values for all the microphones were subtracted using the phase of M6 as a common phase reference. After subtracting the reference phase (5) from the phase of M2 (3b), a definite trend (6) is observed. At a given excitation frequency, data for different measurements is averaged using *Trim Mean*[7]. To reduce relative error among the microphones, they have been calibrated against a reference microphone to yield the calibration amplitude (8a) and phase (8b) curves [31, 103]. This calibration is then applied to 7a and 7b for getting corrected amplitude (9a) and phase (9b) of the acoustic pressure for further processing described in Section 2.1.3.

When microphone measurements at multiple locations are used for wave reconstruction as described in Section 2.1.3 for Multi-Microphone Method (MMM), the relative location of the microphones is important. If the distance between subsequent microphones is an integral multiple of half wavelength, a singularity condition may occur and reconstruction may not be possible [61]. For instance, the microphones may coincide with the nodes of standing waves as shown in Figure 3.5(a) for two microphones.

(a) Two Microphones

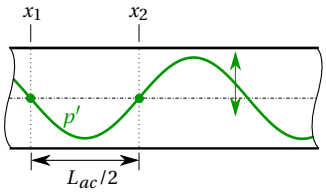

Singular

(b) Three Microphones (Equidistant)

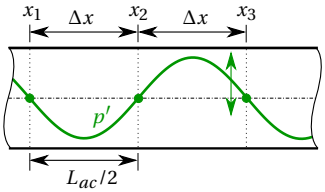

Singular

(c) Three Microphones (Non-equidistant)

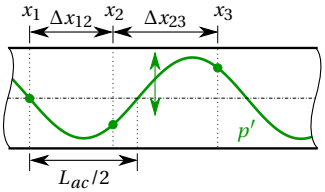

Non-Singular

Figure 3.5: *Singularity effect in wave reconstruction depending upon microphones location*

Using equidistantly placed multiple microphones does not alleviate the situation as shown in Figure 3.5(b). Therefore, the microphones should be located in a non-equidistant manner as depicted in Figure 3.5(c) such that $\Delta x_{23} > \Delta x_{12}$ is not an integral multiple of Δx_{12}. In general, it reduces the chances of producing singularity effect. Hence, the microphones were positioned non-equidistantly where possible, that is the upstream side, as shown in Figure 3.3.

[7] It is a MATLAB function in which the data is sorted in ascending order (4a) and then 50% of the highest and lowest values are neglected (4b). The average is determined only with the 50% middle values resulting in single amplitude (7a) and phase (7b) trends.

3.3.2 OH* Chemiluminescence Detection and Flame Imaging

The optical measurements were performed to record the OH* *Chemiluminescence (CL)* radiation of the flame. In a combustion process, this refers to the emission associated with chemical reactions when an intermediate species (denoted by *) transits from an excited state to its ground state [104]. For hydrocarbon flames, OH* radical gives a narrow-band, strong emission due to chemiluminescence at around 308 nm according to the reactions [18]:

$$\mathrm{HCO + O \longrightarrow CO + OH^*}$$
$$\mathrm{OH^* \longrightarrow OH + h}\nu$$

Where h is the Planck's constant and ν is the frequency of emitted photon. The rate of integral heat release in a perfectly premixed hydrocarbon flame is linearly related to OH* CL intensity [105, 106]. Therefore, it is used as an indicator for flame heat release.

The dynamic CL signal from the flame under excited condition was measured using a photomultiplier[8] at a sampling frequency of 10 kHz. For capturing only the emission from OH* radical, an Ultraviolet (UV) bandpass interference filter[9] with a maximum transmission of 16.6% at central wavelength of 309.7 nm and Full Width Half Maximum (FWHM)[10] of 10.2 nm was used. The dynamic signal is amplified before being fed to the measurement computer via the same NI DAQ device as used for the microphones.

The combination of photomultiplier and UV filter allows to monitor time series of spatially-integrated OH* CL intensity $I'(t)$ corresponding to heat release perturbation $\dot{Q}'(t)$. Since this is measured in Volts, a calibration between the measured signal and actual heat release rate is necessary. However, Freitag [18] has shown that for evaluation of FTF, direct proportionality can be assumed between the two variables:

$$\dot{Q}(t) \propto I(t) \tag{3.2}$$

Then, the relative perturbation in heat release rate can be obtained from relative perturbation in intensity:

$$\frac{\dot{Q}'(t)}{\bar{\dot{Q}}} = \frac{I'(t)}{\bar{I}} \tag{3.3}$$

Where primed variables denote the perturbations and over-bars represent mean quantities. Corresponding to each dynamic measurement, the mean intensity is measured under stationary condition. Note that $\dot{Q}'(t)$ and $I'(t)$ are complex numbers but normalisation by their respective means only affect their amplitudes, the phases remain unchanged.

The amplitude and phase of OH* CL intensity $I'(t)$ is acquired and preprocessed similar to the acoustic pressure measurement as shown in Figure 3.4, except for the correction applied

[8] Type Hamamatsu H5784-03/04
[9] Type L.O.T.-Oriel 307FS10-50
[10] Total width of the band at 50% of the maximum transmission.

through calibration (8a, 8b). Note that the phase of $I'(t)$ is also subtracted using the same common reference phase of M6.

The stationary flame was also imaged under stationary conditions using a high speed Charge Coupled Device (CCD) camera[11]. For recording the spatial distribution of OH* radiation intensity, a UV filter similar to the photomultiplier was used. An image intensifier[12] was employed along the camera axis between the CCD sensor and objective lens[13]. The camera and intensifier were directly connected to the measurement computer and were controlled through a dedicated vendor software.

For each operating condition, a set of 1000 images was captured at a rate of 125 Frames-Per-Second (FPS) corresponding to a duration of 8 s. The exposure time for each frame was set to 100 μs. The camera captured Line-Of-Sight (LOS) integrated flame images of OH* CL emission from the flame. After processing as described in Section 4.4, these images help in analysing the variation of flame dynamic response with operating conditions. Both photomultiplier and camera were positioned normal to the combustor axis as shown in Figure 3.3 such that their field of view covers the entire flame for all operating conditions.

3.4 Operating Conditions

The Operating Points (OPs) for the current study were chosen so as to investigate the influence of varying thermal power P_{th} and air ratio λ on the flame response. A summary of the test matrix is depicted in Figure 3.6.

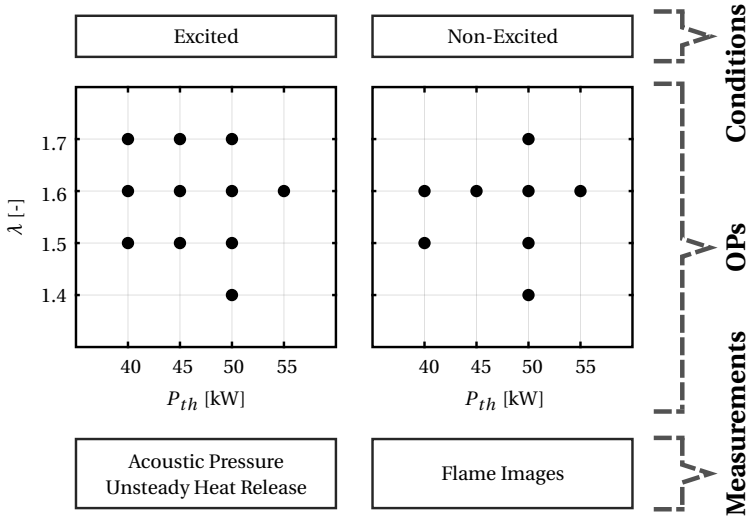

Figure 3.6: *Summary of operating points investigated*

[11] Type Photron FASTCAM SA5
[12] Type Invisible Vision UVi 1850-10
[13] Type Cerco Sodern, focal length 45 mm

For measurements of acoustic pressures and photomultiplier signal, excitation was done at frequencies in the range of 80-640 Hz with steps of 20 Hz. The effect of thermal power was investigated in the range of 40-55 kW with 5 kW increments at $\lambda = 1.6$. The influence of λ was investigated in the range of 1.4-1.7 in the steps of 0.1 at a fixed $P_{th} = 50$ kW. Measurements were also done at $P_{th} = 40$ kW for $\lambda = 1.5, 1.7$, and at $P_{th} = 45$ kW for $\lambda = 1.5, 1.7$. These were used for reduced order modelling and better estimation of temperatures required for evaluation of FTFs.

Flame images were acquired without excitation for thermal power in the range of 40-55 kW with 5 kW increments at $\lambda = 1.6$. Similarly, λ was varied in the range of 1.4-1.7 with increment of 0.1 at a fixed $P_{th} = 50$ kW. Flame was also imaged for $P_{th} = 40$ kW, $\lambda = 1.5$.

The preheating temperature was fixed at a mean plenum temperature of 573 K for all the measurements.

For convenience, an operating point with a thermal power $P_{th} = 45$ kW and air ratio $\lambda = 1.5$ is denoted as "45kW-1.5L".

4 Evaluation Methodology

In this chapter, methods used for evaluating the results from measured data are outlined. A flowchart summarising the calculations performed in this study is shown in Figure 4.1. All calculations are done using MATLAB scripts unless otherwise specified.

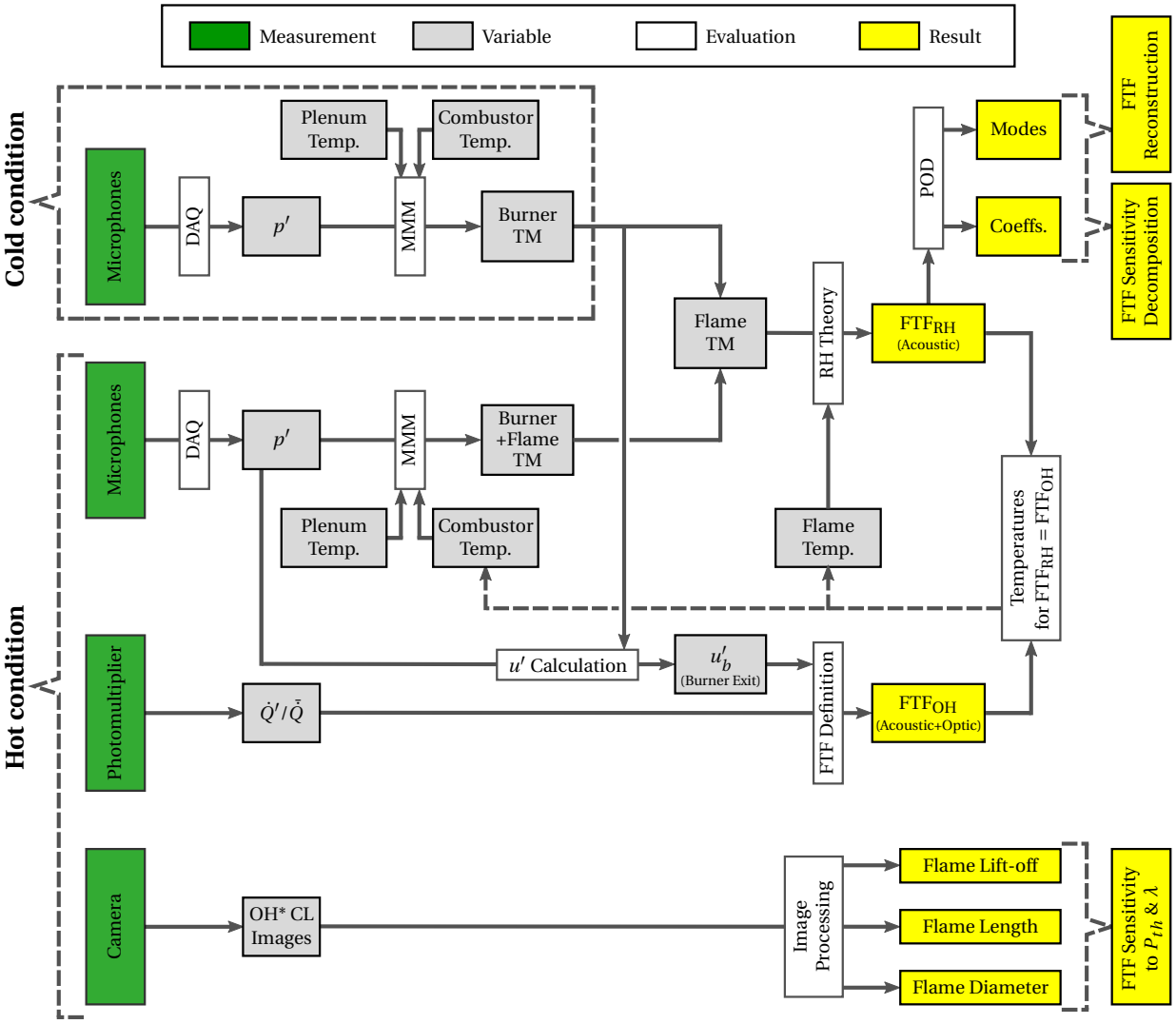

Figure 4.1: *Summary of calculations performed in this study*

The test rig is split into burner and flame acoustic elements with their respective Transfer Matrices (TMs) as described in Section 4.1. The accumulated behaviour of burner and flame

is characterised by a combined TM. Determination of these transfer matrices from acoustical measurements under cold and hot conditions is also outlined in Section 4.1. Afterwards, evaluation of FTF from acoustical-only and optical-acoustical measurements is presented in Section 4.2. Section 4.3 discusses the determination of flame and combustor temperatures required for evaluating FTFs from acoustical-only measurements. This is followed by a description for processing of flame images to evaluate the variation in flame geometric parameters with operating conditions. Finally in Section 4.5, the methodology employed for POD of FTFs for reconstruction and decomposition of FTF behaviour with thermal power as well as air ratio is furnished.

4.1 Network Model of Test Rig and Determination of Transfer Matrices

As explained in Subsection 2.1.2, the test rig was modelled as a network of connected acoustic elements as shown in Figure 4.2. Thus, it is decomposed into an upstream plenum duct, downstream combustor duct, a Burner Transfer Matrix (BTM), and a Flame Transfer Matrix (FTM). An imposed acoustic field, either from upstream or downstream siren, produces p' and u' perturbation fields in both the ducts. The transfer matrices relate the acoustic states across burner and flame at locations "a", "c", and "d" as depicted. For upstream excitation (forcing A), as shown in Figure 4.2(b), the downstream boundary is characterised by acoustic impedance Z_B and vice versa.

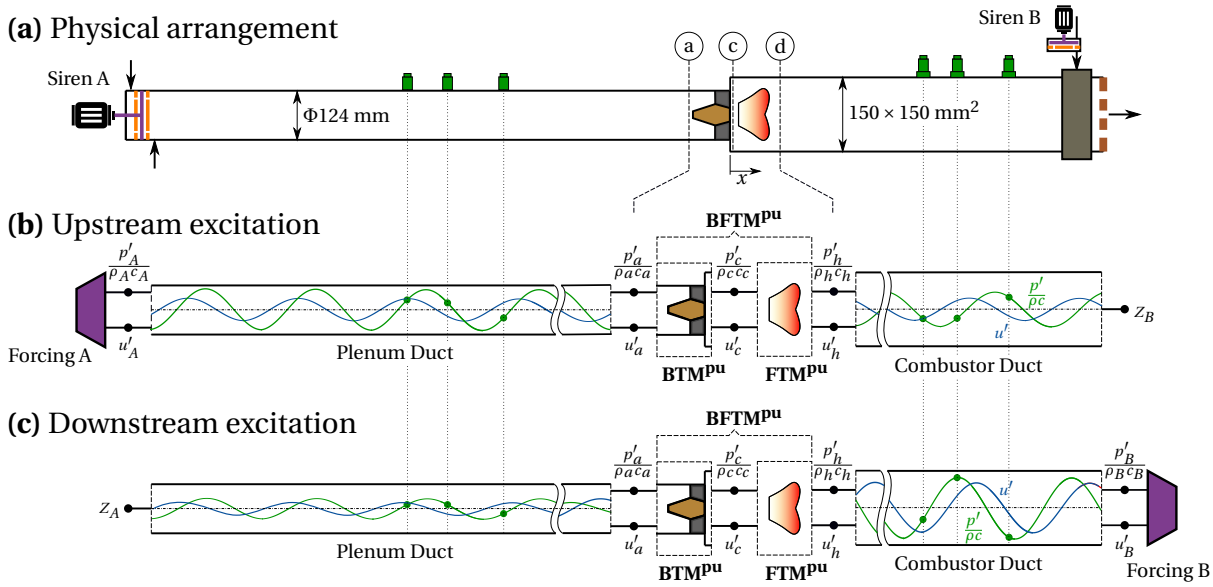

Figure 4.2: *Network model of the test rig, transfer matrices, and generation of waves under excitations*

In order to determine BTM using MMM (see Section 2.1.3), measurements using the six microphones were performed for each forcing in cold condition. The combined behaviour of

burner and flame is characterised through the composite Burner+Flame Transfer Matrix (BFTM). This composite TM was measured in the hot condition with flame. The FTM was then determined as:

$$\mathbf{FTM} = \mathbf{BFTM} \cdot \mathbf{BTM}^{-1} \tag{4.1}$$

This assumes that the combined acoustic characteristics of the burner and flame are superposition of the individual characteristics of the two elements as already shown in Figure 4.2. The output of BTM is equal to the input of FTM. Moreover, the BTM is assumed to remain unchanged even in the presence of flame [23]. Thus, the heat release fluctuation has no coupling with acoustic pressure.

The determination of temperatures used for evaluating ρ, c, k^+, k^- on either side of the acoustic element in cold and hot conditions are outlined in Section 4.3. The mean flow velocities required for calculating k^+, k^- were obtained using the air mass flow rate.

4.2 Determination of Flame Transfer Functions

Determination of transfer functions for premixed flames (Equation 2.38) requires evaluation of heat release fluctuation $\dot{Q}'$ and velocity perturbation u'. Several authors have directly measured $\dot{Q}'$ and u'_b [18, 103, 107]. However, it is possible to determine the FTF indirectly using microphone measurements. In the following subsections, an indirect method solely based on acoustical and a semi-direct method based on optical-acoustical measurements are explained.

4.2.1 Rankine-Hugoniot Relations based Indirect Method (RH)

The analytical FTM from Rankine-Hugoniot (RH) relations (Equation 2.48) is related to the FTF. Assuming this theoretical FTM describes the acoustic characteristics of the flame, its TM_{22}^{pu} element can be compared to the corresponding element FTM_{22}^{pu} of experimentally determined FTM (Equation 4.1) resulting in $\mathrm{FTF}_{\mathrm{RH}}$:

$$\mathrm{FTF}_{\mathrm{RH}} = \frac{\mathrm{FTM}_{22}^{pu} - 1}{T_r} = \frac{\mathrm{FTM}_{22}^{pu} - 1}{T_h / T_c - 1} \tag{4.2}$$

Here T_h is the local temperature just downstream of the flame (station h). Its evaluation is discussed in Section 4.3.

4.2.2 OH* Detection based Semi-Direct Method (OH)

An alternative method is to use photomultiplier measurements for determining the heat release fluctuation $\dot{Q}'$ as explained in Section 3.3.2. From Equation 2.38, determination of FTF

also requires the velocity perturbation at burner exit u'_b. This demands first evaluating the velocity perturbation just upstream of the flame (station "c" in Figure 4.2) using the BTM. From microphone measurements performed on the upstream side, the Riemann invariants can be calculated at burner inlet as mentioned in Section 2.1.3. The acoustic state upstream of the burner (p'_a, u'_a) can then be determined using Equations 2.15, 2.16. Assuming BTM remains the same in the hot condition, the acoustic state just upstream of the flame is then given by:

$$\begin{pmatrix} \frac{p'_c}{\rho_{us} c_{us}} \\ u'_c \end{pmatrix} = \mathbf{BTM^{pu}} \cdot \begin{pmatrix} \frac{p'_a}{\rho_{us} c_{us}} \\ u'_a \end{pmatrix} \tag{4.3}$$

The acoustic state at burner exit, station "b", is different from the acoustic state at flame upstream, station "c". This is because the BTM includes the area jump from burner exit area A_b to the downstream duct inlet area A_c as shown in Figure 4.3.

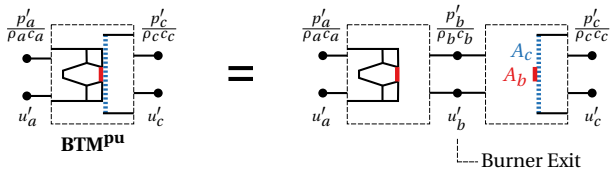

Figure 4.3: *Determination of velocity perturbation at burner exit*

Assuming the length of influence due to area change to be small[1], the velocity perturbation at burner exit u'_b can be obtained as [53, 54]:

$$u'_b = u'_c \frac{A_c}{A_b} \tag{4.4}$$

Finally, $\mathrm{FTF_{OH}}$ is determined using Equation 2.38.

4.3 Determination of Temperatures

The evaluation of transfer matrices and FTFs requires knowledge of temperatures at multiple locations in the test rig. Generally, these temperatures are very different under cold (subscript "C") condition without flame and hot (subscript "H") condition with flame. The assumptions made for simplification of the procedures and specific temperatures required for calculations are highlighted first. An improved method is then presented for empirical determination of the required temperatures from FTF results. Moreover, this method is compared with a previously used procedure for temperature estimation.

4.3.1 Simplification for Required Temperatures

For a 1D acoustic analysis, radially averaged temperatures are sufficient for wave reconstruction [108]. Hence, only axial variation in the flow temperature along the ducts was considered.

[1] This is equivalent to compactness. See description of compactness on p. 18.

Figure 4.4 qualitatively shows the axial temperature profiles in the test rig for the hot and cold conditions.

(a) Temperatures in cold condition

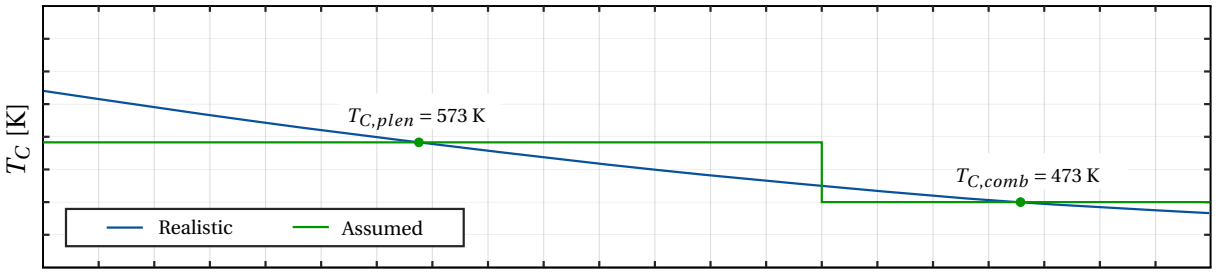

(b) Temperatures in hot condition

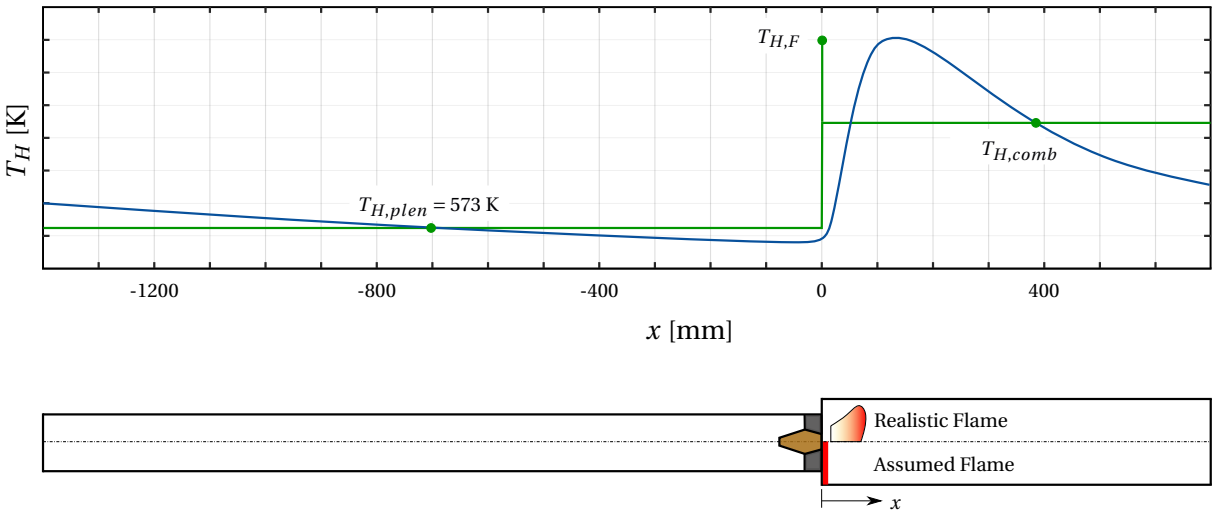

Figure 4.4: *Axial temperature profiles in the test rig with (hot condition) and without (cold condition) the flame*

As air flows downstream, it loses heat through the plenum and combustor walls to the ambient. Thus, the temperature decreases from plenum inlet up to the combustor outlet in cold condition as shown by the blue curve in Figure 4.4(a). However, in the presence of a flame (Figure 4.4(b)), the temperature decreases up to the burner exit and then increases sharply reaching the peak flame temperature. Afterwards, it gradually drops to the exhaust gas temperature at combustor exit. The realistic temperature profiles qualitatively depict the expected temperature variation in axial direction. Assuming a constant wall temperature, the flow temperature in the ducts approximately varies exponentially with the axial coordinate ($T(x) \propto e^{-x}$) [108], excluding the jump at the flame location. The speed of sound required in acoustic calculations is a strong function of temperature. However, Neunert investigated the influence of axial temperature profile for 1D acoustic calculations and concluded that an integral mean temperature is sufficient for wave reconstruction [86, 108]. Thus, plenum and combustor were

assumed to have a uniform speed of sound at axial mean temperatures $T_{C,plen}$ and $T_{C,comb}$ respectively in the cold condition. Similarly, only mean temperature in the plenum $T_{H,plen}$ and in the combustor $T_{H,comb}$ are required under hot condition.

These mean temperatures in the upstream and downstream ducts are sufficient for evaluation of transfer matrices using MMM. Whereas, determination of FTF_{OH} requires only the knowledge of $T_{H,plen}$. In Equation 4.3 for FTF_{OH}, measurements on the upstream side were evaluated at temperature $T_{us} = T_{H,plen}$. Instead of using $T_{ds} = T_{H,comb}$ on the downstream side, the acoustic state and mean flow velocity were evaluated using T_{us} since the station c lies on upstream side of the flame and is more close to the upstream duct conditions. However, application of Rankine-Hugoniot relations for determining FTF_{RH} additionally requires knowledge of the flame temperature $T_{H,F}$ (T_h in Equation 4.2.) For all the experiments in this study, the mean temperature in plenum was maintained at 573 K for both, cold and hot conditions. Based on the heat loss model of Bade [86], a temperature of 473 K is a good approximation for the mean combustor temperature $T_{C,comb}$ in cold condition and was assumed to remain fixed for all operating conditions. Finally, the mean combustor temperature in hot condition ($T_{H,comb}$) and the flame temperature ($T_{H,F}$) need to be known for each operating condition.

Since no direct measurement for these two temperatures was available, the temperatures were determined empirically from FTF_{RH} and FTF_{OH}.

4.3.2 Evaluation of Temperatures for Matching FTF_{RH} and FTF_{OH}

FTF_{RH} shows strong dependence upon the combustor and flame temperatures ($T_{H,comb}$ and $T_{H,F}$) as illustrated in Figure 4.5 for an exemplary case of 50kW-1.6L. At a fixed mean combustor temperature of $T_{H,comb}$ = 1380 K, the amplitude of FTF decreases proportionally for the whole frequency range with an increase in flame temperature $T_{H,comb}$. Whereas, an increase in mean combustor temperature at a constant flame temperature of 1715 K causes the amplitude of FTF_{RH} to increase at low and mid frequencies (4.5(b)). At high frequencies beyond 550 Hz, FTF amplitude shows negligible change. Moreover, high deviations were observed above 620 Hz. Hence, $T_{H,F}$ only shifts the $|FTF_{RH}|$ curve while $T_{H,comb}$ modifies its shape also. The phase of FTF_{RH} remains almost unchanged for both the temperatures.

The FTF evaluated using OH method (FTF_{OH}), is also shown by the black curves in Figure 4.5. FTF_{OH} is independent of temperatures $T_{H,comb}$ and $T_{H,F}$. In general, the trend and shape for FTF_{OH} is same as that for FTF_{RH}. The temperatures $T_{H,comb}$ and $T_{H,F}$ can be adjusted to match FTF_{RH} with FTF_{OH} as shown in Figure 4.6(a). However, FTF_{OH} shows deviation from FTF_{RH} at some low frequencies (<160 Hz), mid frequencies (400-500 Hz), and high frequencies (>580 Hz) data points as shown by the absolute difference (purple) curve in Figure 4.6(b). These deviations are associated with large differences in the velocity perturbation at burner exit $|u'_b|$ with frequency. For instance at very low frequencies, the amplitude of u'_b is very high leading to low FTF_{OH} amplitude. Converse is true at mid frequencies, the velocity u'_b become very low leading to overshoot in FTF_{OH} amplitude. Finally, both acoustic and optical meas-

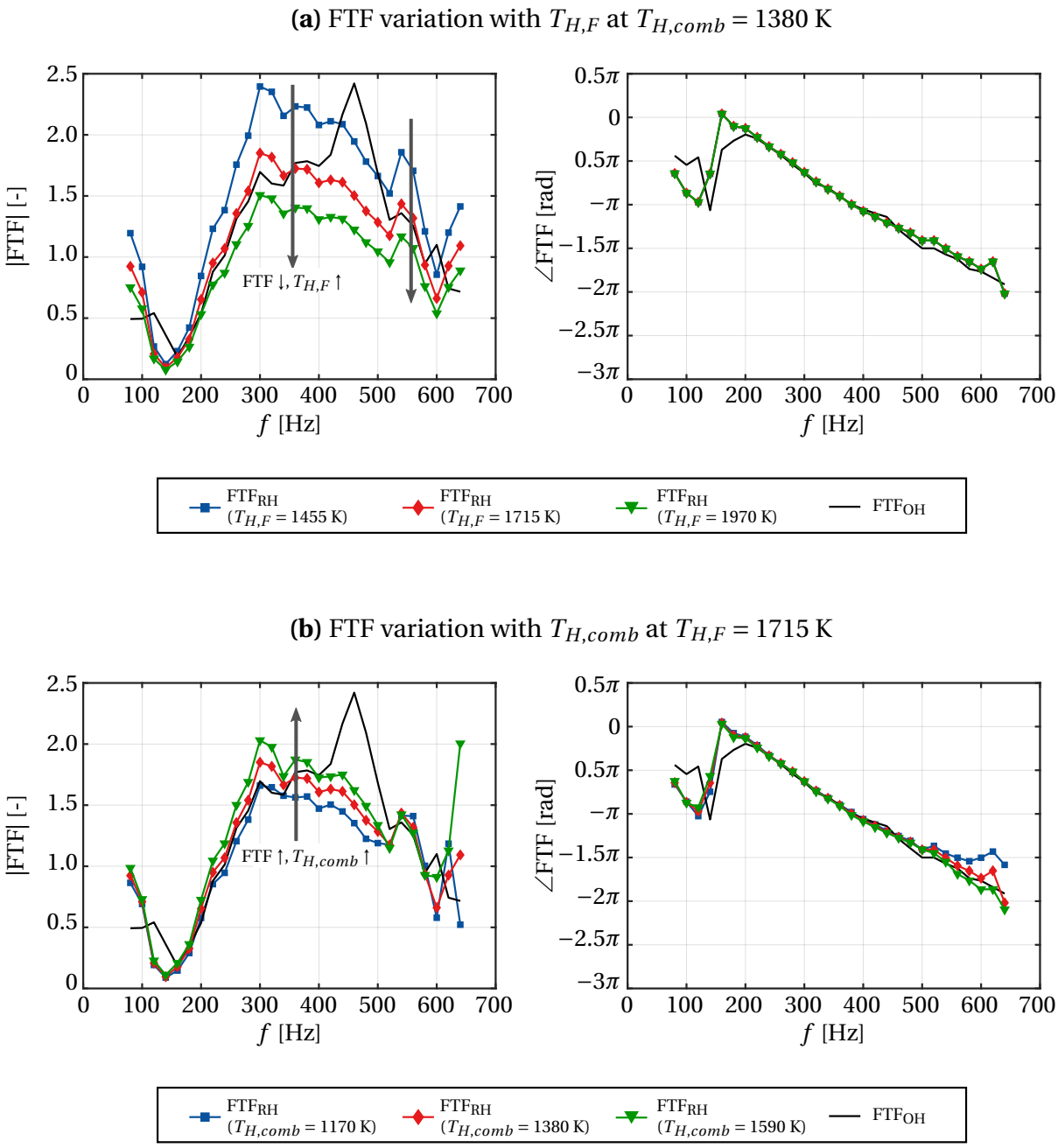

Figure 4.5: *Dependence of FTF_{RH} on mean combustor ($T_{H,comb}$) as well as flame temperatures ($T_{H,F}$) and comparison to FTF_{OH}; exemplary case 50kW-1.6L*

urement data show scatter at high frequencies (>580 Hz) and therefore the two cannot match in this range.

An automatic method was used for identifying the data points to be ignored, hereafter termed *outliers*, when matching FTF_{RH} with FTF_{OH}. In this technique, first the temperatures $T_{H,comb}$ and $T_{H,F}$ are adjusted manually for approximately matching FTF_{RH} with FTF_{OH}. This gives an initial prediction of the two temperatures. Then absolute difference (purple curve) is evalu-

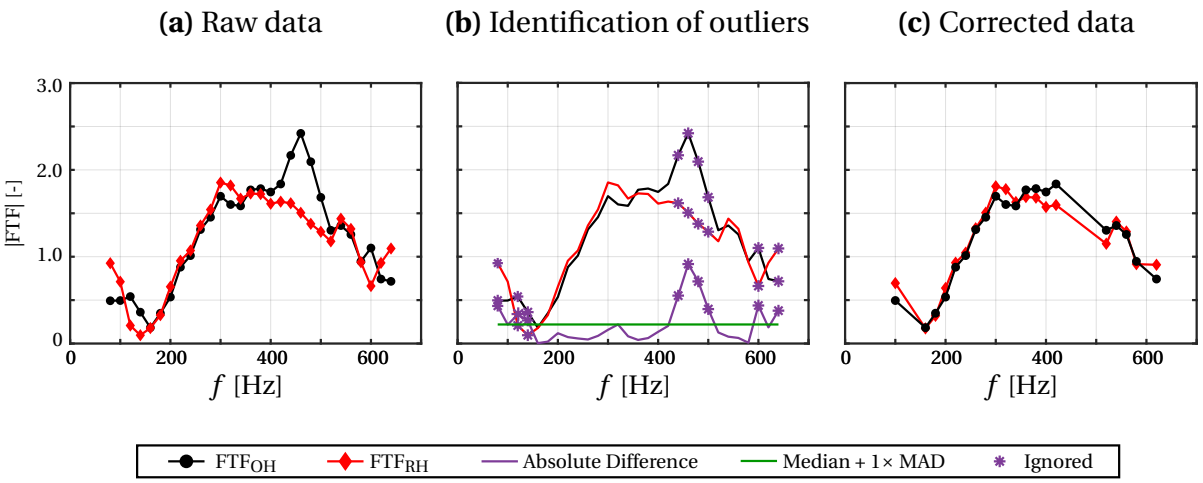

Figure 4.6: *Identification and removal of outliers for matching FTF_{RH} with FTF_{OH}; exemplary case for operating point 50kW-1.6L*

ated between FTF_{RH} and FTF_{OH} at the predicted temperatures. Points deviating by more than one MAD[2] from the median of absolute difference are automatically detected as outliers. This threshold is represented by the green horizontal line in Figure 4.6(b), outliers are denoted by purple asterisk markers. After removal of outliers, corrected data (Figure 4.6(c)) is then used to determine the optimum temperatures. This was done by minimising the Root Mean Square Error (RMSE) between the amplitudes of FTF_{RH} and FTF_{OH}:

$$\mathrm{RMSE}_{|\mathrm{FTF}|} = \sqrt{\frac{1}{n}\sum_{j=1}^{n}\left(|\mathrm{FTF}_{\mathrm{RH}}(\omega_j)| - |\mathrm{FTF}_{\mathrm{OH}}(\omega_j)|\right)^2} \tag{4.5}$$

The RMSE was evaluated for selected combinations of $T_{H,comb}$ and $T_{H,F}$, shown as a surface in Figure 4.7(a). The bell-shaped surface validates that $|FTF_{RH}|$ varies differently with $T_{H,comb}$ and $T_{H,F}$. Therefore, an optimum value of both the temperatures exist corresponding to minimum RMSE point (in this case 0.11). The temperatures at this point were taken as empirically determined mean combustor and flame temperatures.

It is interesting to note that a 15% change in $T_{H,comb}$ causes the FTF magnitude to change on average by 10% only. Whereas, a 15% change in $T_{H,F}$ causes an average change of 25% in FTF magnitude. Thus, FTF_{RH} is more sensitive to $T_{H,F}$ than $T_{H,comb}$ and therefore the former temperature is more deterministic.

Since FTF_{RH} is a weaker function of $T_{H,comb}$, Bade proposed to assume a fixed $T_{H,comb}$ for all the operating conditions [86] and only calculating $T_{H,F}$. However, estimating $T_{H,comb}$ by the above described method is more accurate as shown in Figure 4.7. Assuming a fixed $T_{H,comb}$ = 1270 K and optimising only $T_{H,F}$ would result in a minimum RMSE = 0.13 between the two curves (see Figure 4.7(b)). However, optimising both $T_{H,comb}$ and $T_{H,F}$ reduces this error to

[2]Median Absolute Deviation (MAD) is the average of absolute difference from the median. Using this metric for identification of outliers is more robust than other metrics like mean and standard deviations [109].

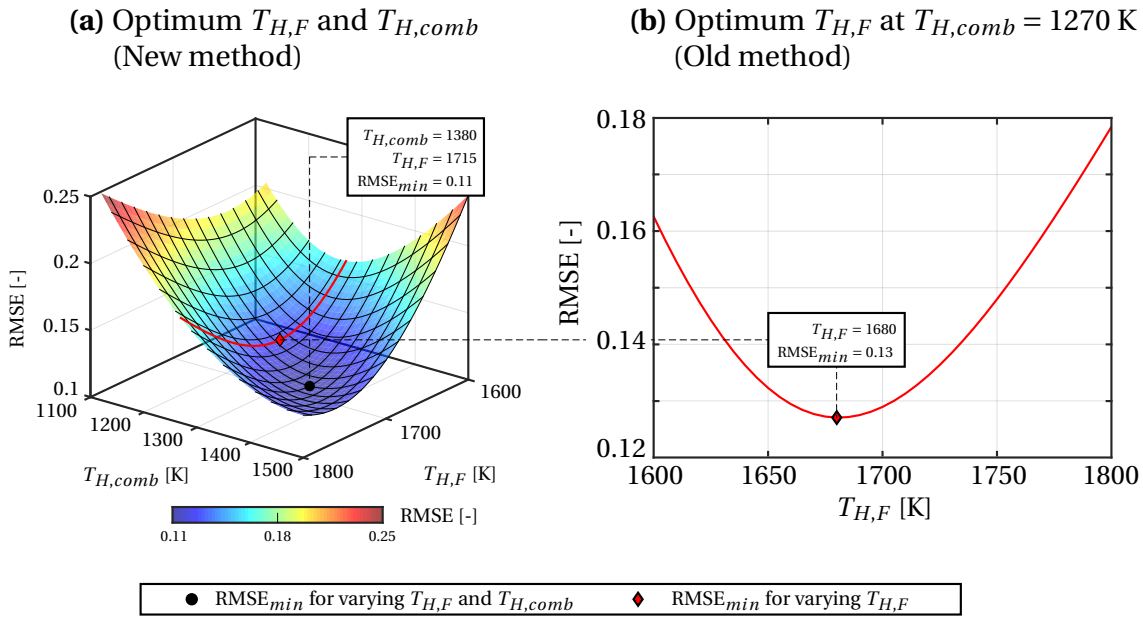

Figure 4.7: *RMSE between FTF_{RH} and FTF_{OH} as a function of temperatures and comparison of new and old estimation methods; exemplary case for operating point 50kW-1.6L*

0.11 which is a significant change considering that the RMSE corresponds to the absolute difference of the two amplitudes and not their actual values.

Resulting temperatures for different operating conditions are discussed in Section 5.2.

4.4 Processing of Stationary Flame Images

The flame images acquired as explained in 3.3.2 were evaluated to estimate the geometric features of the flame relevant to flame dynamics. For this purpose, a series of operations were performed on stationary images corresponding to each operating point as outlined in Figure 4.8.

The ensemble of 1000 images (step 1) was averaged to reduce stochastic noise and determines a temporal mean intensity distribution $I(x,y)$. Intensity of resulting image was scaled from 0 to 1 through division by the maximum value (2). This allows a qualitative comparison of flame images for different operating conditions disregarding the absolute intensity level. For removal of skew in the images, a calibration target set vertically along the combustor central plane with its axis aligning with the combustor axis was imaged. Using MATLAB *Image Processing Toolbox*, manually selected control points were then used to obtain a transformation matrix between the captured (3a) and reference (3b) images of the target (see Figure 4.8). This transformation was then applied to the flame images for eliminating any potential skew. The flame is assumed to be axisymmetric with respect to the combustor axis. Therefore, the flame central axis coincides with the centreline of the de-skewed image (4).

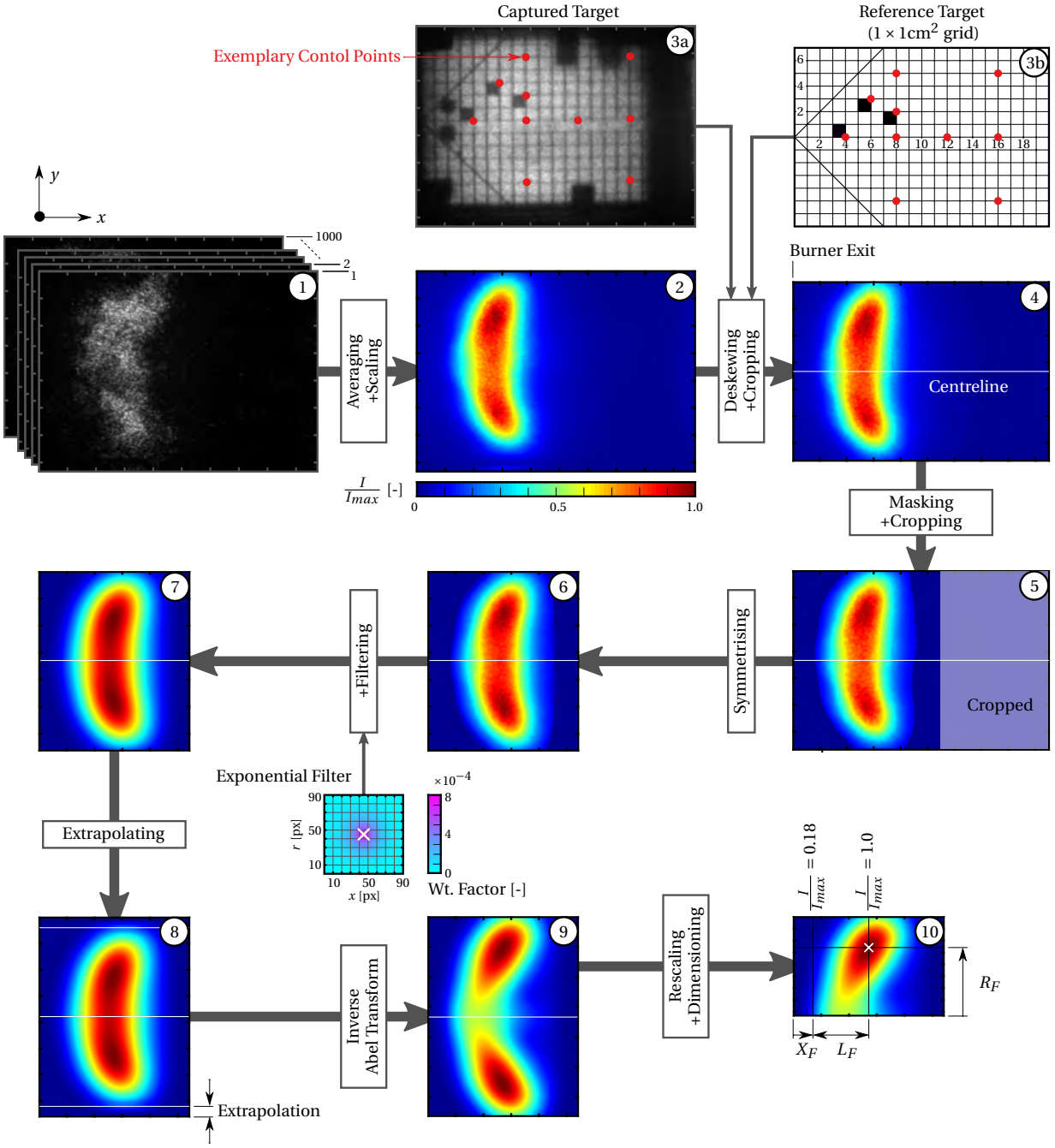

Figure 4.8: *Processing of stationary flame images for estimating the geometric features relevant to FTFs*

A mask was then applied by setting relative intensities to zero for all pixels having values less than 0.1 (step 5 in Figure 4.8):

$$\frac{I}{I_{max}}\left(\frac{I}{I_{max}} < 0.1\right) = 0 \tag{4.6}$$

This helps in avoiding the spurious pixels in further calculations. Moreover, extra region of

image containing no information was cropped (5). Symmetrising was then done to make the two halves identical by flipping the image horizontally and taking the mean of original and flipped image (6). Afterwards, an exponential filter with a window size of 90×90 px^2 was applied for smoothing the intensity distribution (7), weighting factors shown in cyan-magneta colour map[3]. For a better deconvolution of LOS images, linear extrapolation was performed (8). The extrapolation was done until the first (and last) row had zero intensity estimation. Subsequently, Inverse Abel Transform (9) was applied for estimating the intensities along the central plane using Fourier method with five terms [110]. Finally, the relative intensities were rescaled to make them within the range of 0 to 1 and key dimensions were determined in px (10). The lift-off distance X_F representing the distance between burner exit and flame anchoring position was calculated as the distance from left edge to the column having $I/I_{max} = 0.18$. This value was used since it is known for good reproducibility [86].

$$X_F = x_j \left(\frac{I}{I_{max}} = 0.18 \right) \tag{4.7}$$

The axial distance from flame anchoring position to the point of maximum intensity was taken as flame length L_F and radial distance from centreline to the maximum intensity point was taken as flame radius R_F:

$$L_F = x_j \left(\frac{I}{I_{max}} = 1.0 \right) - x_j \left(\frac{I}{I_{max}} = 0.18 \right) \tag{4.8}$$

$$R_F = y_i \left(\frac{I}{I_{max}} = 1.0 \right) - y_{centre} \tag{4.9}$$

These geometric parameters were used to explain the change in flame dynamics with operating conditions in Chapter 5. They were determined in "px" and were converted to "mm" using image scale factor.

4.5 Methodology for Proper Orthogonal Decomposition

Reduced order modelling of FTFs was done using Proper Orthogonal Decomposition (POD) in the context of its variation with operating parameters (thermal power and air ratio.) The mathematical treatment outlined in Section 2.3 was employed to develop a ROM of FTFs obtained. A select FTF data FTF $= \nu(w, \psi)$ distributed in 1D frequency space $w = f$ and changing with operating conditions in parametric space $\psi = OP$ was used. Since FTF is a set of complex numbers, two ensembles corresponding to its amplitude $\mathbf{V} = |\text{FTF}|$ and phase $\mathbf{V} = \angle\text{FTF}$ were constructed and POD algorithm was applied separately. For two operating parameters, the data with both varying thermal power and air ratio was arranged row-wise in $\mathbf{V}$. This has no affect on the results as long as the corresponding POD coefficients are considered in the same order. That is, rows of coefficient matrix correspond to the data arrangement in $\mathbf{V}$. Indeed, the coefficients were visualised in a 2D parametric space.

[3]Filtering is a linear transformation operation in which the central pixel intensity value is considered unknown and is determined as weighted sum of nearby pixels.

In the first step, an exemplary data ensemble was considered for performing POD as described in Section 2.3. The mathematical meaning of the POD modes and coefficients for FTFs can be found in Appendix A.The modes with significant variance content were identified using MRI. Selected modes were then used for reconstruction of FTF at a desired operating point using Equation 2.57. This was then validated against experimentally determined FTF at the same operating point using RMSE:

$$\mathrm{RMSE}_{\mathrm{POD}} = \sqrt{\frac{1}{n}\sum_{i=1}^{n}\left(\mathrm{FTF}^{\mathrm{POD}}(\omega_i) - \mathrm{FTF}^{Exp}(\omega_i)\right)^2} \tag{4.10}$$

The above equation is used to calculate both, RMSE for amplitude and phase. Subsequently, different data ensembles with respect to number of measurements and arrangement in parametric space were analysed in a similar way. Reconstructions from different ensembles were compared using RMSE.

Ideally, the modes should be independent of the data ensemble and should capture the correlation in the data. In other words, any two similar data ensembles of a given problem should yield same modes. This was assessed by performing POD on different ensembles of data and evaluating the Mode Sensitivty Index (MSI). For j-th mode, it can be calculated as [47, 111]:

$$\mathrm{MSI}_j = \sqrt{\theta_{j,en1} \cdot \theta_{j,en2}} \tag{4.11}$$

Where subscript en denotes the ensemble used. If the mode is not biased by the data at all, MSI should be unity. A lower value of this metric indicates a higher deviation in modes determined from the two ensembles.

5 Results for Flame Response

This chapter presents and discusses the results found in the current study. The Transfer Matrix obtained for the burner and its sensitivity to operating parameters are furnished in the first section. Section 5.2 highlights the empirically determined temperatures for evaluating FTFs through the Rankine-Hugoniot method. Generic features of FTFs, their quality assessment, and their sensitivity to operating conditions are elaborated in Section 5.3. Subsequently, geometric parameters of the flames for different operating conditions evaluated through stationary flame images are explained. These parameters are then used to explain the sensitivity of FTFs to operating conditions in the closing section.

5.1 Burner Transfer Matrices (BTMs)

Burner transfer matrices are a function of the burner's geometry, internal flow pattern, and viscous losses. In general, they may also depend upon the operating conditions such as flow-rate. Therefore, the transfer matrices for the swirl burner were determined for all OPs using MMM as described in Section 2.1.3. Measurements were performed under cold condition with a preheating temperature of 573 K, only air flow-rate was varied according to the operating conditions (see Section 3.4).

The amplitudes and phases of the four elements of BTMs corresponding to varying thermal power and air ratio are shown in Figure 5.1 and Figure 5.2 respectively. The plots of BTMs are segregated with respect to thermal power and air ratio only for convenience, both the figures show BTMs for varying air flow-rates.

The results show that the flow-rate has almost no impact on the amplitudes except for the element $\mathbf{BTM_{12}}$ for which the amplitude slightly increases with flow, particularly at low frequencies. The phases of all the elements are almost unchanged excluding the phase jumps for element $\mathbf{BTM_{21}}$ corresponding to zero amplitudes near 100 Hz. These observations are inline with the experimental findings of Bade [86] for a similar burner and network modelling of Bade and Alemela [31, 86]. The model has shown that element $\mathbf{BTM_{12}}$ is a function of Mach number as well as flow losses and therefore depends upon flow-rate. A common trend of the amplitudes suggests an increase with frequency for all the elements except for $\mathbf{BTM_{22}}$ which roughly remains the same. This element was considered a function of the burner outlet-to-inlet area ratio in the network model of Bade which remains fixed for a given burner. Amplitudes of elements $\mathbf{BTM_{11}}$ and $\mathbf{BTM_{12}}$ are in general higher than the other elements. The

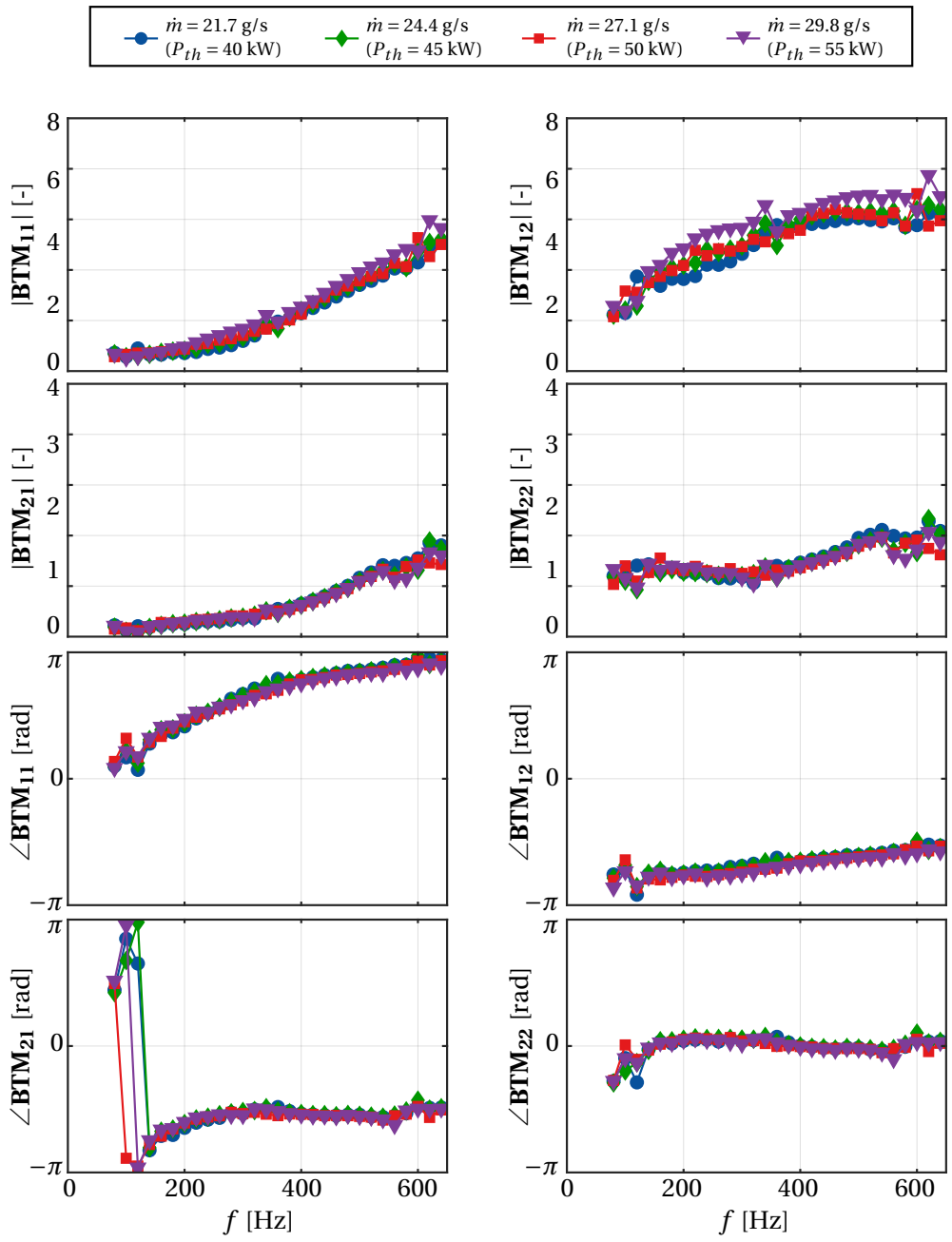

Figure 5.1: *Burner Transfer Matrices corresponding to varying thermal power at* $\lambda = 1.6$

increase in amplitudes of the three elements suggests that with increasing frequency, downstream acoustic pressure and velocity generally become stronger functions of the upstream acoustic pressure and velocity. This is true except for the fact that the relation of downstream velocity perturbation u'_c to upstream velocity perturbation u'_a remains almost unchanged (see Figure 5.1). The phases of all the elements remain nearly unaltered with frequency except for element $\mathbf{BTM_{11}}$, for which it increases. This represents a pressure fluctuation transmission

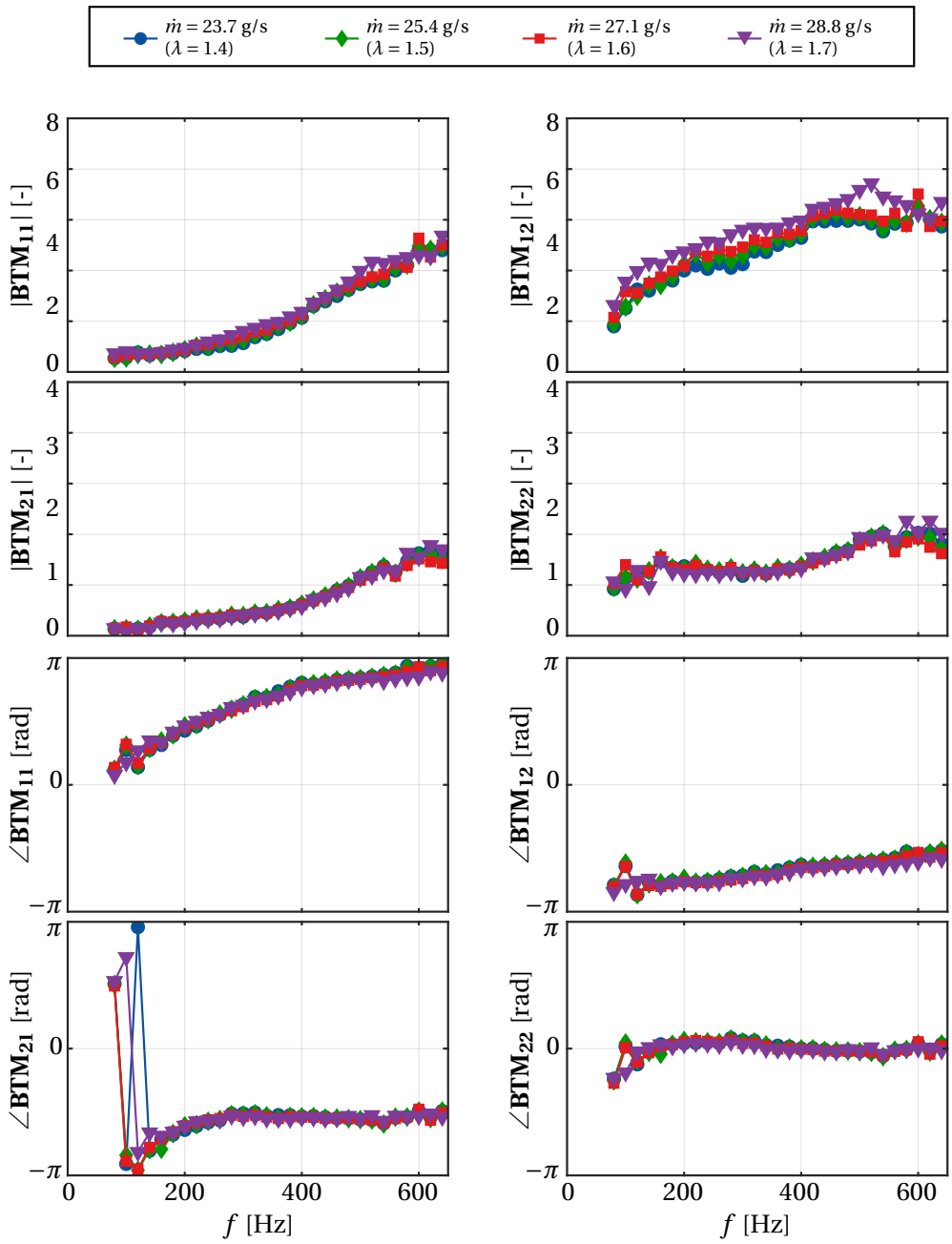

Figure 5.2: *Burner Transfer Matrices corresponding to varying air ratio at* $P_{th} = 50$ *kW*

delay across the burner. Similar behaviour of BTMs with respect to frequency and operating parameters is reported in [86].

5.2 Temperatures for Matching FTF_{RH} and FTF_{OH}

The procedure outlined in Section 4.3 was used for all the operating cases to obtain mean combustor ($T_{H,comb}$) and the flame temperatures ($T_{H,F}$) by matching FTF_{RH} to FTF_{OH}. For a given Operating Point (OP), 3-4 different measurements of FTFs were used to determine multiple temperature values. The final empirical temperatures were taken as the resulting mean. Variation of these temperatures with respect to thermal power and air ratio is depicted in Figure 5.3(a) using a plane surface fit to the empirical temperatures denoted by markers. The figure also shows theoretical limit of adiabatic flame temperature obtained through an in-house script with a reactants temperature of 573 K. This limiting temperature is a strong function of air ratio and decreases linearly with increasing λ (see Figure 1.2). Both the mean combustor and flame temperatures remain well within this limit.

(a) Temperatures determined and fitted surfaces for varying P_{th} and λ

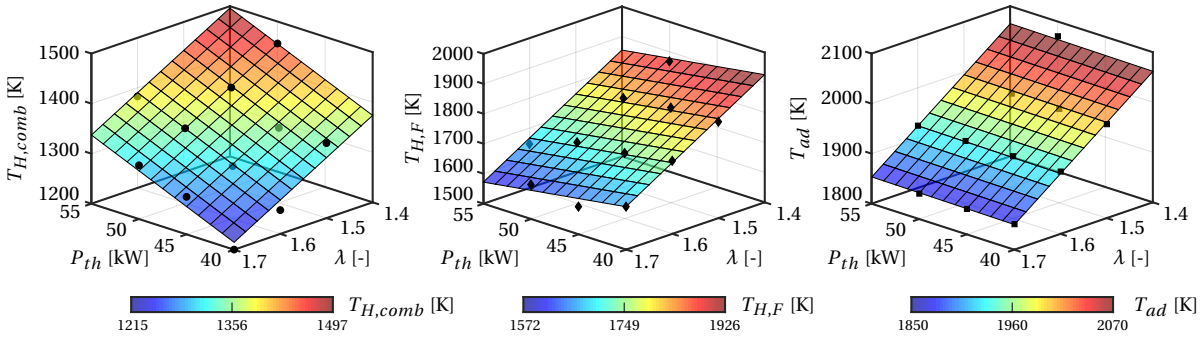

(b) Varying P_{th} at $\lambda = 1.6$

(c) Varying λ at $P_{th} = 50$ kW

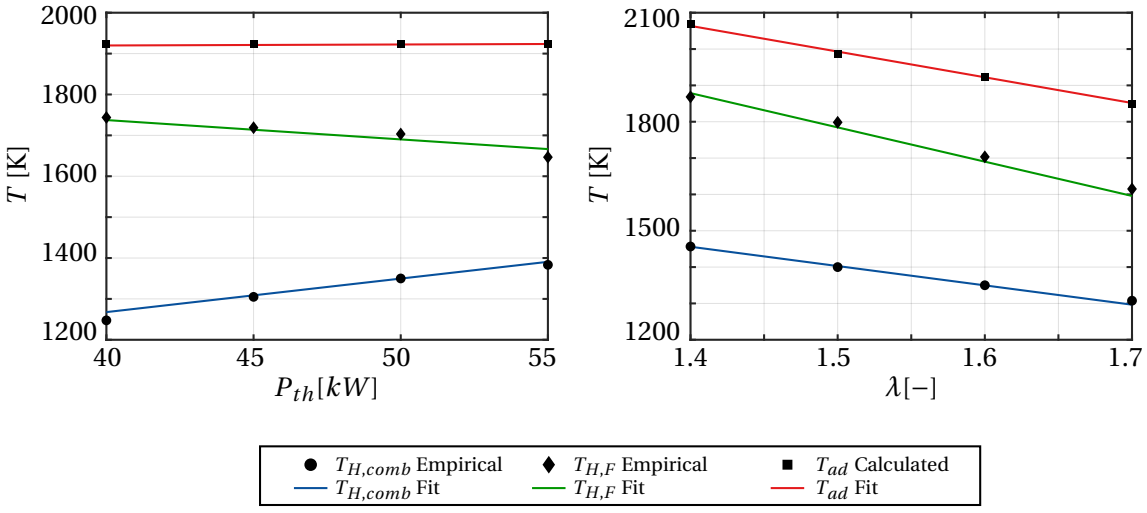

Figure 5.3: *Variation of empirically determined mean combustor and flame temperatures with thermal power and air ratio*

Figure 5.3(b) also shows the temperature curves for varying thermal power at $\lambda = 1.6$ and varying air ratio at $P_{th} = 50$ kW. The lines are obtained from the fitted surfaces data. The flame temperature is mainly governed by the chemistry of combustion reactions while the combustor temperature is associated with the net enthalpy input. Both temperatures also depend upon the heat loss from the combustor control volume. An increase in thermal power at fixed λ does not change the chemical conditions and therefore the flame temperature would remain the same. However, the heat loss from the combustor increases due to increased flow velocity and larger flame radiating area. This results in a slight decrease of the flame temperature. The mean combustor temperature shows an increase with thermal power. Although convective heat loss from combustor walls also increases with thermal power, the increase in net heat input to the combustor dominate. An increase in air ratio makes the burning mixture leaner and thus reduces the flame temperature as well as the net heat input to the combustor. Thus, the mean combustor temperature also decreases. All the temperature trends approximate a linear variation with operating parameters. These trends are in-line with the temperatures predicted by Bade's temperature model [86].

The temperatures resulting from the plane surface fit were used for evaluating the final $\mathrm{FTF_{RH}}$ plots.

5.3 Flame Transfer Functions (FTFs)

The results obtained for FTFs and a quality assessment of the used procedures are discussed in the following subsections. As already mentioned in Section 4.3.2, both $\mathrm{FTF_{RH}}$ and $\mathrm{FTF_{OH}}$ generally show the same trends and are matched by using appropriate temperatures (see Figure 4.5). Therefore, only the results for $\mathrm{FTF_{RH}}$ are presented hereafter.

5.3.1 General Trend and Features

All the FTFs irrespective of the operating condition display some common features depicted in Figure 5.4. Amplitude and phase for an exemplary case of 45kW-1.6L are shown. At very low frequencies, quasi-steady flame behaviour signifying |FTF| = 1 with a zero phase angle (see Section 2.2.3) is expected. This is also suggested by the FTF amplitude and phase trends below 150 Hz. As the frequency increases, the amplitude decreases reaching to the first minimum $\mathrm{FTF}_{min,1}$ near 150 Hz. This is very close to zero amplitude indicating that flame became insensitive to velocity perturbations. It causes a corresponding jump in the phase at the same frequency. The amplitude then increases to reach the peak amplitude FTF_{max} near 320 Hz. Afterwards, the amplitude decreases with frequency reaching to a second minimum $\mathrm{FTF}_{min,2}$. Note that the frequencies mentioned for characteristic points in FTF trend are only indicative and generally vary with the operating conditions.

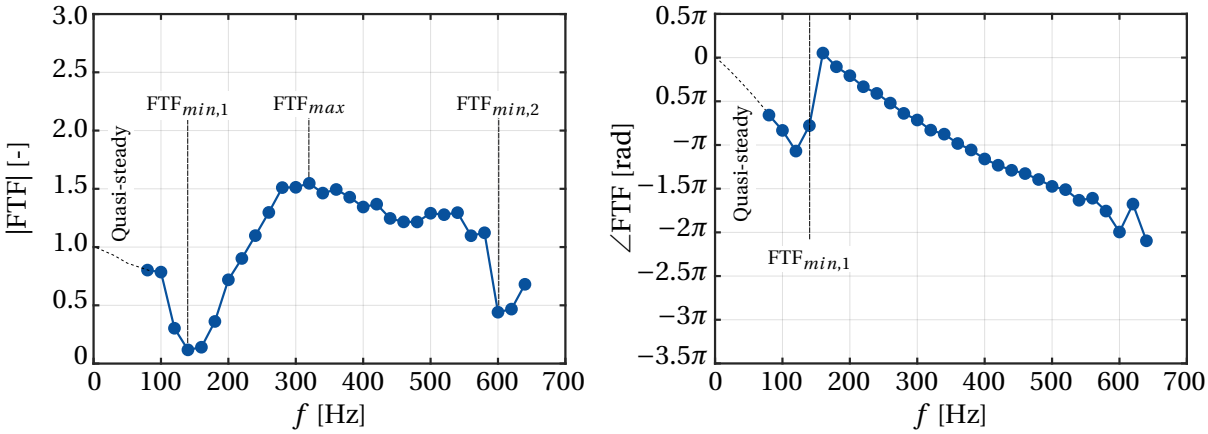

Figure 5.4: *General features of FTF frequency trend; exemplary case 45kW-1.6L*

The phase of FTF signifies the time delay τ after which the flame responds to a velocity perturbation. For sinusoidal perturbations the delay and phase are related as [16, 18]:

$$\angle \mathrm{FTF}(\omega) = \omega\tau \tag{5.1}$$

In Figure 5.4, the phase of FTF decreases with increasing frequency in a linear fashion. This is characteristic of a constant time delay between the acoustic velocity perturbation at burner exit u'_b and heat release fluctuation at the flame $\dot{Q}'$. Hence, the physical mechanisms which entail convective time delay (such as swirl number fluctuations, see Section 2.2.2) dominate the FTF behaviour. Moreover, the increase and decrease in FTF amplitude with increasing frequency is a result of constructive and destructive interaction of different mechanisms [69, 73, 88]. The identification of exact mechanisms involved is beyond the scope of current study.

5.3.2 Quality Assessment

The quality of FTF results was assessed in terms of reproducibility for a given OP, comparison to old measurements, and influence of microphone location.

In order to check reliability of the results, the measurements for exemplary operating points were done multiple times on the same day (different versions) and on different days. Figure 5.5(a) shows the reproducibility of FTFs for an exemplary case of 50kW-1.7L. The error in reproducibility of FTFs is depicted in Figure 5.5(b).

(a) Reproducibility of FTFs

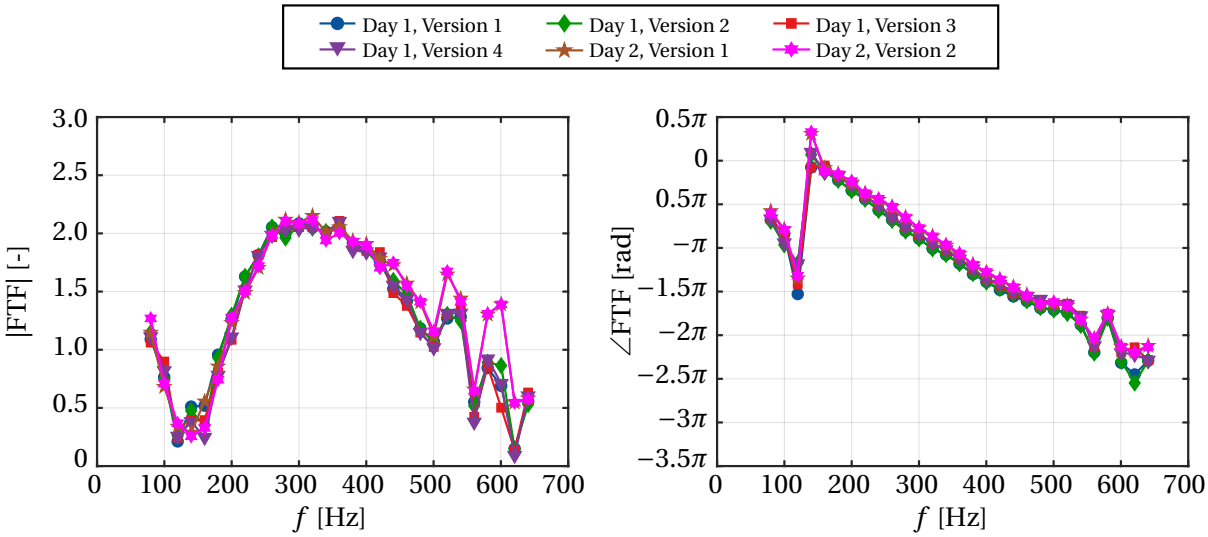

(b) Error in reproducibility of FTFs

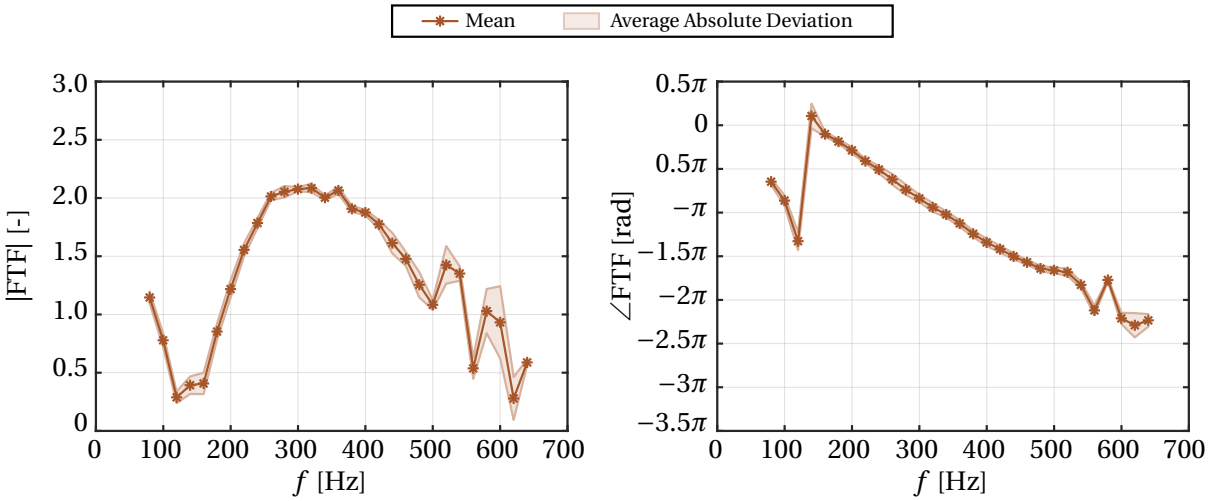

Figure 5.5: *Reproducibility of FTF results; exemplary case 50kW-1.7L*

The centreline marked by "*" represents the mean of the data set FTF_{mean} and the shaded region denotes the Average Absolute Deviation (AAD) from the mean:

$$\mathrm{FTF}_{mean}(\omega) = \frac{1}{n}\sum_{j=1}^{n} \mathrm{FTF}_j(\omega) \tag{5.2}$$

$$\mathrm{AAD}_{\mathrm{FTF}}(\omega) = \frac{1}{n}\sum_{j=1}^{n} \left|\mathrm{FTF}_j(\omega) - \mathrm{FTF}_{mean}(\omega)\right| \tag{5.3}$$

Where $n = 6$ are the number of measurements. The deviations for both amplitude and phase are small except for high frequencies above 560 Hz. The amplitude has a maximum AAD of

0.31 at 600 Hz and phase has a maximum deviation of 0.44 at 620 Hz. On average, for the entire frequency range, the deviation for amplitude remains below 0.1 and that for phase is below 0.24. This demonstrates a very good reproducibility for determination of FTFs.

For the same swirl burner, the FTFs were previously determined by Bade for perfectly premixed natural gas flames [86]. However, changes have been made to the test rig over the years and the current test configuration is different from the one used before. The newly obtained results were compared to previous measurements in order to evaluate the reliability of procedures and test setup. In general, the newly determined FTFs showed same trends as reported previously. The comparison for an exemplary operating point of 50kW-1.5L is shown in Figure 5.6.

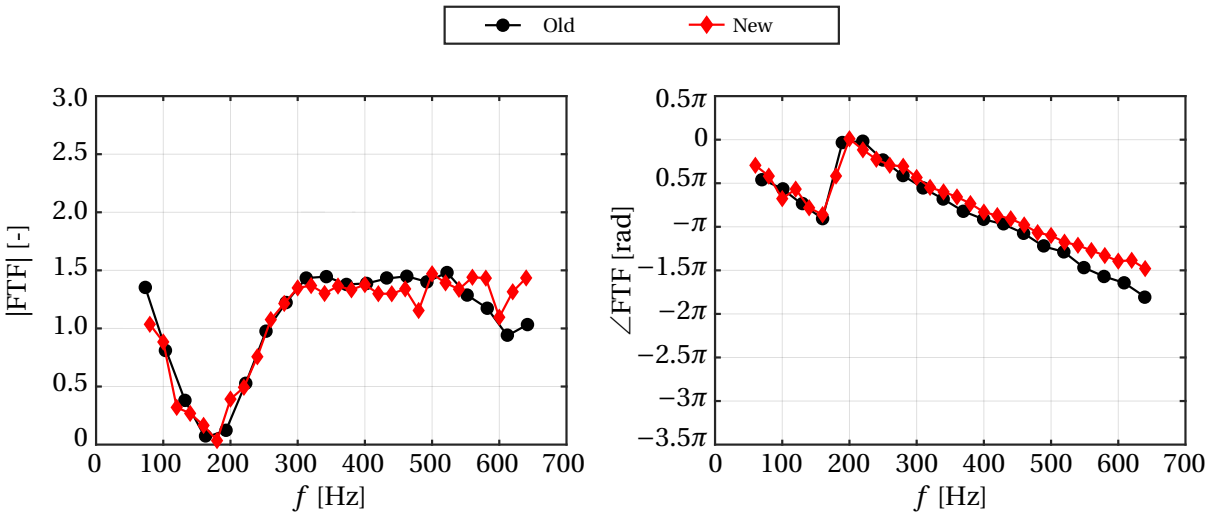

Figure 5.6: *Comparison of newly determined FTFs with old measurements (Bade [86]); exemplary case 50kW-1.5L*

The amplitude curves show a very good agreement except for the scatter beyond 600 Hz. The phase trend also show good agreement excluding a slightly lower slope of the new phase curve at high frequencies. The new results generally agree well with the previous measurements.

It has been reported in previous studies that the results of MMM are sensitive to location of microphones [61, 103]. Particularly at low frequencies, sufficient spacing between the microphones is desired for good quality reconstruction of acoustic fields [31]. In order to test the effect of microphones location on the FTFs obtained using RH method, the position of one microphone (M1, see Figure 3.3) was changed from $x = -655$ mm to $x = -595$ mm. Two tests were performed for the corresponding microphone locations under the same operating conditions. The $\mathrm{FTF_{RH}}$ results obtained for the two configurations are shown in Figure 5.7.

It is evident from the figure that both the amplitude and phase of FTF are approximately the same, especially at low frequencies. Therefore, the results obtained from MMM can be considered free from any significant error associated with microphone spacing.

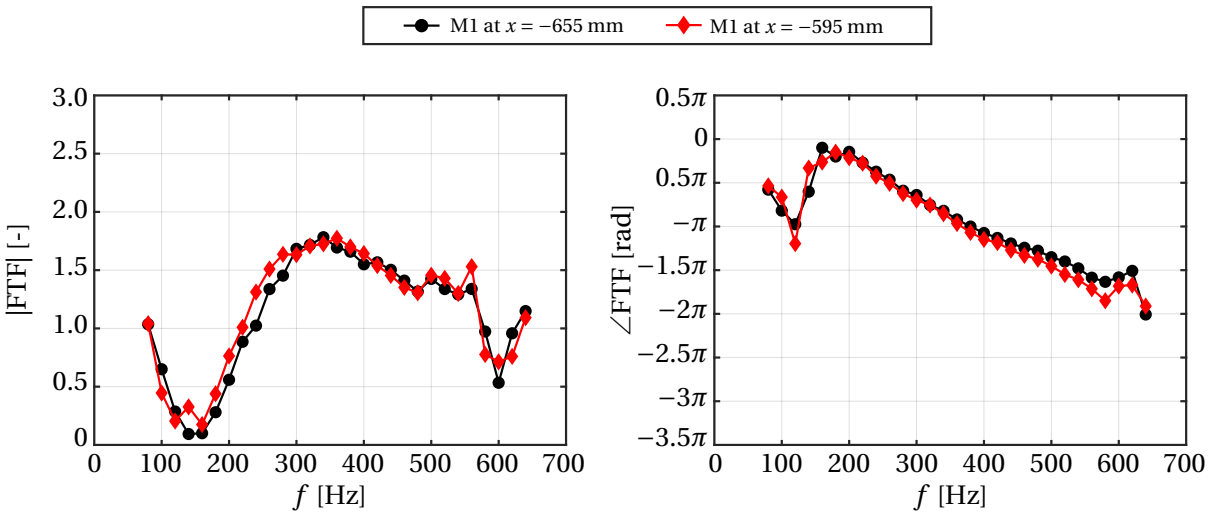

Figure 5.7: *Influence of microphone location (M1) on FTF determined using RH method; exemplary case 50kW-1.6L*

Hence, adequate quality of the FTF results is achieved.

5.3.3 Sensitivity to Operating Conditions

The flame response, and hence FTFs, depend upon the operating conditions, namely thermal power and air ratio. The amplitudes and phases of the FTFs for varying thermal power at a fixed air ratio of 1.6 are shown in Figure 5.8.

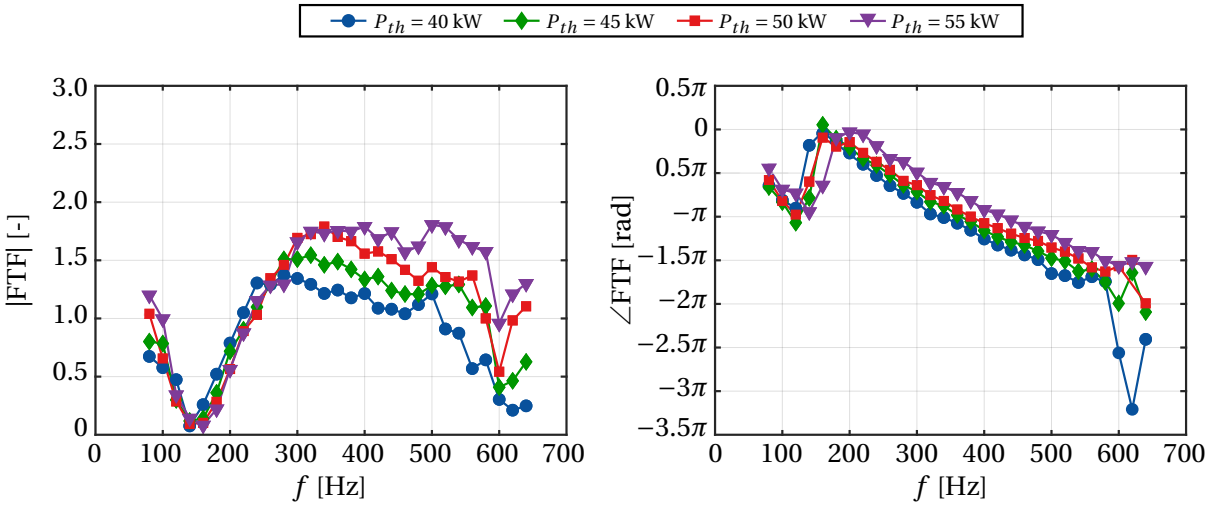

Figure 5.8: *Flame Transfer Functions for varying thermal power at* $\lambda = 1.6$

All the curves show the generic features mentioned in Section 5.3.1. The amplitudes increase throughout the frequency range with increasing thermal power. The frequency for first min-

imum ($FTF_{min,1}$) slightly increases with increasing thermal power. This is also evident from the rightward shifting phase jump. The phase curves show a slight increase with thermal power, which is pronounced due to this jump for mid-high frequencies. Moreover, the frequency corresponding to peak amplitude (FTF_{max}) increases with thermal power while the second minimum in FTF amplitudes (point $FTF_{min,2}$) occur approximately at 600 Hz for all the operating points.

Figure 5.9 shows the amplitudes and phases of FTFs for varying air ratio at a fixed thermal power of 50 kW. The amplitudes increase with increasing air ratio up to a critical frequency f_{cr}, beyond which they decrease. The frequency for $FTF_{min,1}$ decreases with increasing air ratio in contrast to its increase with increasing thermal power. This leads to a corresponding jump in the phase curves. The phase curves shift vertically downward with increasing air ratio. As opposed to varying thermal power, the slope of the phase curves increases with increasing air ratio. Furthermore, the frequency for FTF_{max} decrease with increasing air ratio. Due to different behaviour beyond f_{cr}, some amplitude curves show a second minimum near 600 Hz while others do not show second minimum in the measured frequency range. In both the Figures 5.8 and 5.9, scatter can be seen in the measured data beyond 580 Hz.

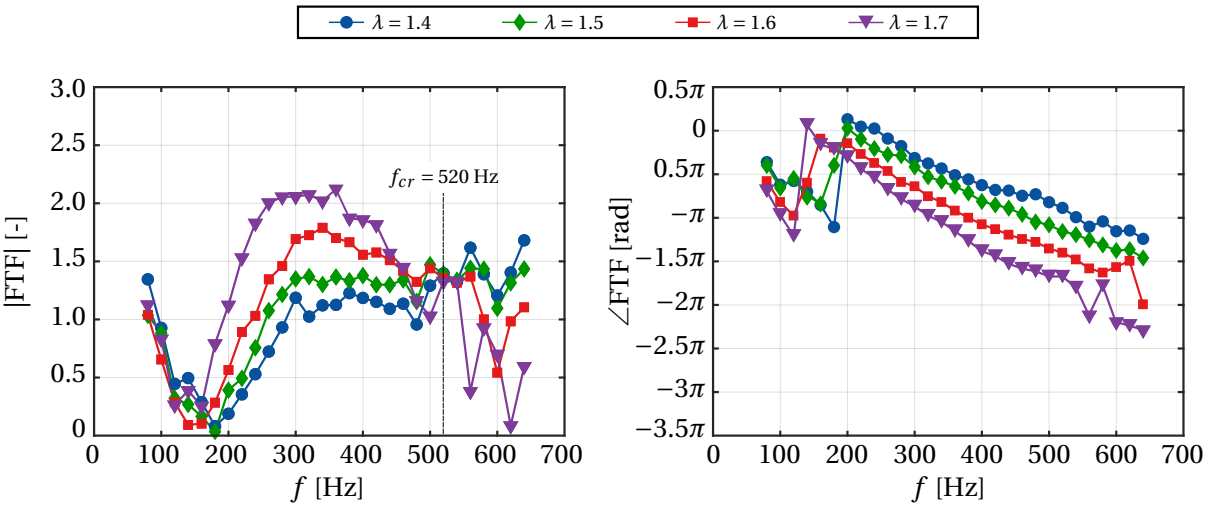

Figure 5.9: *Flame Transfer Functions for varying air ratio at P_{th} = 50 kW*

Similar trends of FTFs for varying thermal power and air ratio have been previously reported [86].

The influence of thermal power on the critical frequency beyond which FTF amplitude decreases with increasing air ratio was evaluated as shown in Figure 5.10. This frequency increases with increasing thermal power.

The explanation of these variations in FTF require an understanding of variation in flame geometry with thermal power and air ratio. It is discussed in the next section.

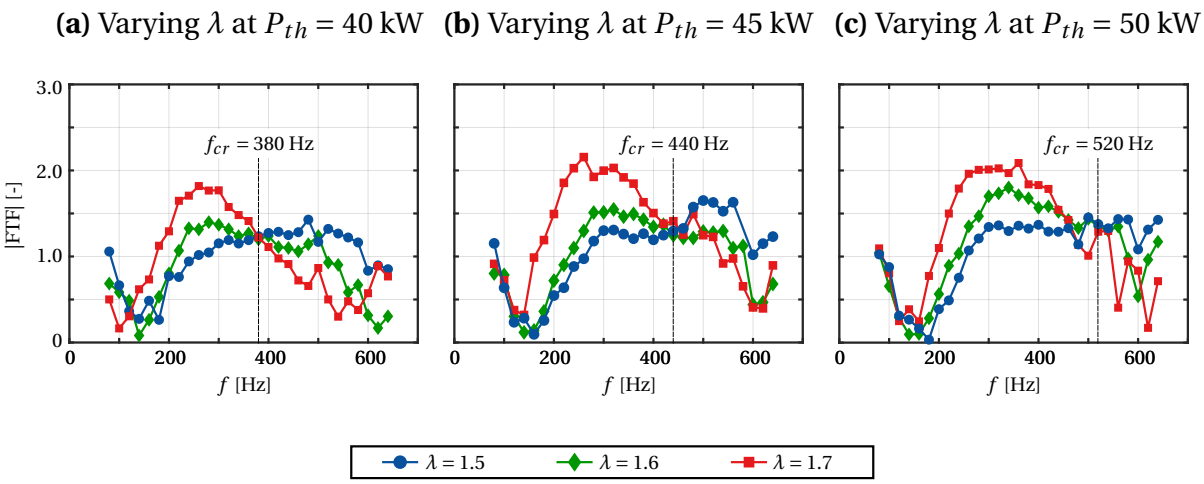

Figure 5.10: *Variation of critical frequency for dispersion with operating conditions*

5.4 Stationary Flame Shapes

Images of stationary flames without acoustic excitation were evaluated following the methodology described in Section 4.4. Sensitivity of flame shape to the thermal power and air ratio was investigated by evaluating geometric parameters at different operating conditions.

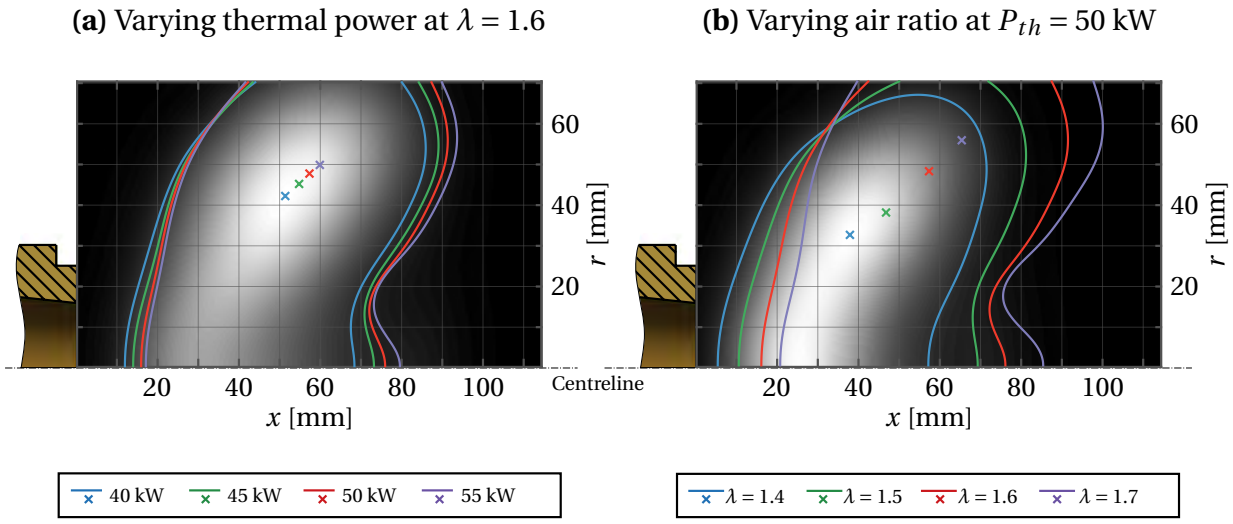

Figure 5.11: *Flame shape contours (lines) and peak OH* intensity (markers) for different operating conditions*

The flame shapes were first compared using boundary contours at normalised intensity level of 0.18 as shown in Figure 5.11. The images show the upper half of the flame with the burner exit on the left. The greyscale image corresponds to the first operating point denoted by blue contour line. Points corresponding to peak image intensity are also marked with a "×". The contours suggest that the flames are principally bowl-shaped with their curvature increasing with thermal power as well as with air ratio. The flame moves towards downstream and

spreads out radially with increase in thermal power and air ratio, the effect of latter is more pronounced than former. The point of peak OH* intensity also shifts axially downwards and radially upwards, more with air ratio than with thermal power.

Three geometric parameters were studied; flame lift-off distance X_F, flame length L_F, and flame diameter d_F (see Figure 4.8). Variation in these parameters with varying thermal power and air ratio is shown in Figure 5.12(a). These parameters are normalised by the burner exit diameter d_b. Data obtained through processing of acquired images is shown with black markers. In order to better visualise the sensitivity of flame geometry, a plane surface was fitted to each parameter. Figure 5.12(b) also show the 2D curves for varying thermal power at $\lambda = 1.6$ and varying air ratio at $P_{th} = 50$ kW. The fitted curves were extracted from the plane surface data. Maximum changes are observed in flame diameter and minimum in flame length. Thus, flame diameter is the most sensitive to the operating conditions.

(a) Flame geometric properties evaluated and fitted surfaces for varying P_{th} and λ

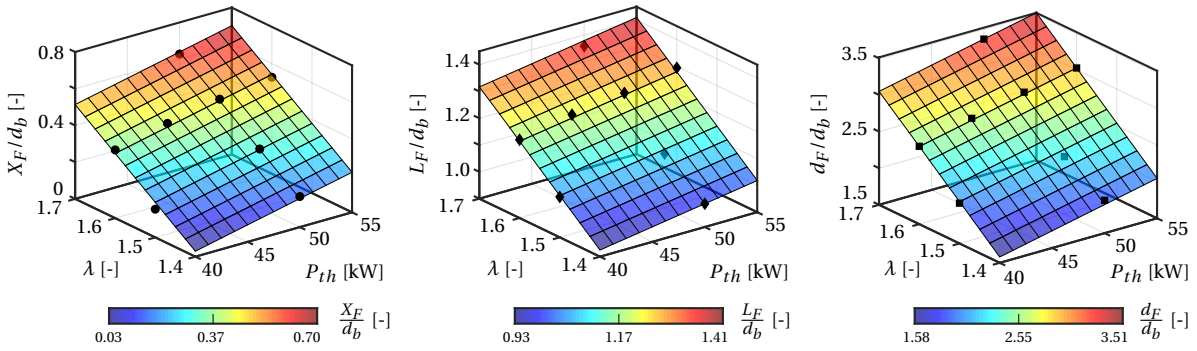

(b) Varying P_{th} at $\lambda = 1.6$ **(c)** Varying λ at $P_{th} = 50$ kW

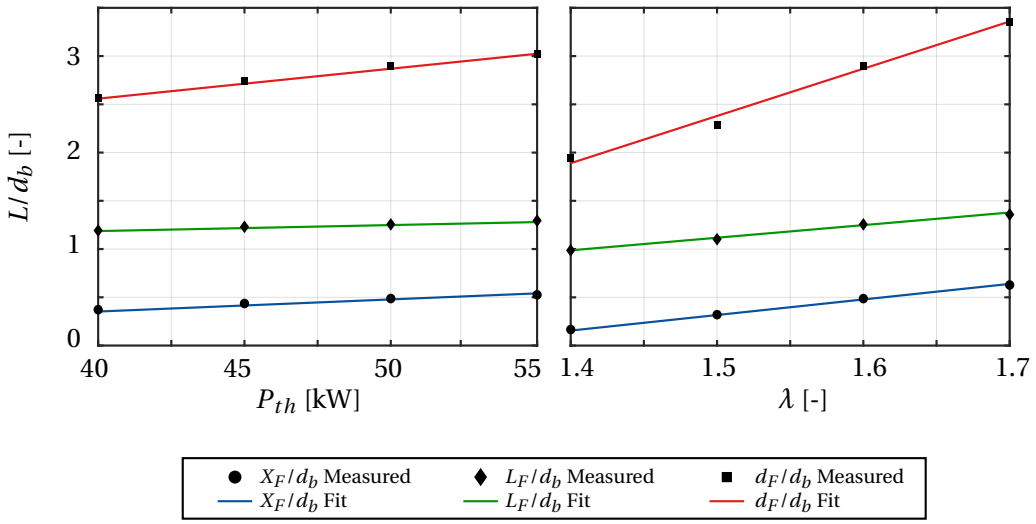

Figure 5.12: *Variation in flame lift-off distance, length, and diameter with operating conditions*

As shown in Figure 2.6(b), the flame lift-off distance X_F is a function of the axial flow velocity and turbulent burning velocity. An increase in thermal power does not significantly influence the burning velocity which is a strong function of combustion chemistry [78]. However, it increases the flow velocity and therefore the lift-off distance slightly increases. Whereas with increase in air ratio, combustion occurs at leaner conditions with significantly reduced burning velocity. Additionally, higher air flow-rate increases the flow velocity. Hence, X_F significantly increases with air ratio [24, 112, 113].

The length of the flame relates to the time required for main combustion reactions to take place. A higher burning rate would result in a shorter flame length. For a simplified analysis, the length can be assumed to be proportional to the square-root of the ratio of mean flow velocity to the mean turbulent burning velocity [22, 86]:

$$L_F \propto \sqrt{\frac{\bar{u}}{s_F}} \tag{5.4}$$

The flow velocity $\bar{u}$ increases with increasing thermal power and the flame length slightly increases. However as the air ratio increases, it significantly reduces the burning velocity s_F while increasing the flow velocity. Therefore, L_F increases profoundly with air ratio [55].

The increase in width or diameter of the flame can be understood from Equation 2.36. Assuming that the burning velocity and reaction enthalpy do not increase with increasing thermal power at constant λ, the effective flame area A_F and hence d_F would increase for a higher heat release. With increasing air ratio at a fixed heat release, the decrease in burning velocity has to be compensated by increase in flame area A_F and therefore d_F significantly increases.

These geometric features help in understanding the variation of FTFs with operating parameters.

5.5 Explanation of FTF Sensitivity to Operating Conditions

The variation of FTFs with thermal power and air ratio can be described through a combination of the following *sensitivity mechanisms* [24, 86]:

1. An increase in thermal power or a decrease in air ratio results in a corresponding increase in the volumetric *power density*. An energetically denser flame is more sensitive to acoustic perturbations and therefore the amplitude of FTF would increase (see description of *lean premixed* combustion on p. 2.)

2. The *swirl perturbations* (see Figure 2.7(a)) resulting in heat release fluctuations have a more pronounced effect for a wider flame. Therefore as the diameter of flame increases, one should expect the amplitude of FTF to increase.

3. With an increase in flame length, the *axial dispersion* of the heat release fluctuations increases (see FTF description on p. 18). Thus, the heat release fluctuation along the length of flame become less coherent at high frequencies resulting in a drop in the FTF amplitude.

4. When the gap between burner exit and flame (lift-off distance) increases, the perturbations associated with convective mechanisms take more time to travel with the mean flow from burner exit to the flame front. Hence, this *convective delay* would increase resulting in steeper phase of FTF (see Equation 5.1).

Thus, the mechanisms in play are a strong function of the flame geometry. In general, these mechanisms are active in parallel and the resulting behaviour is a superposition of the individual responses when in linear domain. The operating conditions can alter one or more of these mechanisms resulting in a certain dynamic response of the flame. A summary of the sensitivity of flame geometry and FTF to operating parameters is furnished in Table 5.1.

Table 5.1: *Variation in flame geometric parameters with operating parameters and FTF sensitivity mechanisms*

Flame Geometry				
Variable	-	Diameter d_F	Length L_F	Lift-off X_F
$P_{th}\uparrow$	-	$\uparrow$	$\sim$	$\uparrow$
$\lambda\uparrow$	-	$\Uparrow$	$\uparrow$	$\Uparrow$
Sensitivity Mechanisms				
No.	1	2	3	4
Variable	Power Density	Swirl Perturbations	Axial Dispersion	Convective Delay
$P_{th}\uparrow$	$\uparrow$	$\uparrow$	$\sim$	$\sim$
$\lambda\uparrow$	$\downarrow$	$\uparrow$	$\uparrow$	$\uparrow$
Effect on |FTF|	$\uparrow$	$\uparrow$	$\downarrow$	$\sim$
Effect on $\angle$FTF	$\sim$	$\sim$	$\sim$	$\uparrow$

Symbols: $\uparrow$ Increase, $\Uparrow$ Large increase, $\downarrow$ Decrease, $\sim$ No change.

The overall increase in amplitude with increasing thermal power (see Figure 5.8) can be attributed to the increase in power density and flame diameter. Since the flame length remains almost unchanged, the axial dispersion does not influence the increase in amplitude at high frequencies. Furthermore, due to a small increase in the flame lift-off distance with thermal power, the slopes of FTF phase curves are approximately the same. This suggests that the convective time delay is a weak function of thermal power.

An increase in air ratio decreases the power density but increases the flame diameter. These counteracting mechanisms show two different trends, as evident above and below f_{cr}. The

increase in radial flame spread dominates the decrease in power density at low frequencies ($< f_{cr}$) and therefore increases FTF amplitude. At higher frequencies, the axial dispersion of heat release fluctuation due to increased flame length overcomes the amplitude increase due to higher flame diameter. Therefore, a net decrease in FTF amplitude is observed above f_{cr}. The increase in this critical frequency with increasing thermal power (see Figure 5.10) suggests that it is a strong function of power density. Although the net result is a superposition of the two effects, the proportional contribution from power density shifts the critical point rightward. Thus, a high density flame can follow faster perturbations than a lower density flame. The flame becomes more compact with increasing thermal power and axial dispersion occurs at higher frequencies. Moreover, since the increase in X_F is significantly higher for increasing air ratio, the convective time delay increases. As a result, the phase curves of FTFs become steeper with increasing air ratio.

The point of first minimum $\mathrm{FTF}_{min,1}$ and maximum FTF_{max} in FTF amplitudes shifts to higher frequencies with increasing thermal power and lower frequencies with increasing air ratio. It indicates that like f_{cr}, $f_{min,1}$ and f_{max} are also a strong function of power density.

6 Results for Empirical Modelling of FTF

In this chapter, results for empirical modelling of FTFs based on Proper Orthogonal Decomposition (POD) are outlined. The POD modes and coefficients allow a better understanding of the sensitivity of FTFs to the operating parameters as interpreted in Section 6.1. Reconstruction of FTF at a non-measured exemplary operating point and its comparison with experimentally determined FTF are given in Section 6.2. Finally, Section 6.3 describes the influence of data selection on POD results. This was assessed by comparing validation errors and mode independence for different data ensembles.

6.1 Interpretation of POD Modes and Coefficients

Using the procedure outlined in Section 4.5, POD was applied to an ensemble of FTFs data with nine OPs for obtaining the POD modes and coefficients. Amplitudes and phases for the chosen FTF data are shown in Figure 6.1.

As also noted in Figures 5.8 and 5.9, the overall amplitude increases with thermal power whereas the amplitude at higher frequencies decreases with increasing air ratio. The overall phase curves shift slightly upward with thermal power while slope remains unchanged. On the other hand, the phase curves shifts significantly downward with air ratio and slope of the curves increases.

From the POD of the data ensemble, the Mode Relevance Indices (MRIs) (see Equation 2.56) corresponding to FTF amplitudes and phases are shown in Figure 6.2. Both, linear and logarithmic scales are used for better visualisation. Since the MRIs become close to zero after the third mode, only first three modes were selected for both amplitude and phase.

The first three modes for FTF amplitude are shown in Figure 6.3(a) with respect to frequency. The corresponding coefficients are shown by meshes in Figure 6.3(b) with respect to the 2D parametric space. The coefficients calculated are denoted by markers. For better visualisation, the meshes are refined by spline interpolation.

The first mode is representative of the mean behaviour of FTF amplitude irrespective of the operating parameter. This is because the first POD mode represents an overall mean trend of the data ensemble [45]. With a change in operating parameter, the coefficient for the first mode changes. Since it is multiplied by the first mode, the overall FTF amplitude is affected.

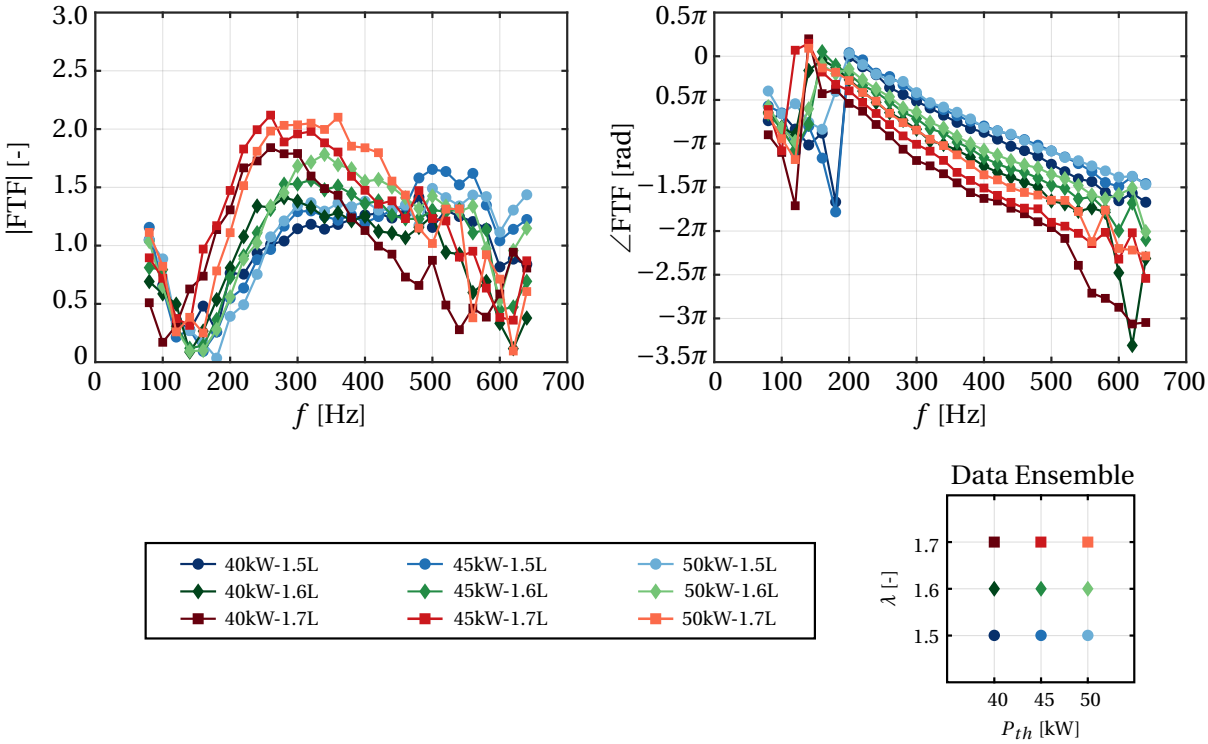

Figure 6.1: *Ensemble of FTF data (amplitudes and phases) selected for performing POD*

(a) FTF Amplitude **(b)** FTF Phase

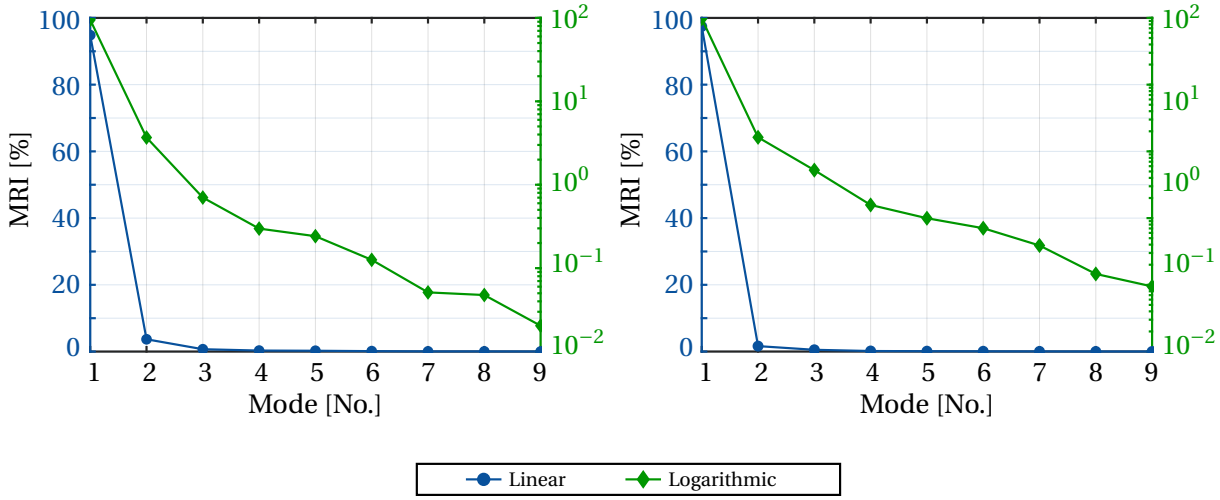

Figure 6.2: *Mode Relevance Indices (MRIs) for FTF amplitude and phase*

For instance, the coefficient a_1 generally increases with both the thermal power and air ratio, thus increasing the overall amplitude proportionally throughout the frequency range[1]. This is

[1]Exceptionally, a_1 shows little change for varying λ at $P_{th} = 40$ kW. This is because the OP 40kW-1.7L has high amplitude at low frequency and very low amplitude at high frequency. The converse is true for 40kW-1.5L as shown in Figure 6.1. Thus, the frequential mean of the two amplitude curves are close to each other even though

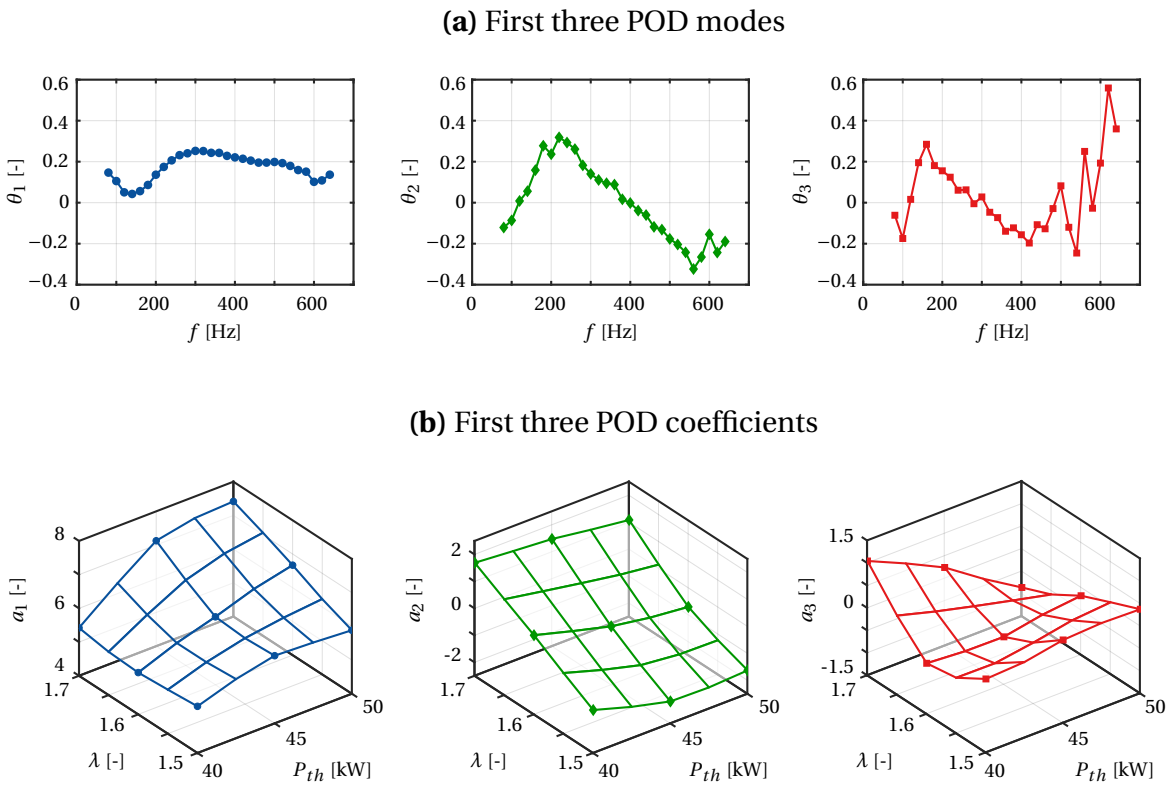

Figure 6.3: *First three POD modes and coefficients for FTF amplitude*

a characteristic of increasing power density and flame diameter (see Section 5.5). Therefore, the first mode can be associated with sensitivity mechanisms 1 and 2 in Table 5.1.

The second mode contributes to the FTF amplitude more at low frequency than at high frequency. Thus, it captures the effect of increasing air ratio since the corresponding coefficient a_2 show slight change with thermal power while it significantly increases with λ. Hence, it can be attributed to mechanism 3 in Table 5.1. In other words, mode 2 represent the FTF trend which is dominated by high axial dispersion.

Finally, the third mode captures the sharp drop in amplitude near 120 Hz and scatter in data at high frequencies. The corresponding coefficients are close to zero except for cases 40kW-1.7L and 50kW-1.7L for which high scatter can be seen in Figure 6.1.

Similarly, the first three modes and coefficients for FTF phase are shown in Figure 6.4.

The first mode shows a generic behaviour of the FTF phase common to all operating points. Since the mode has negative values while the coefficient a_1 is positive, an increase in a_1 shifts the curve proportionally downwards. Phase values at high frequency shift more than those at low frequency since the whole curve is multiplied by the same a_1 value. This increases the slope of the curve and therefore a_1 is a stronger function of λ than P_{th}. It is in-line with the significant downward shifting of phase curves and increasing slope with increasing air ratio.

the distributions are significantly different.

(a) First three POD modes

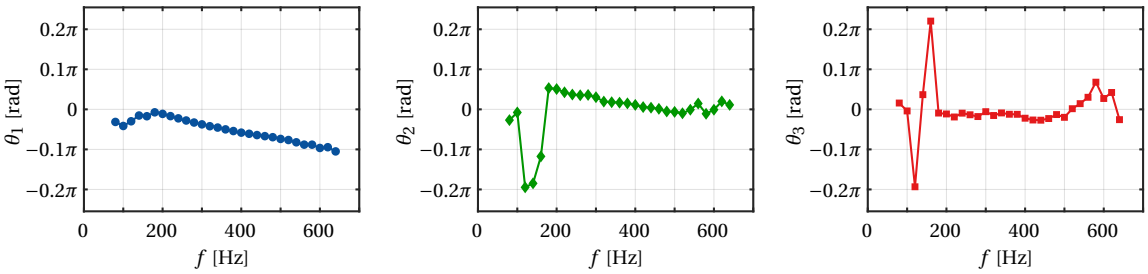

(b) First three POD coefficients

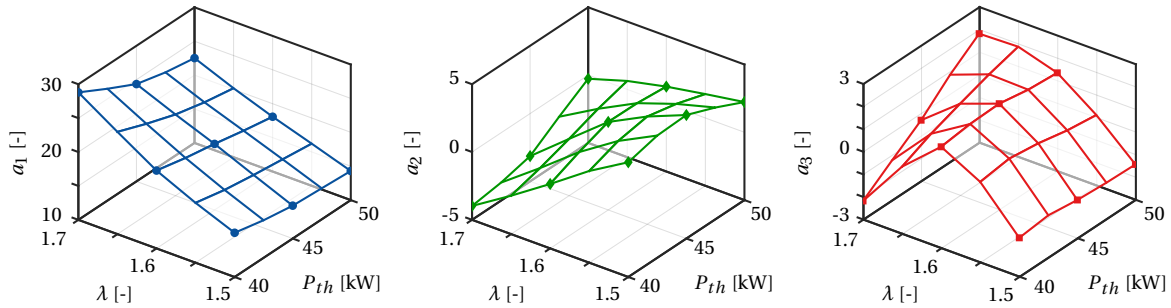

Figure 6.4: *First three POD modes and coefficients for FTF phase*

The a_1 coefficient shows some decrease with P_{th} which corresponds to slight upward shifting and minute decrease in slope of the phase curves with increasing thermal power.

The second mode has captured the effect of inverted bell shape of the phase curves at around 100-200 Hz. Moreover, it has positive values at mid frequencies and is close to zero at high frequencies. Since a_2 significantly decreases with λ, this contributes in slightly changing the slope of the main phase curve. a_2 shows negligible change with varying P_{th}.

Finally, the third phase mode shows a significant jump at around 120 Hz corresponding to FTF$_{min,1}$ point. Moreover, it has captured the scatter preset at high frequencies as evident for higher coefficient values such as for 40kW-1.7L.

Conclusively, POD mode 1 of FTF amplitude represents generic trends of FTFs. Its coefficient scale with both, thermal power and air ratio. It can be associated to power density and flame diameter based sensitivity mechanisms. The influence of increasing air ratio is captured by mode 2. Coefficients of mode 2 scale well with increasing air ratio but show little dependence on thermal power. Therefore, this mode represents the axial dispersion resulting due to increased flame length. On the other hand, POD mode 1 of FTF phase is responsible for the trends with both varying thermal power and air ratio. It also represents the increase in slope with increasing λ. Mode 2 has little influence on the net curves. Moreover, for both amplitude and phase, mode 3 is responsible for the jump near $f_{min,1}$ = 120 Hz and scatter at high frequencies (>580 Hz).

6.2 Reconstruction and Validation at Desired Operating Point

The POD modes and coefficients were used for estimating FTF at a desired operating point 45kW-1.6L. The same data ensemble shown in Figure 6.1 was used excluding the data for 45kW-1.6L. Resulting POD modes were similar to those shown in Figures 6.3 and 6.4, only first three were considered. Reconstruction at a desired point requires interpolating the first three POD coefficients at 45kW-1.6L as shown in Figure 6.5(a) for FTF amplitude.

(a) Evaluated POD coefficients and fitted surfaces for varying P_{th} and λ

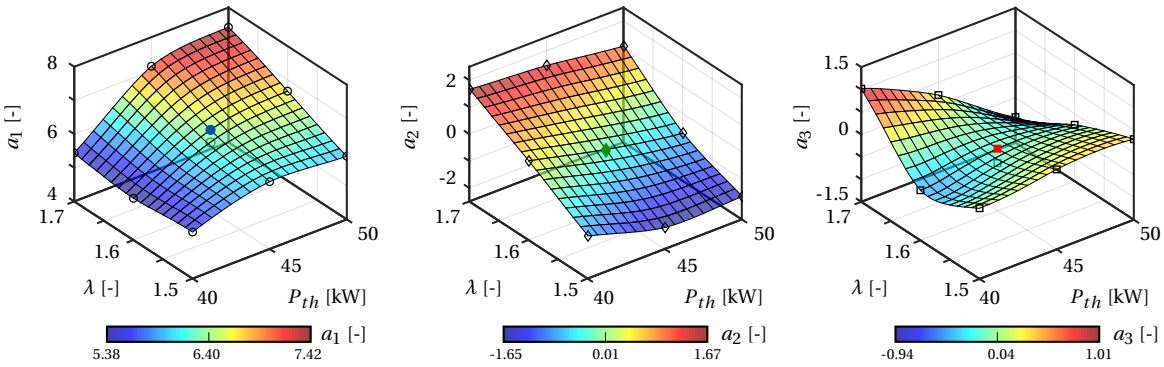

(b) POD coeffcients and fit results for varying P_{th} at $\lambda = 1.6$

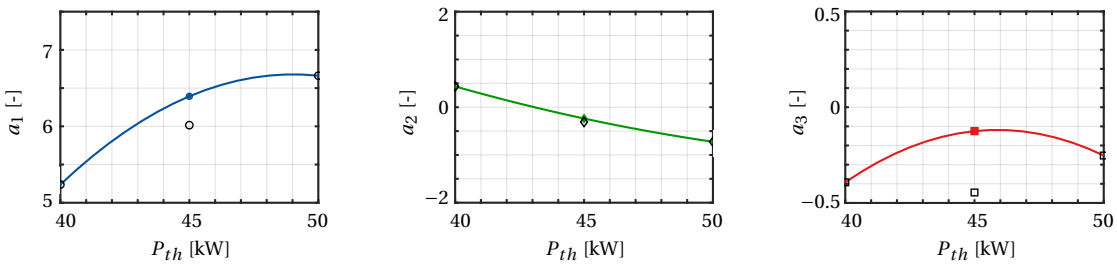

(c) POD coeffcients and fit results for varying λ at $P_{th} = 50$ kW

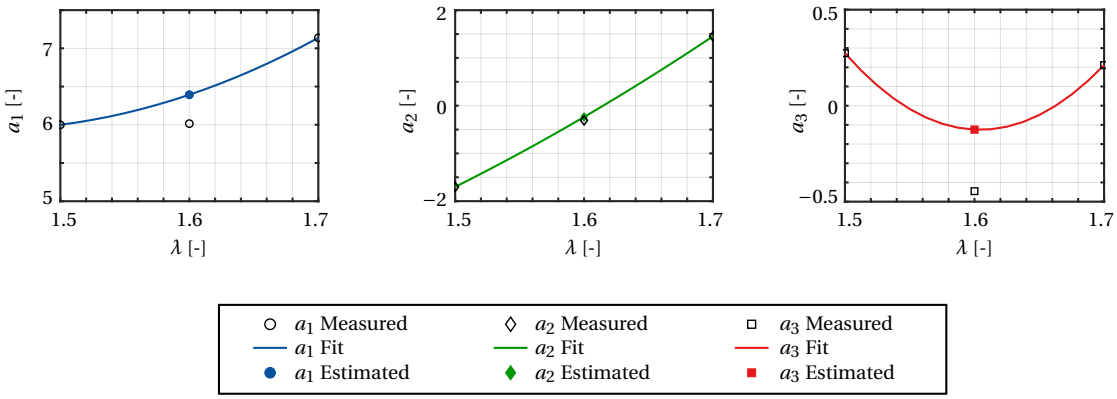

Figure 6.5: *Estimation of POD coefficients for FTF amplitude at 45kW-1.6L*

(a) Evaluated POD coefficients and fitted surfaces for varying P_{th} and λ

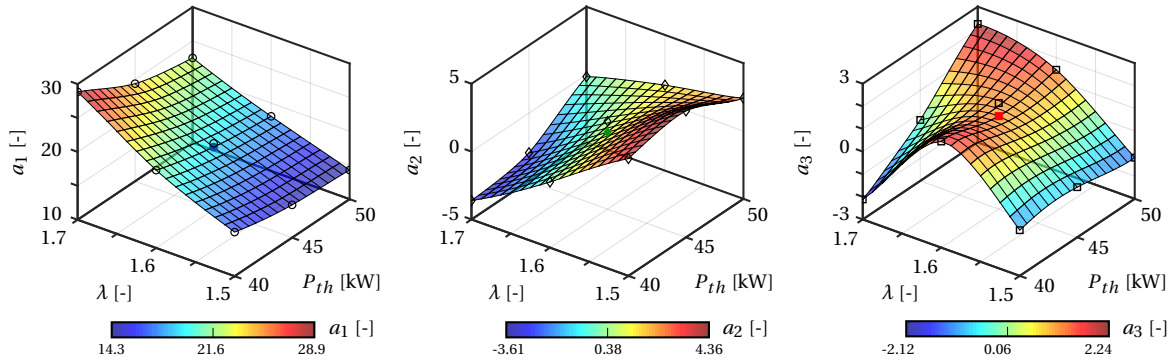

(b) POD coeffcients and fit results for varying P_{th} at $\lambda = 1.6$

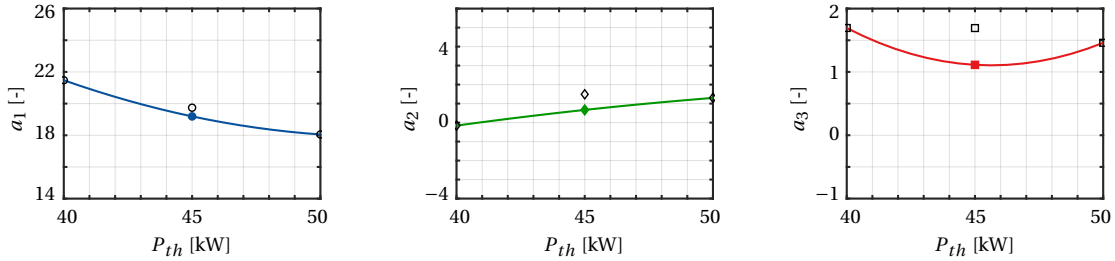

(c) POD coeffcients and fit results for varying λ at $P_{th} = 50$ kW

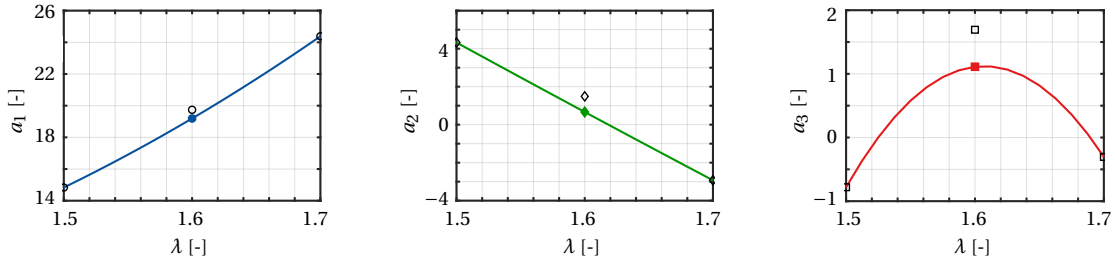

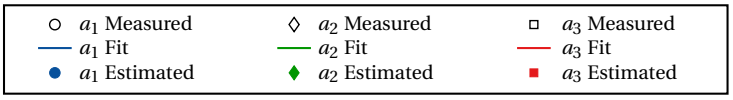

Figure 6.6: *Estimation of POD coefficients for FTF phase at 45kW-1.6L*

The interpolation of POD coefficients was done by fitting a spline surface (MATLAB fit model *thinplateinterp*) to the calculated coefficients and estimating at the desired point as shown by the coloured markers. 2D curves of POD coefficients extracted from surfaces for varying thermal power and air ratio are also shown in Figures 6.5(b) and 6.5(c) respectively. Although not included in the calculation, the coefficient value corresponding to the measured FTF at 45kW-1.6L is also shown for comparison. The estimated coefficients are lower than those corresponding to the measured FTF. A very good match between measured and estimated values is found for a_2. Highest deviation is observed for a_3. This can be explained by random nature

of a_3 since mode 3 represents scatter in FTF. The deviation in a_1 estimate is reflected in the reconstruction result discussed later.

The interpolation of POD coefficient for FTF phase is shown in Figure 6.6. Both, fitted surfaces for varying thermal power and air ratio as well as 2D curves for individually varying thermal power and air ratio are shown.

The coefficients corresponding to the measured FTF at 45kW-1.6L are also shown. Estimated coefficients are generally lower than the measured coefficient values. A good match between the two can be seen for a_1 and a_2. Highest deviation is observed for a_3. Again, it can be attributed to the random nature of this coefficient.

The reconstruction for FTF amplitude and phase at operating point 45kW-1.6L is shown in Figure 6.7.

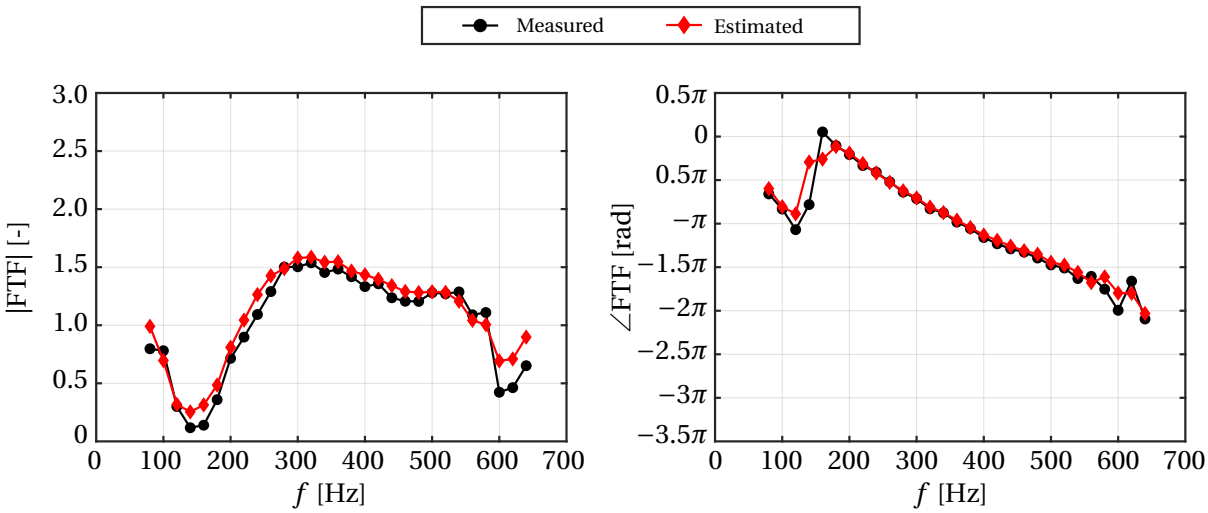

Figure 6.7: *Reconstruction of FTF amplitude and phase at 45kW-1.6L using three POD modes*

Good agreement against experimental results can be seen for both the amplitude and phase with RMSE of 0.1245 and 0.3978 rad respectively. Note that RMSE depends upon the sample values and therefore errors in amplitude cannot be compared with that in phase. The estimated amplitude is slightly higher than the measured one since estimated a_1 values were higher than the corresponding measured values. Results for FTF phase are better than the amplitude since the phases in the considered ensemble are similar and their shape almost remains the same. They show little variation with P_{th} and a regular variation with λ. Therefore, they could be modelled more accurately. Whereas, the amplitude curve not only shifts vertically but also changes its shape significantly with varying operating conditions.

6.3 Influence of Data Ensemble on POD Results

Since POD is solely based on the input data ensemble, it is important to assess how the data selection affect the POD results. To this end, five different data ensembles were considered and POD was applied to FTF amplitude and phase using each of these ensembles. The influence of data ensembles on reconstruction of FTF at the desired operating point is evaluated. Later, POD modes are assessed for their independence from the input data ensemble.

The considered data ensembles are shown in Figure 6.8. Black dots show the arrangement of measurement points used as input data whereas the desired operating point is marked in red diamond on the parametric grid. For all the cases, only first three modes sorted in descending order of relevance index were used. Cases 1, 2, and 3 were used to reconstruct FTF at 45kW-1.6L. Excluding data for 45kW-1.6L, case 1 represents the same data ensemble as used in Section 6.1. Case 2 was chosen to evaluate the influence of number of measurement points. A comparison of case 2 and 3 allowed evaluating the effect of commonality between the measurement and desired OPs. Cases 4 and 5 were used to compare reconstruction at 40kW-1.5L and assess the effect of parametric extrapolation in contrast to interpolation. Case 5 covers the operating range of P_{th} at fixed λ and vice versa. Whereas case 4 includes a variety of combinations of P_{th} and λ with variations in both, roughly circumscribing most of the operating grid.

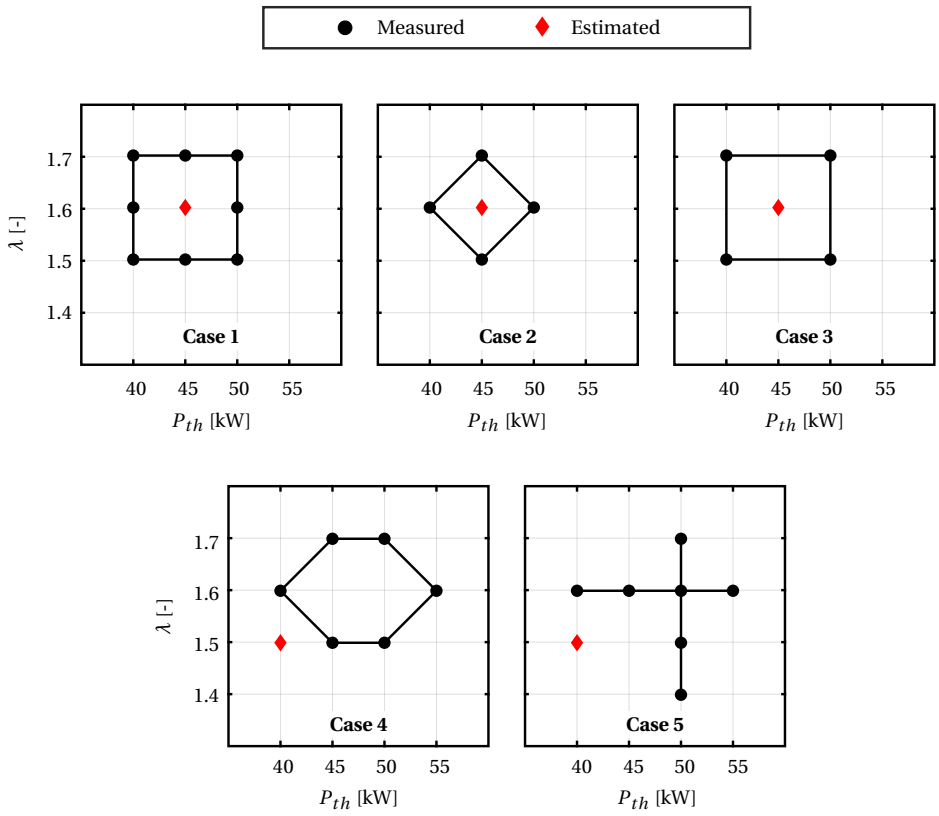

Figure 6.8: *Cases used to study influence of FTF data ensemble on POD results*

The results obtained using different cases are summarised in Table 6.1.

Table 6.1: *Summary of reconstruction results obtained for FTF amplitude and phase using different data ensembles*

Case	No. of Measurements	Reconstruction	Amplitude RMSE	Phase RMSE
1	8	45kW-1.6L	0.1245	0.3978
2	4	45kW-1.6L	0.1248	0.3333
3	4	45kW-1.6L	0.1675	0.5888
4	6	40kW-1.5L	0.1343	0.4546
5	7	40kW-1.5L	0.2174	0.7453

For the operating point 45kW-1.6, the best reconstruction results considering both the amplitude and phase are obtained with case 2. The second best results are obtained using case 1. Note that case 2 has only 4 measurement points but the points have at least one operating parameter in common with the desired OP. Due to the same reason, case 2 produces better results than case 3 even though the two cases have the same number of measurements. Comparing case 1 with case 3, the high number of measurement points improve the reconstruction as expected but the effect is very mild. For the desired operating point 40kW-1.5, case 4 gives much better results than case 5, although both have at least one measurement parameter in common with the desired point.

This suggests that good reconstruction quality can be obtained even with a limited number of measurement and less common OPs. The important aspect is that the ensemble includes data for a variety of combinations of the operating parameters with variation in each of them. It roughly encompasses the desired OP for interpolation and is close to it for extrapolation.

The sensitivity of POD modes to the input data ensemble was assessed using Mode Sensitivty Indices (MSIs) as defined by Equation 4.11. For evaluating this parameter, case 1 was considered as reference and the modes obtained using different ensembles were compared. This was done by calculating MSI for both amplitude and phase of FTF for each data ensemble as shown in Figure 6.9. Note that the number of modes cannot be more than the number of measurement points for a given ensemble. The maximum number of modes for each case are shown.

The quantity MSI between two data ensembles signify the deviation between the POD modes obtained using the two ensembles [47, 98]. For perfectly matching POD modes, MSI = 1 whereas for completely different POD modes, MSI = 0 [111]. For case 1, MSI = 1 since a scalar product of mode with itself is unity. For other cases, the MSI generally decreases with increasing mode number, with some exceptions like case 5. Similar trends of MSI have also been reported by others, though for field variables other than FTF such as flame image intensity [46, 47]. The random character of MSI at higher mode numbers, such as for case 5, is also reported. Recall that for all the cases, only first three modes are of relevance. The MSI for cases 2 and 5 have

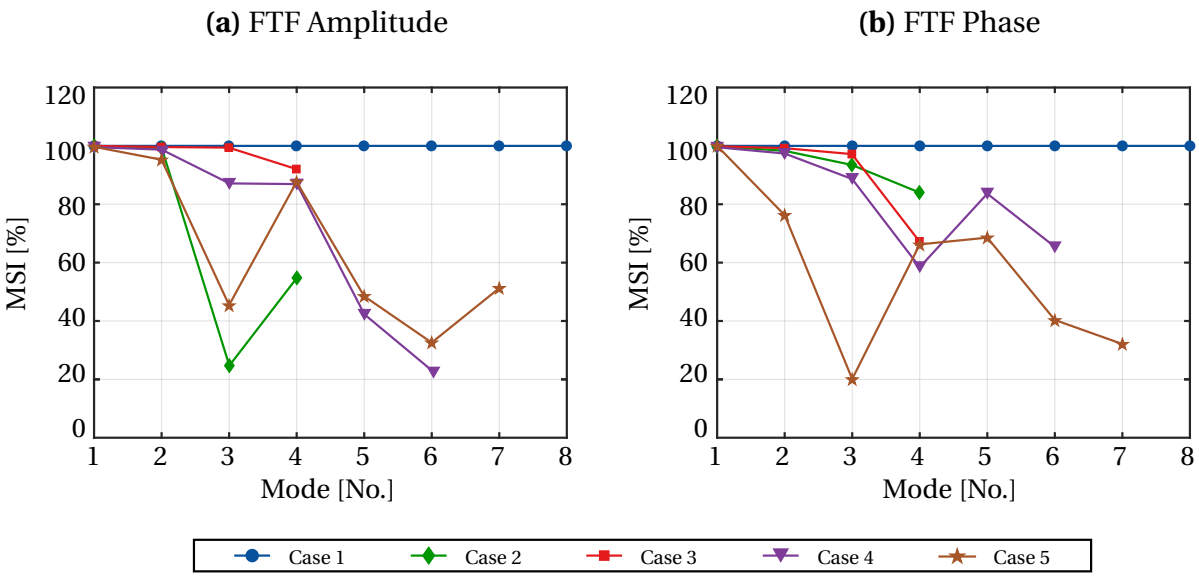

Figure 6.9: *Mode Sensitivity Indices (MSI) for FTF amplitude and phase*

quite lower values compared with others. In other words, their resulting modes are much different from the POD modes obtained using the other three ensembles. Since MSIs for the cases 2 and 5 also differ significantly among themselves, there is a high probability that their respective POD modes are biased to the data ensemble and therefore not reliable. On the other hand, cases 1, 3 and 4 show very similar values up to the third mode which indicates that their respective modes are almost independent of the data used.

Hence, the first three POD modes obtained using cases 1, 3, 4 are not noticeably biased by the data ensembles. Comparing cases 1 and 5 which have almost the same number of data points, MSI results suggest that data points for the ensemble should approximately circumnavigate the major part of the operating domain.

The POD based ROM can also be applied to other thermoacoustic quantities like TMs. An example for FTM is presented in Appendix B.

7 Conclusions and Outlook

This study focused on the experimental determination of the flame response to acoustic perturbations in a gas turbine combustor. The dynamic response of a perfectly premixed natural gas flame was quantified in terms of Flame Transfer Function (FTF) over a frequency range of interest. This function was determined using two methods. The first method was based on acoustic pressure measurement using the Multi-Microphone Method for characterising the behaviour of burner and flame. The second method relied on acoustic and OH* chemiluminescence radiation measurements. A comparison of the two results allowed determination of combustor and flame temperatures. The scope of work included assessing and improving the quality of results.

The following conclusions were drawn for the measurement of FTFs:

1. Transfer functions obtained from the two methods showed similar trends. The two results approximately matched when appropriate combustor and flame temperatures were used in the calculations.
2. The temperatures determined showed similar variation with operating conditions as predicted by an analytical model from a previous work.
3. Results of FTFs demonstrated good reproducibility. Furthermore, acoustical measurement location had negligible impact on the results.
4. FTFs agreed well with the old measurements done by a previous researcher. Both the results showed some scatter at high frequencies.
5. Flame response varies with frequency, which is representative of the constructive and destructive interaction of different driving mechanisms. The frequencies for minimum and maximum response are related to volumetric heat release density.
6. The response is characterised by a constant convective time delay.

The variation in FTFs with operating thermal power and air ratio was evaluated. OH* chemiluminescence images of the flame were used to quantify the variation in flame lift-off distance, length, and diameter. Variations in FTFs were correlated to these parameters. The main findings are:

1. The flame lift-off distance and diameter increases with thermal power and leaner conditions. Flame length is approximately independent of thermal power but increases with flame leanness.

2. The flame becomes more sensitive to perturbations when operated at higher thermal power and under leaner combustion. This is due to an increased heat release density and flame diameter.

3. The effect of leaner combustion is more pronounced than that for higher thermal power.

4. Above a certain frequency, which is a function of heat release density, leaner combustion restricts the flame response. This is due to axial dispersion of the phase of heat release fluctuation which increases with the flame length.

5. The convective time delay between acoustic perturbation and heat release fluctuation increases with air ratio but not with thermal power.

Reduced order modelling of FTF based on Proper Orthogonal Decomposition (POD) was performed. The resulting modes and coefficients were used to estimate FTF at a desired operating point and decompose FTF variation with operating conditions into individual contributions. The crux of the modelling results is given below:

1. POD modes can be associated with specific sensitivity mechanisms describing FTF variations. Mode 1 of FTF gain relates to heat release density and flame radial spread whereas mode 2 corresponds to axial dispersion.

2. The FTF prediction from reduced order model agreed very well with the measurement done for validation.

3. The reconstruction and modal results depend upon the data ensemble used for calculations. To achieve good results, the ensemble should be selected so that it includes data for a variety of combinations of thermal power and air ratio with variation in both.

A possible next step is to quantify the flame dynamics for partially premixed natural gas flame. This would allow incorporation of air perturbation λ' in the data processing routines further to the velocity perturbation u' upstream of the flame. For this purpose, a similar burner with a secondary fuel injector could be installed. Since the FTF would depend upon both λ' and u', it could not be directly determined using optical measurements and pure acoustic method would be required. For a given operating condition, the temperatures determined for perfectly premixed case can then be used for the partially premixed cases.

The test setup should then be extended to Kerosene flames. A similar swirl burner equipped with an air-blast fuel injector can be used. Further to degree of premixing, thermoacoustic characterisation would entail droplet dynamics since acoustics interact and affect the droplet size, distribution, and trajectories. This would significantly alter the flame response. Therefore, the characterisation of spray-only response to acoustics might be needed such as without

flame. Moreover, the optical method could not be directly used for quantifying the heat release and hence determining the FTF. Therefore, pure acoustical method would be needed and temperatures would be necessary for calculations. Previously developed analytical temperature model for the test rig based on energy balance can be explored for extension to the case of Kerosene.

Instead of using the Proper Orthogonal Decomposition (POD) for parametric study of FTFs, it can also be applied to high speed flame images for decomposition of spatial intensity distributions in temporal domain. This would allow directly analysing dynamics of the flame and may result in a meaningful decomposition of the flame response into individual driving mechanisms. Moreover, phase averaging of flame images using POD can be tested to eliminate the need of cumbersome synchronisation between acoustic and optical signals required for phase-resolved measurements.

References

[1] M. A. Gonzalez-Salazar, T. Kirsten and L. Prchlik, "Review of the operational flexibility and emissions of gas- and coal-fired power plants in a future with growing renewables", *Renewable and Sustainable Energy Reviews*, vol. 82, pp. 1497–1513, Feb. 2018, ISSN: 13640321. DOI: 10.1016/j.rser.2017.05.278.

[2] IEA. (9th Jan. 2020). World Energy Outlook 2019 – Analysis, International Energy Agency, [Online]. Available: https://www.iea.org/reports/world-energy-outlook-2019 (visited on 25/01/2020).

[3] PEI. (4th Oct. 2019). The role of the gas turbine in the energy transition, Power Engineering International, [Online]. Available: https://www.powerengineeringint.com/2019/04/10/the-role-of-the-gas-turbine-in-the-energy-transition/ (visited on 25/01/2020).

[4] A. H. Lefebvre, "The role of fuel preparation in low-emission combustion", *Journal of Engineering for Gas Turbines and Power*, vol. 117, no. 4, pp. 617–654, 1st Oct. 1995, ISSN: 0742-4795, 1528-8919. DOI: 10.1115/1.2815449.

[5] N. Cumpsty, D. Mavris and M. Kirby, "Aviation and the environment: Outlook", in *ICAO Environmental Report 2019*, 2019, p. 15.

[6] M. P. Boyce, *Gas Turbine Engineering Handbook*, 2nd ed. Boston, MA: Gulf Professional Pub, 2002, ISBN: 978-0-88415-732-8.

[7] H. I. H. Saravanamuttoo, G. F. C. Rogers and H. Cohen, *Gas Turbine Theory*, 7th ed. Harlow, England ; New York: Pearson, 2017, ISBN: 978-1-292-09309-3.

[8] S. M. Correa, "A review of NOx formation under gas-turbine combustion conditions", *Combustion Science and Technology*, vol. 87, no. 1-6, pp. 329–362, Jan. 1993, ISSN: 0010-2202, 1563-521X. DOI: 10.1080/00102209208947221.

[9] J. J. Keller, "Thermoacoustic oscillations in combustion chambers of gas turbines", *AIAA Journal*, vol. 33, no. 12, pp. 2280–2287, Dec. 1995, ISSN: 0001-1452, 1533-385X. DOI: 10.2514/3.12980.

[10] T. Scarinci and J. L. Halpin, "Industrial trent combustor: Combustion noise characteristics", *Journal of Engineering for Gas Turbines and Power*, vol. 122, no. 2, pp. 280–286, 1st Apr. 2000, ISSN: 0742-4795, 1528-8919. DOI: 10.1115/1.483207.

[11] W. Krebs, P. Flohr, B. Prade and S. Hoffmann, "Thermoacoustic stability chart for high-intensity gas turbine combustion systems", *Combustion Science and Technology*, pp. 99–128, 2002. DOI: 10.1080/00102200208984089.

[12] T. C. Lieuwen and V. Yang, Eds., *Combustion Instabilities in Gas Turbine Engines: Operational Experience, Fundamental Mechanisms and Modeling*, Progress in Astronautics and Aeronautics v. 210, Reston, VA: American Institute of Aeronautics and Astronautics, 2005, ISBN: 978-1-56347-669-3.

[13] Y. Huang and V. Yang, "Dynamics and stability of lean-premixed swirl-stabilized combustion", *Progress in Energy and Combustion Science*, vol. 35, no. 4, pp. 293–364, Aug. 2009, ISSN: 03601285. DOI: 10.1016/j.pecs.2009.01.002.

[14] S. Candel, "Combustion dynamics and control: Progress and challenges", *Proceedings of the Combustion Institute*, vol. 29, no. 1, pp. 1–28, Jan. 2002, ISSN: 15407489. DOI: 10.1016/s1540-7489(02)80007-4.

[15] J. M. Apeloig, F.-X. d'Herbigny, F. Simon, P. Gajan, M. Orain and S. Roux, "Liquid-fuel behavior in an aeronautical injector submitted to thermoacoustic instabilities", *Journal of Propulsion and Power*, vol. 31, no. 1, pp. 309–319, Jan. 2015, ISSN: 0748-4658, 1533-3876. DOI: 10.2514/1.b35290.

[16] T. Poinsot and D. Veynante, *Theoretical and Numerical Combustion*, 2nd ed. Philadelphia: Edwards, 2005, ISBN: 978-1-930217-10-2.

[17] T. Komarek and W. Polifke, "Impact of swirl fluctuations on the flame response of a perfectly premixed swirl burner", *Journal of Engineering for Gas Turbines and Power*, vol. 132, no. 6, p. 061 503, 1st Jun. 2010, ISSN: 0742-4795, 1528-8919. DOI: 10.1115/1.4000127.

[18] E. Freitag, "On the measurement and modelling of flame transfer functions at elevated pressure", PhD thesis, Technischen Universität München, Munich, Germany, 2009.

[19] J. A. Ranalli, C. R. Martin, P. R. Black, U. Vandsburger and R. West, "Measurement of flame transfer functions in swirl-stabilized, lean-premixed combustion", *Journal of Propulsion and Power*, vol. 25, no. 6, pp. 1350–1354, Nov. 2009, ISSN: 0748-4658, 1533-3876. DOI: 10.2514/1.44187.

[20] B. Schuermans, V. Bellucci, F. Guethe, F. Meili, P. Flohr and C. O. Paschereit, "A detailed analysis of thermoacoustic interaction mechanisms in a turbulent premixed flame", in *Volume 1: Turbo Expo 2004*, Vienna, Austria: ASMEDC, 1st Jan. 2004, pp. 539–551, ISBN: 978-0-7918-4166-2. DOI: 10.1115/gt2004-53831.

[21] N. Stadlmair and T. Sattelmayer, "Measurement and analysis of flame transfer functions in a lean-premixed, swirl-stabilized combustor with water injection", in *54th AIAA Aerospace Sciences Meeting*, San Diego, California, USA: American Institute of Aeronautics and Astronautics, 4th Jan. 2016, ISBN: 978-1-62410-393-3. DOI: 10.2514/6.2016-1157.

[22] P. R. Alemela, D. Fanaca, C. Hirsch, T. Sattelmayer and B. Schuermans, "Determination and scaling of thermo acoustic characteristics of premixed flames", *International Journal of Spray and Combustion Dynamics*, vol. 2, no. 2, pp. 169–198, Jun. 2010, ISSN: 1756-8277, 1756-8285. DOI: 10.1260/1756-8277.2.2.169.

[23] B. Schuermans, "Modeling and control of thermoacoustic instabilities", PhD thesis, École Polytechnique Fédérale de Lausanne (EPFL), Lausanne, Netherlands, 2003.

[24] S. Bade, M. Wagner, C. Hirsch, T. Sattelmayer and B. Schuermans, "Influence of fuel-air mixing on flame dynamics of premixed swirl burners", presented at the ASME Turbo Expo 2014: Turbine Technical Conference and Exposition, American Society of Mechanical Engineers Digital Collection, 18th Sep. 2014. DOI: 10.1115/GT2014-25381.

[25] S. Bade, M. Wagner, C. Hirsch, T. Sattelmayer and B. Schuermans, "Design for thermoacoustic stability: Procedure and database", *Journal of Engineering for Gas Turbines and Power*, vol. 135, no. 12, p. 121 507, 1st Dec. 2013, ISSN: 0742-4795, 1528-8919. DOI: 10.1115/1.4025131.

[26] S. Bade, M. Wagner, C. Hirsch, T. Sattelmayer and B. Schuermans, "Design for thermoacoustic stability: Modeling of burner and flame dynamics", *Proceedings of ASME Turbo Expo 2013*, p. 10, 2013. DOI: 10.1115/GT2013-95058.

[27] J. Eckstein, E. Freitag, C. Hirsch and T. Sattelmayer, "Experimental study on the role of entropy waves in low-frequency oscillations in a RQL combustor", *Journal of Engineering for Gas Turbines and Power*, vol. 128, no. 2, pp. 264–270, 1st Apr. 2006, ISSN: 0742-4795, 1528-8919. DOI: 10.1115/1.2132379.

[28] W. A. Chishty, "Effects of thermoacoustic oscillations on spray combustion dynamics with implications for lean direct injection systems", PhD thesis, Virginia Polytechnic Institute and State University, USA, 2005.

[29] R. I. Sujith, "An experimental investigation of interaction of sprays with acoustic fields", *Experiments in Fluids*, vol. 38, no. 5, pp. 576–587, May 2005, ISSN: 0723-4864, 1432-1114. DOI: 10.1007/s00348-004-0912-1.

[30] P. Gajan, F. Simon, M. Orain and V. Bodoc, "Investigation and modeling of combustion instabilities in aero engines", *Journal Aerospace Lab (ONERA)*, no. 11, p. 17, 2016. DOI: 10.12762/2016.AL11-09.

[31] P. R. Alemela, "Measurement and scaling of acoustic transfer matrices of premixed swirl flames", PhD thesis, Technischen Universität München, Munich, Germany, 2009.

[32] M. Lohrmann and H. Büchner, "Scaling of stability limits in lean-premixed gas turbine combustors", in *Volume 1: Turbo Expo 2004*, Vienna, Austria: ASMEDC, 1st Jan. 2004, pp. 453–463, ISBN: 978-0-7918-4166-2. DOI: 10.1115/GT2004-53710.

[33] P. Christ and T. Sattelmayer, "Reduced order modelling of flow and mixing in an automobile HVAC system using proper orthogonal decomposition", *Applied Thermal Engineering*, vol. 133, pp. 211–223, Mar. 2018, ISSN: 13594311. DOI: 10.1016/j.applthermaleng.2018.01.023.

[34] Y. Wang, B. Yu, Z. Cao, W. Zou and G. Yu, "A comparative study of POD interpolation and POD projection methods for fast and accurate prediction of heat transfer problems", *International Journal of Heat and Mass Transfer*, vol. 55, no. 17-18, pp. 4827–4836, Aug. 2012, ISSN: 00179310. DOI: 10.1016/j.ijheatmasstransfer.2012.04.053.

[35] X. Du, H. Hu, Y. Shen, L. Yang and Y. Yang, "Reduced order analysis of flow and heat transfer for air-cooled condenser of power generating unit", *Applied Thermal Engineering*, vol. 51, no. 1-2, pp. 383–392, Mar. 2013, ISSN: 13594311. DOI: 10.1016/j.applthermaleng.2012.09.029.

[36] R. A. Białecki, A. J. Kassab and Z. Ostrowski, "Application of the proper orthogonal decomposition in steady state inverse problems", in *Inverse Problems in Engineering Mechanics IV*, Elsevier, 2003, pp. 3–12, ISBN: 978-0-08-044268-6. DOI: 10.1016/B978-008044268-6/50005-3.

[37] T. Bui-Thanh, M. Damodaran and K. Willcox, "Proper orthogonal decomposition extensions for parametric applications in compressible aerodynamics", in *21st AIAA Applied Aerodynamics Conference*, Orlando, Florida: American Institute of Aeronautics and Astronautics, 23rd Jun. 2003, ISBN: 978-1-62410-092-5. DOI: 10.2514/6.2003-4213.

[38] B. Malouin, J.-Y. Trépanier and M. Gariépy, "Interpolation of transonic flows using a proper orthogonal decomposition method", *International Journal of Aerospace Engineering*, vol. 2013, pp. 1–11, 2013, ISSN: 1687-5966, 1687-5974. DOI: 10.1155/2013/928904.

[39] M. Taeibi-Rahni, F. Sabetghadam and M. K. Moayyedi, "Low-dimensional proper orthogonal decomposition modeling as a fast approach of aerodynamic data estimation", *Journal of Aerospace Engineering*, vol. 23, no. 1, pp. 44–54, Jan. 2010, ISSN: 0893-1321, 1943-5525. DOI: 10.1061/(ASCE)0893-1321(2010)23:1(44).

[40] P. Druault, P. Guibert and F. Alizon, "Use of proper orthogonal decomposition for time interpolation from PIV data: Application to the cycle-to-cycle variation analysis of in-cylinder engine flows", *Experiments in Fluids*, vol. 39, no. 6, pp. 1009–1023, Dec. 2005, ISSN: 0723-4864, 1432-1114. DOI: 10.1007/s00348-005-0035-3.

[41] H. Gunes, S. Sirisup and G. E. Karniadakis, "Gappy data: To Krig or not to Krig?", *Journal of Computational Physics*, vol. 212, no. 1, pp. 358–382, Feb. 2006, ISSN: 00219991. DOI: 10.1016/j.jcp.2005.06.023.

[42] H. Gunes and U. Rist, "Spatial resolution enhancement/smoothing of stereo–particle-image-velocimetry data using proper-orthogonal-decomposition–based and Kriging interpolation methods", *Physics of Fluids*, vol. 19, no. 6, p. 064 101, Jun. 2007, ISSN: 1070-6631, 1089-7666. DOI: 10.1063/1.2740710.

[43] N. E. Murray and L. S. Ukeiley, "An application of Gappy POD: For subsonic cavity flow PIV data", *Experiments in Fluids*, vol. 42, no. 1, pp. 79–91, 7th Dec. 2006, ISSN: 0723-4864, 1432-1114. DOI: 10.1007/s00348-006-0221-y.

[44] J. Weiss, "A tutorial on the proper orthogonal decomposition", in *AIAA Aviation 2019 Forum*, Dallas, Texas: American Institute of Aeronautics and Astronautics, 17th Jun. 2019, ISBN: 978-1-62410-589-0. DOI: 10.2514/6.2019-3333.

[45] H. Chen, D. L. Reuss, D. L. Hung and V. Sick, "A practical guide for using proper orthogonal decomposition in engine research", *International Journal of Engine Research*, vol. 14, no. 4, pp. 307–319, Aug. 2013, ISSN: 1468-0874, 2041-3149. DOI: 10.1177/1468087412455748.

[46] S. Gadiraju, S. Park, D. Gomez-Ramirez, S. V. Ekkad, K. T. Lowe, H.-K. Moon, Y. Kim and R. Srinivasan, "Application of proper orthogonal decomposition to high speed imaging for the study of combustion oscillations", in *Volume 4B: Combustion, Fuels and Emissions*, Charlotte, North Carolina, USA: American Society of Mechanical Engineers, 26th Jun. 2017, V04BT04A031, ISBN: 978-0-7918-5085-5. DOI: 10.1115/GT2017-64602.

[47] P. Iudiciani, C. Duwig, S. Hosseini, R. Szasz, L. Fuchs, E. Gutmark, A. Lantz, R. Collin and M. Aldén, "Proper orthogonal decomposition for experimental investigation of swirling flame instabilities", in *48th AIAA Aerospace Sciences Meeting Including the New Horizons Forum and Aerospace Exposition*, Orlando, Florida: American Institute of Aeronautics and Astronautics, 4th Jan. 2010, ISBN: 978-1-60086-959-4. DOI: 10.2514/6.2010-584.

[48] K. Bizon, G. Continillo, S. S. Merola and B. M. Vaglieco, "POD analysis of flame dynamics from optical imaging of an IC Engine", in *21st International Colloquium on the Dynamics of Explosions and Reactive Systems*, Poitiers, France: ICDERS, 2007, p. 4.

[49] M. G. Zahn, "Vorhersage und optimierung des thermoakustischen stabilitätsverhaltens von ringbrennkammern unter einsatz passiver dämpfer", PhD thesis, Technische Universität München, Munich, Germany, 2018.

[50] A. D. Pierce, *Acoustics: An Introduction to Its Physical Principles and Applications*, 3rd ed. USA: Springer International Publishing, 2019, ISBN: 978-3-030-11213-4. DOI: 10.1007/978-3-030-11214-1.

[51] P. M. Morse and K. U. Ingard, *Theoretical Acoustics*, ser. International Series in Pure and Applied Physics. New York: McGraw-Hill, 1968, ISBN: 978-0-07-043330-4.

[52] P. Davies, "Practical flow duct acoustics", *Journal of Sound and Vibration*, vol. 124, no. 1, pp. 91–115, Jul. 1988, ISSN: 0022460X. DOI: 10.1016/s0022-460x(88)81407-x.

[53] W. Polifke, B. Verhaar and J. van der Hoek, "Everything you always wanted to know about f and g", *Technical University of Munich*, p. 85, 2009.

[54] S. W. Rienstra and A. Hirschberg, *An Introduction to Acoustics*. Eindhoven University of Technology, 2018.

[55] T. C. Lieuwen, *Unsteady Combustor Physics*. Cambridge: Cambridge University Press, 2012, ISBN: 978-1-139-05996-1. DOI: 10.1017/CBO9781139059961.

[56] J. Matthews and R. L. Walker, *Mathematical Methods of Physics*. N.Y.: Addison-Wesley, 1970, ISBN: 978-0-8053-7002-7.

[57] M. Hall. (1st May 2012). K is for Wavenumber, Agile Scientific, [Online]. Available: https://agilescientific.com/blog/2012/5/1/k-is-for-wavenumber.html (visited on 25/01/2020).

[58] M. Munjal and A. Doige, "Theory of a two source-location method for direct experimental evaluation of the four-pole parameters of an aeroacoustic element", *Journal of Sound and Vibration*, vol. 141, no. 2, pp. 323–333, Sep. 1990, ISSN: 0022460X. DOI: 10.1016/0022-460X(90)90843-O.

[59] M. Åbom, "A note on the experimental determination of acoustical two-port matrices", *Journal of Sound and Vibration*, vol. 155, no. 1, pp. 185–188, May 1992, ISSN: 0022460X. DOI: 10.1016/0022-460X(92)90655-H.

[60] C. O. Paschereit, B. Schuermans, W. Polifke and O. Mattson, "Measurement of transfer matrices and source terms of premixed flames", *Journal of Engineering for Gas Turbines and Power*, vol. 124, no. 2, pp. 239–247, 1st Apr. 2002, ISSN: 0742-4795, 1528-8919. DOI: 10.1115/1.1383255.

[61] A. Fischer, C. Hirsch and T. Sattelmayer, "Comparison of multi-microphone transfer matrix measurements with acoustic network models of swirl burners", *Journal of Sound and Vibration*, vol. 298, no. 1-2, pp. 73–83, Nov. 2006, ISSN: 0022460X. DOI: 10.1016/j.jsv.2006.04.040.

[62] C. L. Lawson and R. J. Hanson, *Solving Least Squares Problems*, ser. Classics in Applied Mathematics 15. Philadelphia: SIAM, 1995, ISBN: 978-0-89871-356-5.

[63] M. Åbom and H. Bodén, "Error analysis of two-microphone measurements in ducts with flow", *The Journal of the Acoustical Society of America*, vol. 83, no. 6, pp. 2429–2438, Jun. 1988, ISSN: 0001-4966. DOI: 10.1121/1.396322.

[64] M. Åbom, "Measurement of the scattering-matrix of acoustical two-ports", *Mechanical Systems and Signal Processing*, vol. 5, no. 2, pp. 89–104, Mar. 1991, ISSN: 08883270. DOI: 10.1016/0888-3270(91)90017-Y.

[65] W. Polifke, "Six lectures on thermoacoustic combustion instability", in *21st CISM IUTAM International Summer School on Measurement, Analysis and Passive Control of Thermoacoustic Oscillations*, Udine, Italy, 2015.

[66] Rayleigh, "The explanation of certain acoustical phenomena", *Nature*, vol. 18, no. 455, pp. 319–321, Jul. 1878, ISSN: 0028-0836, 1476-4687. DOI: 10.1038/018319a0.

[67] I. Chterev, C. W. Foley, D. Foti, S. Kostka, A. W. Caswell, N. Jiang, A. Lynch, D. R. Noble, S. Menon, J. M. Seitzman and T. C. Lieuwen, "Flame and flow topologies in an annular swirling flow", *Combustion Science and Technology*, vol. 186, no. 8, pp. 1041–1074, 3rd Aug. 2014, ISSN: 0010-2202, 1563-521X. DOI: 10.1080/00102202.2014.882916.

[68] J. M. Beér and N. A. Chigier, *Combustion Aerodynamics*, ser. Fuel and Energy Science Series. London: Applied Science Publishers Ltd, 1972, ISBN: 978-0-85334-513-8.

[69] S. Candel, D. Durox, T. Schuller, J.-F. Bourgouin and J. P. Moeck, "Dynamics of swirling flames", *Annual Review of Fluid Mechanics*, vol. 46, no. 1, pp. 147–173, 3rd Jan. 2014, ISSN: 0066-4189, 1545-4479. DOI: 10.1146/annurev-fluid-010313-141300.

[70] S. Burmberger, C. Hirsch and T. Sattelmayer, "Design rules for the velocity field of vortex breakdown swirl burners", in *Volume 1: Combustion and Fuels, Education*, Barcelona, Spain: ASMEDC, 1st Jan. 2006, pp. 413–421, ISBN: 978-0-7918-4236-2. DOI: 10.1115/GT2006-90495.

[71] T. Reichel, "Flashback prevention in lean-premixed hydrogen combustion", PhD thesis, Technischen Universität Berlin, Berlin, Germany, 2017.

[72] D. Darmofal, "The role of vorticity dynamics in vortex breakdown", in *23rd Fluid Dynamics, Plasmadynamics, and Lasers Conference*, Orlando, Florida, USA: American Institute of Aeronautics and Astronautics, 6th Jul. 1993. DOI: 10.2514/6.1993-3036.

[73] C. Hirsch, D. Fanaca, P. Reddy, W. Polifke and T. Sattelmayer, "Influence of the swirler design on the flame transfer function of premixed flames", in *Volume 2: Turbo Expo 2005*, Reno, Nevada, USA: ASMEDC, 1st Jan. 2005, pp. 151–160, ISBN: 978-0-7918-4725-1. DOI: 10.1115/GT2005-68195.

[74] M. Malanoski, M. Aguilar, D.-H. Shin and T. Lieuwen, "Flame leading edge and flow dynamics in a swirling, lifted flame", *Combustion Science and Technology*, vol. 186, no. 12, pp. 1816–1843, 2nd Dec. 2014, ISSN: 0010-2202, 1563-521X. DOI: 10.1080/00102202.2014.923410.

[75] F. Biagioli, "Stabilization mechanism of turbulent premixed flames in strongly swirled flows", *Combustion Theory and Modelling*, vol. 10, no. 3, pp. 389–412, Jun. 2006, ISSN: 1364-7830, 1741-3559. DOI: 10.1080/13647830500448347.

[76] K. Periagaram, "Determination of flame characteristics in a low swirl burner at gas turbine conditions through reaction zone imaging", PhD thesis, Georgia Institute of Technology, USA, 2012.

[77] A. Lipatnikov, *Fundamentals of Premixed Turbulent Combustion*. CRC Press, 24th Oct. 2012, ISBN: 978-0-429-08872-8. DOI: 10.1201/b12973.

[78] A. H. Lefebvre and D. R. Ballal, *Gas Turbine Combustion: Alternative Fuels and Emissions*. Boca Raton, USA: Taylor & Francis, 2010, ISBN: 978-1-4200-8604-1.

[79] I. Chterev, B. Emerson and T. Lieuwen, "Velocity and stretch characteristics at the leading edge of an aerodynamically stabilized flame", *Combustion and Flame*, vol. 193, pp. 92–111, Jul. 2018, ISSN: 00102180. DOI: 10.1016/j.combustflame.2018.02.024.

[80] C. Mayer, J. Sangl, T. Sattelmayer, T. Lachaux and S. Bernero, "Study on the operational window of a swirl stabilized syngas burner under atmospheric and high pressure conditions", *Journal of Engineering for Gas Turbines and Power*, vol. 134, no. 3, p. 031 506, 1st Mar. 2012, ISSN: 0742-4795, 1528-8919. DOI: 10.1115/1.4004255.

[81] H. Merk, "An analysis of unstable combustion of premixed gases", *Symposium (International) on Combustion*, vol. 6, no. 1, pp. 500–512, Jan. 1957, ISSN: 00820784. DOI: 10.1016/s0082-0784(57)80067-8.

[82] S. McAllister, J.-Y. Chen and A. C. Fernandez-Pello, *Fundamentals of Combustion Processes*, ser. Mechanical Engineering Series. New York: Springer, 2011, ISBN: 978-1-4419-7942-1.

[83] D. P. Mishra, *Experimental Combustion: An Introduction*. Hoboken: CRC Press, 2014, ISBN: 978-1-4665-1736-3.

[84] C. Külsheimer and H. Büchner, "Combustion dynamics of turbulent swirling flames", *Combustion and Flame*, vol. 131, no. 1-2, pp. 70–84, Oct. 2002, ISSN: 00102180. DOI: 10.1016/S0010-2180(02)00394-2.

[85] W. Polifke and C. Lawn, "On the low-frequency limit of flame transfer functions", *Combustion and Flame*, vol. 151, no. 3, pp. 437–451, Nov. 2007, ISSN: 00102180. DOI: 10.1016/j.combustflame.2007.07.005.

[86] S. Bade, "Measurement and modeling of the thermoacoustic properties of a modular burner system for premixed swirl flames", PhD thesis, Technischen Universität München, Munich, Germany, 2014.

[87] T. Sattelmayer, "Influence of the combustor aerodynamics on combustion instabilities from equivalence ratio fluctuations", *Journal of Engineering for Gas Turbines and Power*, vol. 125, no. 1, pp. 11–19, 1st Jan. 2003, ISSN: 0742-4795, 1528-8919. DOI: 10.1115/1.1365159.

[88] P. Palies, T. Schuller, D. Durox, L. Y. M. Gicquel and S. Candel, "Acoustically perturbed turbulent premixed swirling flames", *Physics of Fluids*, vol. 23, no. 3, p. 037 101, Mar. 2011, ISSN: 1070-6631, 1089-7666. DOI: 10.1063/1.3553276.

[89] N. V. Stadlmair, "Influence of water injection on the thermoacoustic stability of a lean-premixed combustor", PhD thesis, Technischen Universität München, Munich, Germany, 2017.

[90] B.-T. Chu, "On the generation of pressure waves at a plane flame front", *Symposium (International) on Combustion*, vol. 4, no. 1, pp. 603–612, Jan. 1953, ISSN: 00820784. DOI: 10.1016/S0082-0784(53)80081-0.

[91] W. Polifke, C. O. Paschereit and K. Paschereit, "Constructive and destructive interference of acoustic and entropy waves in a premixed combustor with a choked exit", *The International Journal of Acoustics and Vibration*, vol. 6, no. 3, 2001, ISSN: 24151408. DOI: 10.20855/ijav.2001.6.382.

[92] D. D. Kosambi, "Statistics in function space", *Journal of the Indian Mathematical Society*, vol. 7, pp. 76–88, 1943, ISSN: 0019-5839.

[93] R. Narasimha, "Kosambi and proper orthogonal decomposition", *Resonance*, vol. 16, no. 6, pp. 574–581, Jun. 2011, ISSN: 0971-8044, 0973-712X. DOI: 10.1007/s12045-011-0062-8.

[94] L. Sirovich, "Turbulence and the dynamics of coherent structures. I. Coherent structures", *Quarterly of Applied Mathematics*, vol. 45, no. 3, pp. 561–571, 1st Oct. 1987, ISSN: 0033-569X, 1552-4485. DOI: 10.1090/qam/910462.

[95] A. Chatterjee, "An introduction to the proper orthogonal decomposition", *Current Science*, vol. 78, no. 7, pp. 808–817, 2000.

[96] T. R. Smith, J. Moehlis and P. Holmes, "Low-dimensional modelling of turbulence using the proper orthogonal decomposition: A tutorial", *Nonlinear Dynamics*, vol. 41, no. 1-3, pp. 275–307, Aug. 2005, ISSN: 0924-090X, 1573-269X. DOI: 10.1007/s11071-005-2823-y.

[97] P. LeGresley and J. Alonso, "Airfoil design optimization using reduced order models based on proper orthogonal decomposition", in *Fluids 2000 Conference and Exhibit*, Denver,CO,U.S.A.: American Institute of Aeronautics and Astronautics, 19th Jun. 2000. DOI: 10.2514/6.2000-2545.

[98] C. Duwig and P. Iudiciani, "Extended proper orthogonal decomposition for analysis of unsteady flames", *Flow, Turbulence and Combustion*, vol. 84, no. 1, pp. 25–47, Jan. 2010, ISSN: 1386-6184, 1573-1987. DOI: 10.1007/s10494-009-9210-6.

[99] A. Qamar and S. Sanghi, "Steady supersonic flow-field predictions using proper orthogonal decomposition technique", *Computers & Fluids*, vol. 38, no. 6, pp. 1218–1231, Jun. 2009, ISSN: 00457930. DOI: 10.1016/j.compfluid.2008.11.011.

[100] P. Holmes, J. L. Lumley, G. Berkooz and C. Rowley, *Turbulence, Coherent Structures, Dynamical Systems, and Symmetry*, 2nd ed. Cambridge; New York: Cambridge University Press, 2012, ISBN: 978-0-521-55142-7.

[101] J. Eckstein, "On the mechanisms of combustion driven low-frequency oscillations in aero-engines", PhD thesis, Technischen Universität München, Munich, Germany, 2004.

[102] J. Sangl, C. Mayer and T. Sattelmayer, "Dynamic adaptation of aerodynamic flame stabilization of a premix swirl burner to fuel reactivity using fuel momentum", *Journal of Engineering for Gas Turbines and Power*, vol. 133, no. 7, p. 071 501, 1st Jul. 2011, ISSN: 0742-4795, 1528-8919. DOI: 10.1115/1.4002659.

[103] A. Fischer, "Hybrid thermoacoustic characterisation of swirl burner", PhD thesis, Technischen Universität München, Munich, Germany, 2004.

[104] T.-W. Lee, *Thermal and Flow Measurements*. Boca Raton: CRC Press, 2008, ISBN: 978-0-8493-7970-3.

[105] R. Price, I. Hurle and T. Sugden, "Optical studies of the generation of noise in turbulent flames", *Symposium (International) on Combustion*, vol. 12, no. 1, pp. 1093–1102, Jan. 1969, ISSN: 00820784. DOI: 10.1016/S0082-0784(69)80487-X.

[106] A. Huber and W. Polifke, "Dynamics of practical premixed flames, Part I: Model structure and identification", *International Journal of Spray and Combustion Dynamics*, vol. 1, no. 2, pp. 199–228, Jun. 2009, ISSN: 1756-8277, 1756-8285. DOI: 10.1260/175682709788707431.

[107] M. W. Hauser, "Zum Einfluss transversaler akustischer Anregung auf die Dynamik turbulenter vorgemischter Drallflammen", PhD thesis, Technische Universität München, 2014.

[108] U. Neunert, "Thermoakustische Stabilität einer Reisemobilheizung", PhD thesis, Technische Universität München, Munich, Germany, 2009.

[109] C. Leys, C. Ley, O. Klein, P. Bernard and L. Licata, "Detecting outliers: Do not use standard deviation around the mean, use absolute deviation around the median", *Journal of Experimental Social Psychology*, vol. 49, no. 4, pp. 764–766, Jul. 2013, ISSN: 00221031. DOI: 10.1016/j.jesp.2013.03.013.

[110] G. Pretzier, H. Jäger, T. Neger, H. Philipp and J. Woisetschläger, "Comparison of different methods of abel inversion using computer simulated and experimental side-on data", *Zeitschrift für Naturforschung A*, vol. 47, no. 9, 1st Jan. 1992, ISSN: 1865-7109, 0932-0784. DOI: 10.1515/zna-1992-0906.

[111] L. Perret, J. Delville, R. Manceau and J.-P. Bonnet, "Turbulent inflow conditions for large-eddy simulation based on low-order empirical model", *Physics of Fluids*, vol. 20, no. 7, p. 075 107, Jul. 2008, ISSN: 1070-6631, 1089-7666. DOI: 10.1063/1.2957019.

[112] P. Jourdaine, C. Mirat, J. Caudal and T. Schuller, "Stabilization mechanisms of swirling premixed flames with an axial-plus-tangential swirler", *Journal of Engineering for Gas Turbines and Power*, vol. 140, no. 8, p. 081 502, 1st Aug. 2018, ISSN: 0742-4795, 1528-8919. DOI: 10.1115/1.4038617.

[113] T. G. Reichel, S. Terhaar and O. Paschereit, "Increasing flashback resistance in lean premixed swirl-stabilized hydrogen combustion by axial air injection", *Journal of Engineering for Gas Turbines and Power*, vol. 137, no. 7, p. 071 503, 1st Jul. 2015, ISSN: 0742-4795, 1528-8919. DOI: 10.1115/1.4029119.

Appendices

A Mathematical Description of POD Modes and Coefficients

This appendix elaborates the mathematical meaning of the POD modes and coefficients. In Section 4.5, the data matrix **V** was constructed so as to obtain modes in frequency space and coefficients in parametric space. For a better visualisation of raw data and its relation with POD modes and coefficients, transpose of the matrix **V** was considered (see Equation 2.51). Thus, each row of the data matrix contains FTF for all the operating points at a given frequency. This resulted in parametric POD modes and frequential coefficients.

For a simpler analysis, consider two operating points namely; 45kW-1.6L and 50kW-1.6L representing an increase in thermal power. FTF for one operating point (OP_2) is plotted against the FTF for the reference operating point (OP_1) as shown with blue colour in Figure A.1. The coordinate axes correspond to the operating parameters while each data point correspond to a specific frequency, increasing from the darkest to the brightest blue marker.

The data can be considered to be represented by the major and minor axes of a hypothetical ellipse enclosing the data points. For phase plots in Figure A.1(b), data points corresponding to phase jump are excluded since the phase for one operating point becomes positive while the other remains negative. The major axis represents a correlation between FTFs for the two operating points. This means that higher values for OP_2 correspond to higher values for OP_1. The minor axis represents anti-correlation, that is higher values for OP_2 correspond to lower values for OP_1. For this 2D problem, the parametric POD mode 1 can be thought as a unit vector representing the direction of the major axis. Similarly, mode 2 represents the direction of the minor axis[1]. These directions are orthogonal, hence the modes are independent from one another. Moreover, the modes are optimal in that mode 1 represents the direction of maximum variance in the data (change with frequency.) The original data can be projected along the modes representing a new principal coordinate system. For a given frequency, the coefficients of modes 1 and 2 can be considered as magnitudes of components or projections along the unit vectors. They represent the distances in the directions given by modes. These definitions also apply to a second pair of operating points 45kW-1.6L and 45kW-1.7L, shown in green colour in Figure A.1. These two operating points represent an increase in the air ratio. For both amplitude (Figure A.1(a)) and phase (Figure A.1(b)), the direction of correlation (mode 1) is steeper for increasing air ratio than for increasing thermal power. It means that

[1] J. Weiss, "A tutorial on the proper orthogonal decomposition", in *AIAA Aviation 2019 Forum*, Dallas, Texas: American Institute of Aeronautics and Astronautics, 17th Jun. 2019, ISBN: 978-1-62410-589-0. DOI: 10.2514/6.2019-3333. [Online]. Available: https://arc.aiaa.org/doi/10.2514/6.2019-3333 (visited on 06/01/2020).

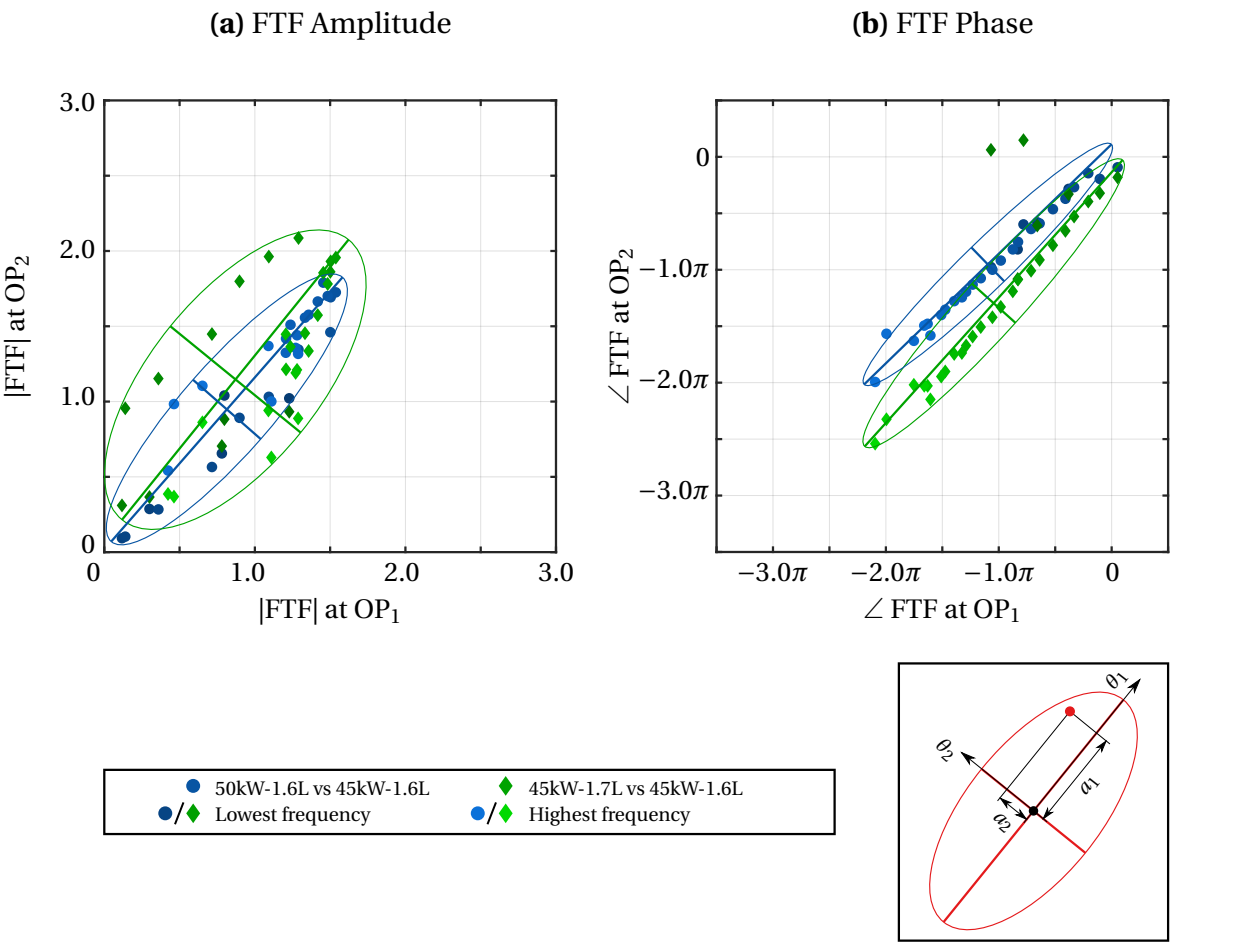

Figure A.1: *Scatter plots of FTF amplitude and phase between two operating points*

an increase in air ratio by 0.1 changes the FTF more than a 10 kW increase in thermal power. Moreover, the contribution from mode 2 is higher for increasing air ratio than for increasing thermal power. Although the slope of mode 1 for the two pairs of operating points is different, it can be approximated as an angle of 45°.

Thus, the two elements of mode 1 are the same representing a correlation in the data. Similarly, the two elements of mode 2 are opposite in sign representing an anti-correlation.

A similar analysis is possible for data matrix $\mathbf{V}$ with axes corresponding to frequential modes and data points corresponding to OPs. However, it would result in only $m << n$ points in the scatter plot making it difficult for visualising the elliptic behaviour. Therefore, $\mathbf{V}^T$ matrix was used for this analysis.

The above analysis can be extended from 2D to n-D with n POD modes. Hence, POD modes signify the directions of correlation in the FTF data ensemble whereas POD coefficients correspond to the data projection along those directions.

B Empirical Modelling of FTM

This appendix describes the extension of POD as used for FTF in Chapter 6 for developing Reduced Order Model (ROM) of FTMs. The general features of FTM and its variation with operating conditions is first explained. Evaluation of POD modes, coefficients, and estimation of the coefficients for desired OP 45kW-1.6L are subsequently explained. Finally, reconstruction at the desired OP and validation are outlined.

B.1 General Trend and Variation with Operating Parameters

A specimen of FTMs obtained in the current study for three different Operating Points (OPs) representing varying P_{th} and λ is shown in Figure B.1. The figure shows amplitudes and phases for the four elements of FTM.

The element $\mathbf{FTM_{11}}$ relating acoustic pressures across the flame has a phase of zero and a fairly constant amplitude. Both the quantities show little change with P_{th} and λ. $\mathbf{FTM_{12}}$ has generally a very low amplitude except for frequencies above 400 Hz. At low frequencies, it increases with P_{th} as well as λ. Whereas, at high frequencies it shows some decrease with both the parameters. The phase of $\mathbf{FTM_{12}}$ generally decreases with frequency and show a jump corresponding to minimum $|\mathbf{FTM_{12}}|$. This minimum shifts rightward with P_{th} and leftward with increasing λ. For element $\mathbf{FTM_{21}}$, the amplitude is close to zero whereas its phase decreases with increasing frequency. Its amplitude and phase show little change with P_{th} but both decreases with increasing λ, particularly at high frequency. Finally, the element $\mathbf{FTM_{22}}$ shows the highest amplitude among all elements. Its phase almost linearly decreases with increasing frequency which is characteristic of a convective time delay. Thus, this element representing the relationship of velocity perturbation at the flame downstream to that at upstream is the most significant in describing the flame dynamics[1]. Its amplitude increases with P_{th} throughout the frequency spectrum where as it increases at low and decreases at high frequency with λ. Moreover, its phase slightly shifts upwards with P_{th} whereas it becomes steeper and shifts significantly downwards with increasing λ.

[1] U. Neunert, "Thermoakustische Stabilität einer Reisemobilheizung", PhD thesis, Technische Universität München, Munich, Germany, 2009.

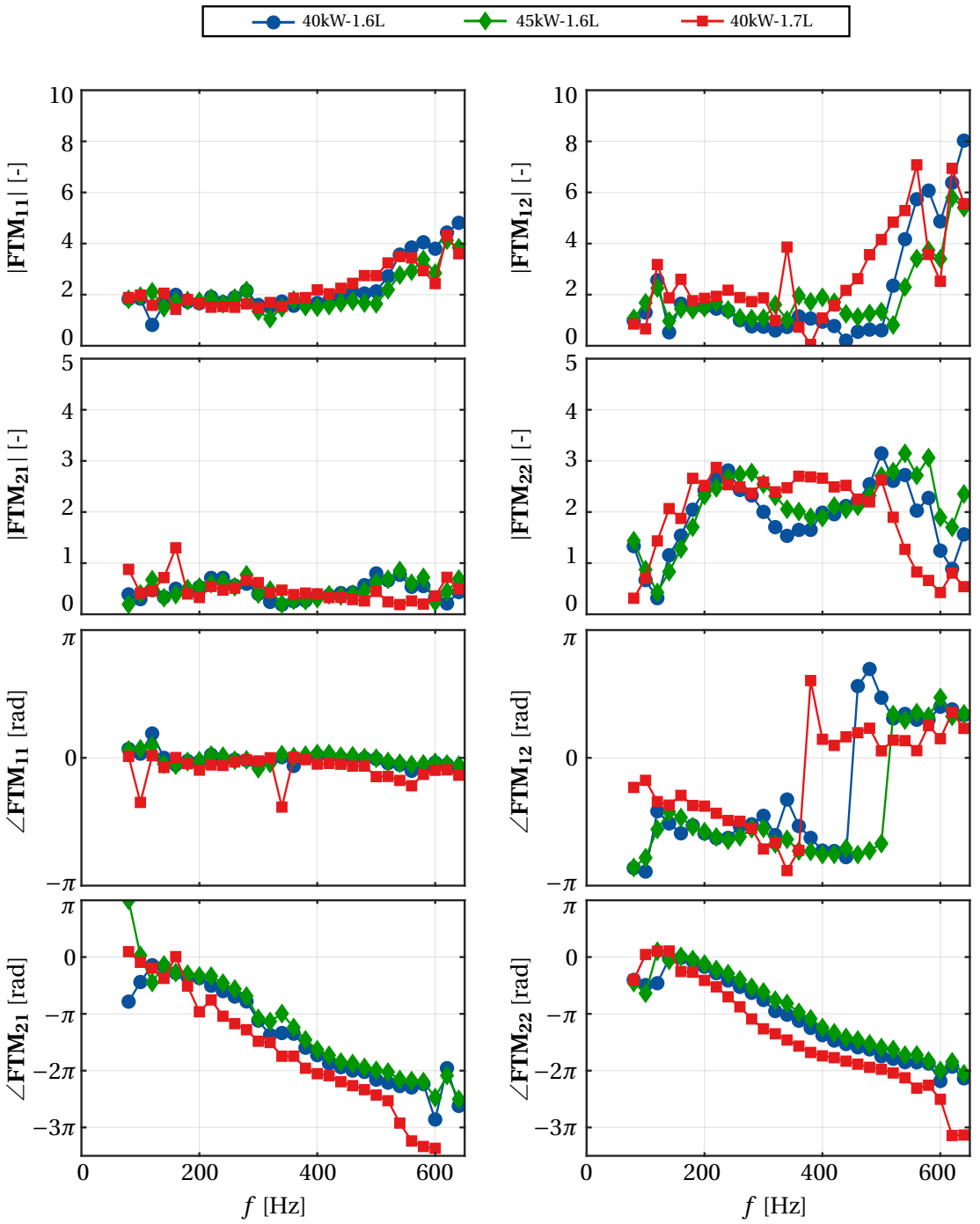

Figure B.1: *Flame Transfer Matrices for varying thermal power and air ratio*

B.2 POD Modes and Coefficients

Since FTM consist of eight different quantities, that is four amplitudes and four phases, the POD was applied to each of these quantities separately for reconstruction of the complete

FTM at a desired OP. Note that the phases were unwrapped with respect to 2π before performing the POD. The data ensemble used for performing POD consisted of eight OPs and the reconstruction was done at 45kW-1.6L. As an example, the intermediate results for $\mathbf{FTM_{22}}$ will be presented followed by the final reconstruction of the complete FTM.

Amplitude and phase data ensemble for $\mathbf{FTM_{22}}$ is shown in Figure B.2 including the data for validation at 45kW-1.6L. The curves in this plot show similar variation with P_{th} and λ as observed in Figure B.1.

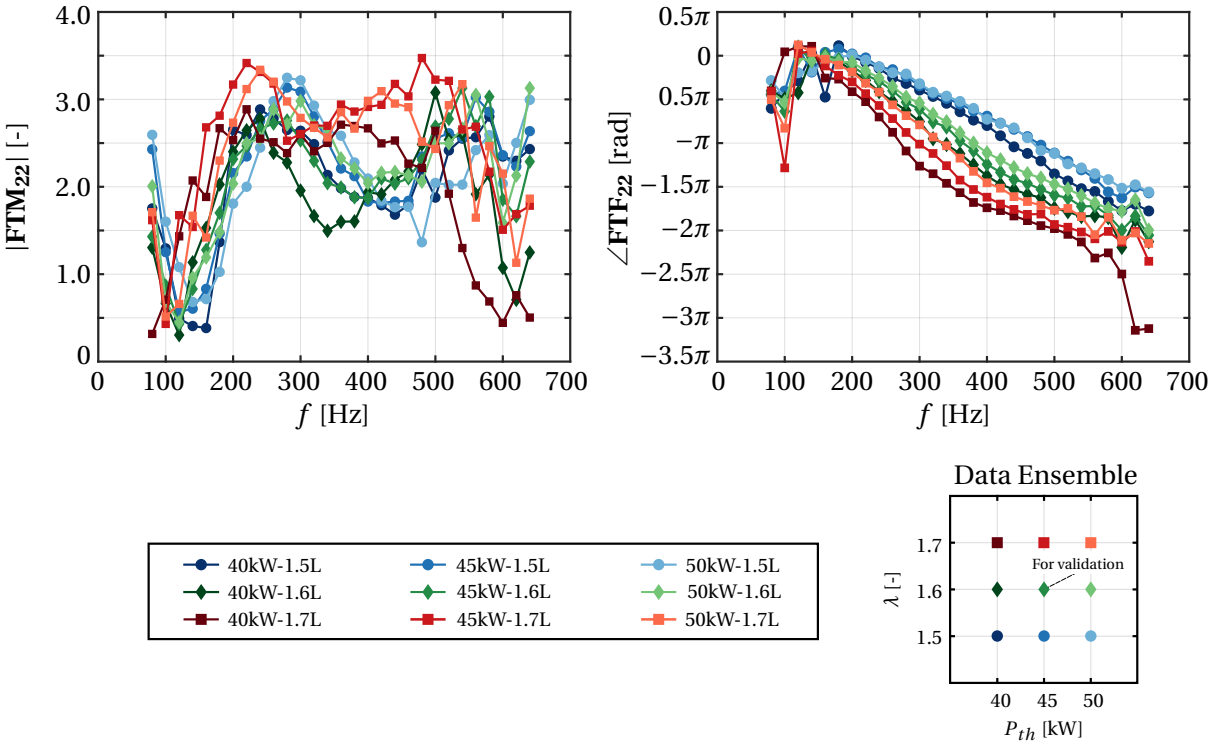

Figure B.2: *Ensemble of* $\mathbf{FTM_{22}}$ *data (amplitudes and phases) used for performing POD and validation data at 45kW-1.6L*

The MRIs obtained for the amplitude and phase of $\mathbf{FTM_{22}}$ are depicted in Figure B.3. They are very similar to the MRIs obtained for FTFs in Figure 6.2. Since they become close to zero for mode 3 and above, first three POD modes were selected for further processing.

Figure B.4 outlines the first three POD modes and coefficients obtained for the amplitude of $\mathbf{FTM_{22}}$.

The first mode captures the sharp drop in amplitude at around 100 Hz and remain constant afterwards. It signifies the mean of all the amplitude curves in Figure B.2. Its corresponding coefficient a_1 is a strong function of thermal power and has little dependence upon λ. Thus, mode 1 contributes to the overall increase in $|\mathbf{FTM_{22}}|$ with thermal power and little change with air ratio.

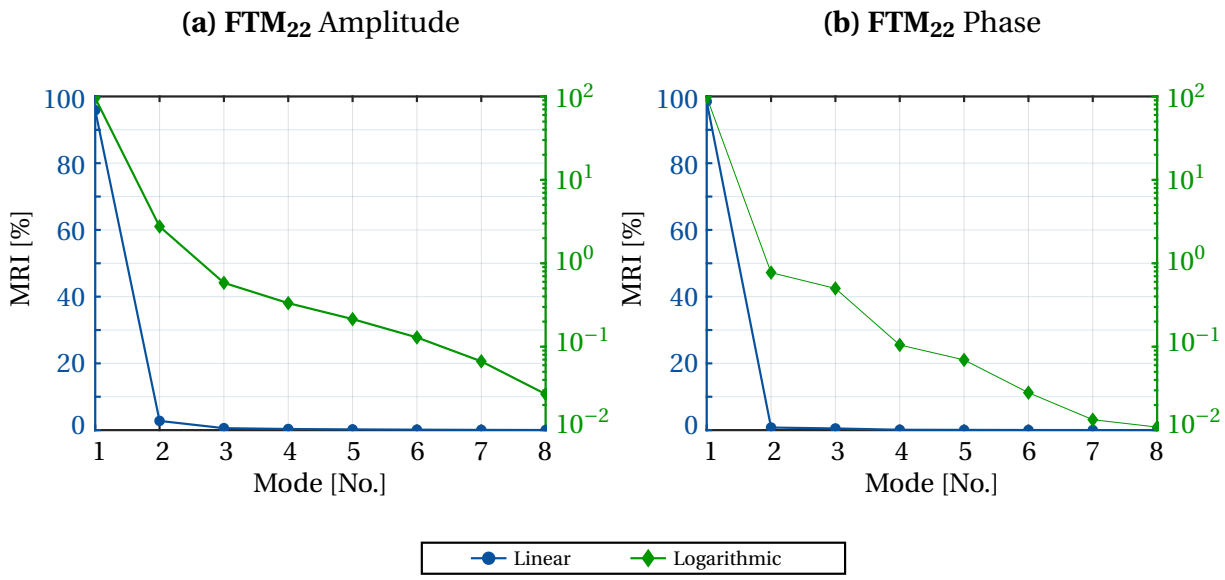

Figure B.3: *Mode Relevance Indices (MRIs) for* **FTM$_{22}$** *amplitude and phase*

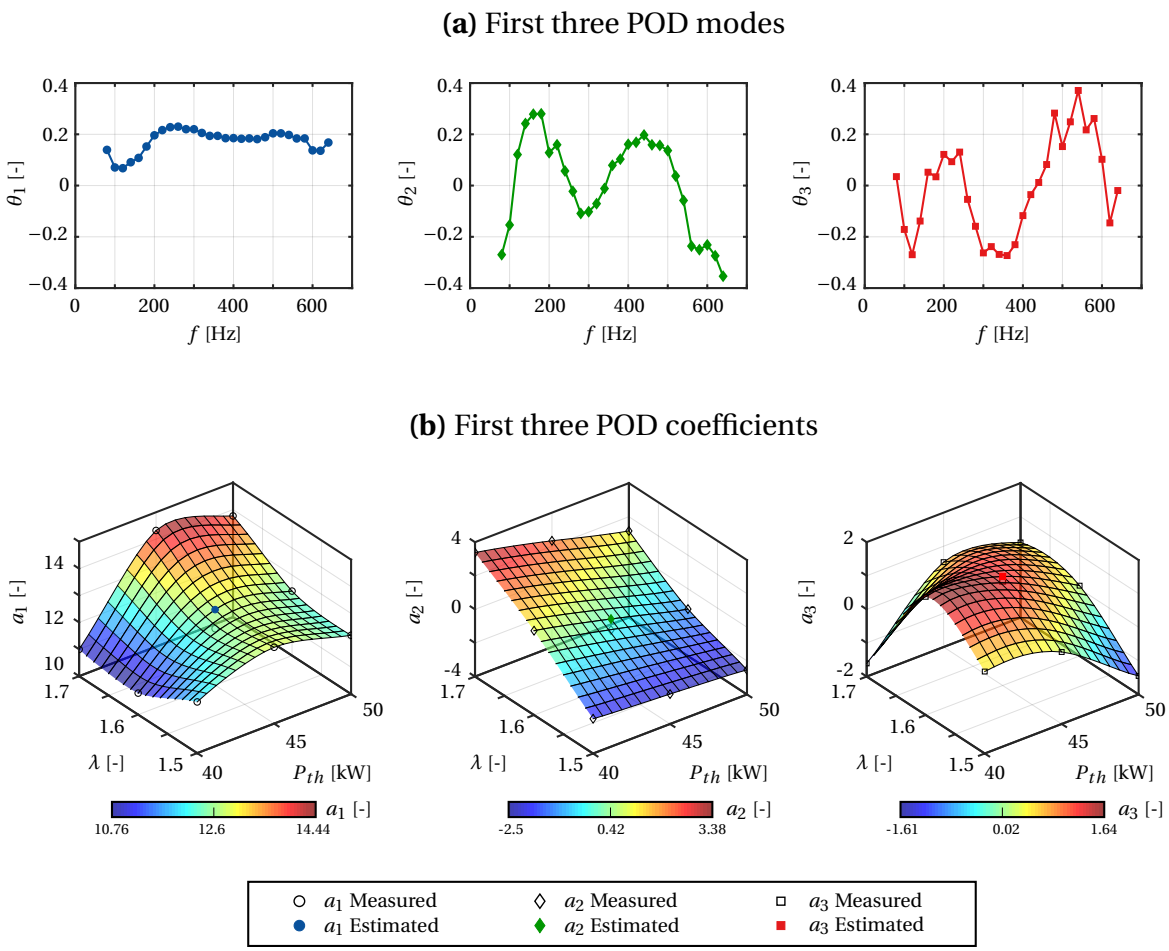

Figure B.4: *First three POD modes and coefficients for* **FTM$_{22}$** *amplitude*

The mode 2 show high amplitude at low frequencies and low amplitudes at high frequencies. Hence, it tends to change the shape of the amplitude curve. Its coefficient a_2 significantly increase with λ and show little change with P_{th}. Therefore, mode 2 captures the effect of increasing air ratio.

Mode 3 contributes to the drop in amplitude near 100 Hz and in producing scatter in the curve. It has high values at different OPs including the desired 45kW-1.6L.

For each modal coefficient, a spline surface (MATLAB fit model *thinplateinterp*) was fitted to the measured coefficient values and the value at 45kW-1.6L was interpolated. Coefficient values corresponding to the validation data at 45kW-1.6L are also shown which are generally close to the estimated values. Maximum deviation is observed for a_1.

Similarly, the POD modes and coefficients for **FTM$_{22}$** phase are shown in Figure B.5.

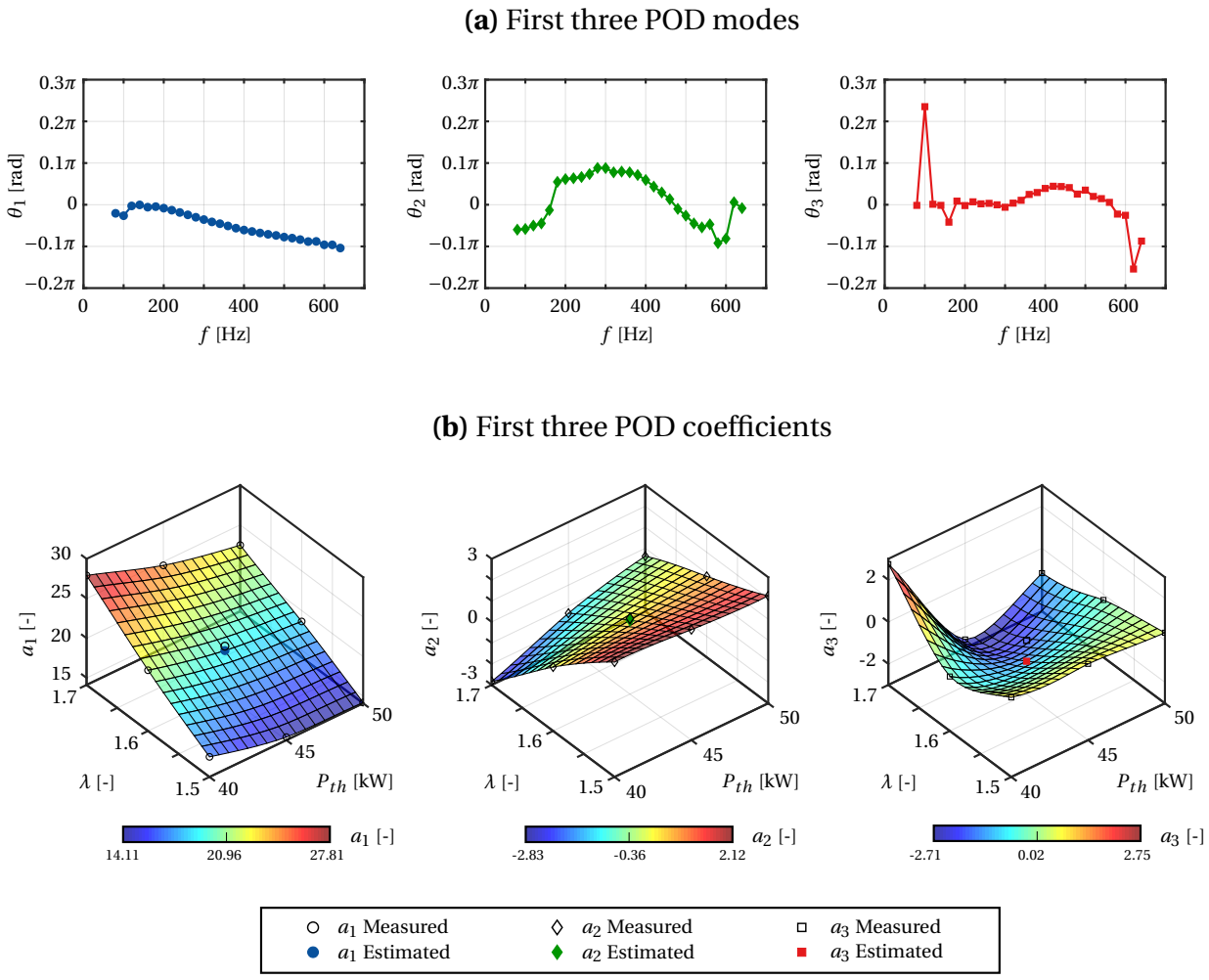

Figure B.5: *First three POD modes and coefficients for* **FTM$_{22}$** *phase*

Mode 1 represents a linear drop in the phase curve which is common to all the curves in Figure B.2. Its coefficient a_1 has positive values which decrease with thermal power shifting

the whole curve slightly upward and minutely decreasing the slope. a_1 significantly increases with air ratio shifting the whole curve downward with significant increase in the slope.

The second mode contributes significantly at mid frequencies as its coefficient a_2 has a strong dependence upon λ than P_{th}. Therefore, it is responsible for the increase in bend in the phase curves that can be observed in Figure B.2 for increasing air ratio.

Finally, mode 3 contributes to the scatter at high frequencies at the phase jump near 100 Hz. The coefficient a_3 do not show a definite trend with operating parameters and is high for some OPs and low for the others.

Again, the coefficients were interpolated at 45kW-1.6L using spline fitted surfaces. For comparison, the coefficient values corresponding to validation data at 45kW-1.6L are also shown. The estimated and experimental coefficient values are similar except for a high deviation for a_3. This is justifiable due to random nature of mode 3 representing the scatter in phase curves.

Similarly, the POD modes and coefficients for the other 6 components of FTM were obtained. The coefficients for amplitudes and phases of all the other elements were estimated using the same procedure.

B.3 Reconstruction and Validation at Desired Operating Point

Reconstruction of each individual component was done separately using Equation 2.57. The reconstruction results for the complete FTM are collectively shown in Figure B.6. For each component, the Root Mean Square Error (RMSE) between the estimated and measured curves calculated using similar formula to Equation 4.10 is also shown.

In general, good reconstruction results are obtained. The best match can be seen for the phase of $\mathbf{FTM_{22}}$. However, the phase of $\mathbf{FTM_{12}}$ show significant deviation, specially at high frequencies. The validation data show a phase jump near 500 Hz whereas the estimate curve increases gradually without any jump. Moreover, the phase values deviate significantly at low frequencies.

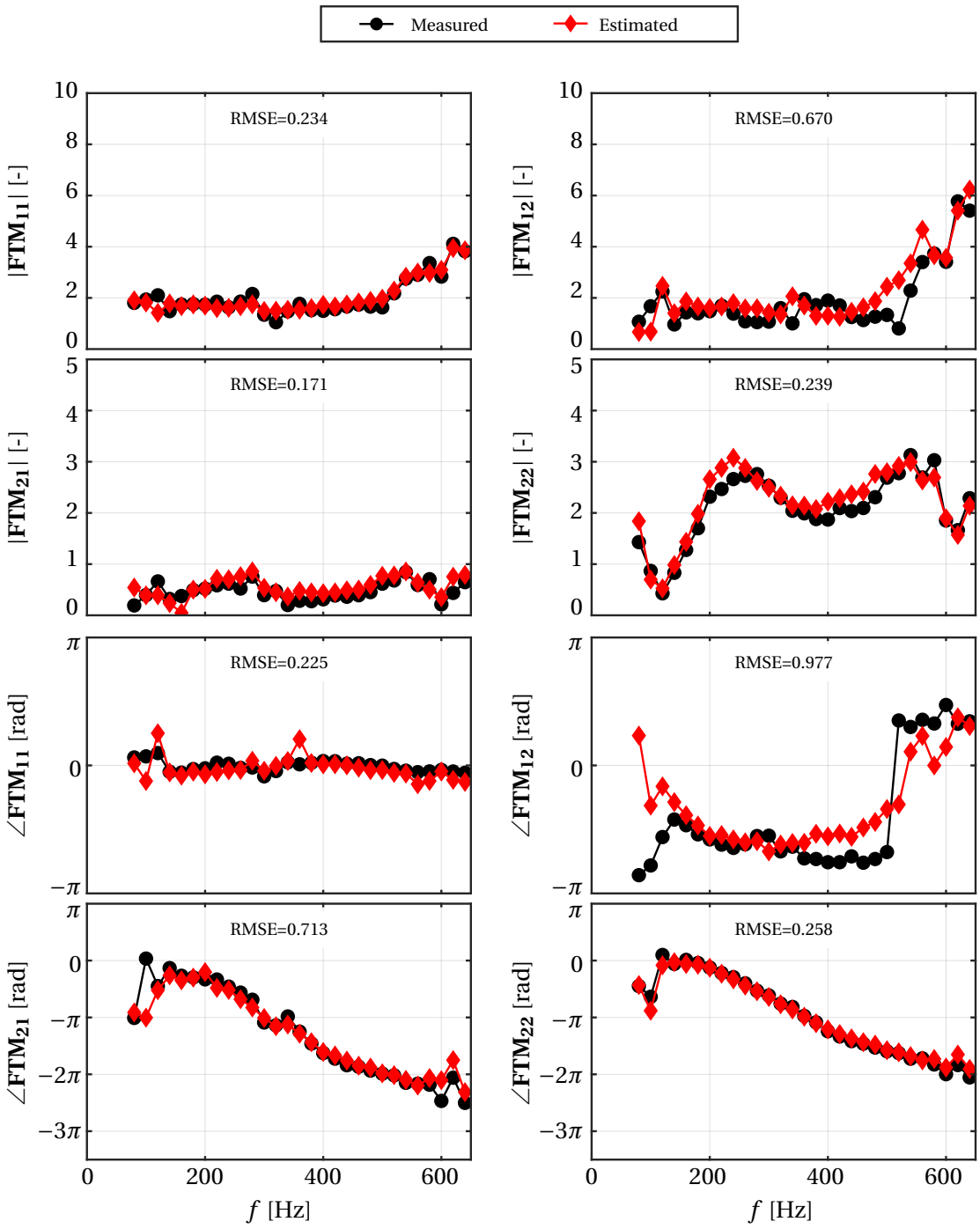

Figure B.6: *Reconstruction of FTM amplitude and phase at 45kW-1.6L using three POD modes*

The reason for deviation in $\angle\mathbf{FTM_{12}}$ can be explained by probing into the data used for POD as shown in Figure B.7. The validation data for 45kW-1.6L is also shown. As can be seen from this data set, high scatter exist at low frequencies near 100 Hz. This explains the deviation between reconstructed and measured curves at low frequency. Furthermore, the phase jump

is not a characteristic of all the phase curves. For instance, 50kW-1.6L show a gradual increase in the high frequency range while other OPs show a sharp jump. Since the estimated phase curve depends upon all the phase data present in the ensemble, it did not capture the sharp phase jump.

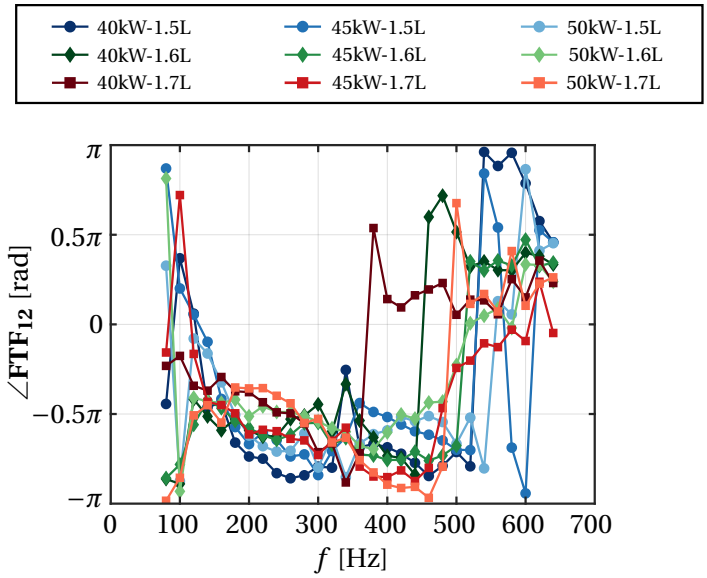

Figure B.7: *Ensemble of* $\mathbf{FTM_{12}}$ *phase data used for performing POD and validation data at 45kW-1.6L*